

2014-01-01

# Frequency Selective Surfaces For Extreme Applications

Jay Houston Barton

*University of Texas at El Paso*, jbar2600@gmail.com

Follow this and additional works at: [https://digitalcommons.utep.edu/open\\_etd](https://digitalcommons.utep.edu/open_etd)



Part of the [Computer Engineering Commons](#), and the [Electrical and Electronics Commons](#)

---

## Recommended Citation

Barton, Jay Houston, "Frequency Selective Surfaces For Extreme Applications" (2014). *Open Access Theses & Dissertations*. 809.  
[https://digitalcommons.utep.edu/open\\_etd/809](https://digitalcommons.utep.edu/open_etd/809)

This is brought to you for free and open access by DigitalCommons@UTEP. It has been accepted for inclusion in Open Access Theses & Dissertations by an authorized administrator of DigitalCommons@UTEP. For more information, please contact [lweber@utep.edu](mailto:lweber@utep.edu).

# FREQUENCY SELECTIVE SURFACES FOR EXREME APPLICATIONS

JAY HOUSTON BARTON

Department of Electrical and Computer Engineering

APPROVED:

---

Raymond C. Rumpf, Ph.D., Chair

---

Thompson Sarkodie-Gyan, Ph.D.

---

David Roberson, Ph.D.

---

Eric MacDonald, Ph.D.

---

Joseph Pierluissi, Ph.D.

---

Bess Sirmon-Taylor, Ph.D.  
Interim Dean of the Graduate School

Copyright ©

by

Jay H. Barton

2014

# FREQUENCY SELECTIVE SURFACES FOR EXTREME APPLICATIONS

by

JAY HOUSTON BARTON, B.S.E.E.

DISSERTATION

Presented to the Faculty of the Graduate School of

The University of Texas at El Paso

in Partial Fulfillment

of the Requirements

for the Degree of

DOCTOR OF PHILOSOPHY

Department of Electrical and Computer Engineering

THE UNIVERSITY OF TEXAS AT EL PASO

May 2014

## **Acknowledgements**

I would like to thank my committee and my family for helping along the way. I would also like to thank everyone at White Sands Missile Range SVAD who helped me achieve this, and put up with all my questions.

## **Abstract**

It is known that for high-power microwaves and other extreme environments, the use of resonant metallic elements in frequency selective surfaces can be problematic. The solution developed within this dissertation to solve these problems was to use guided-mode resonance phenomenon to create all-dielectric frequency selective surfaces that could survive these extreme environments.

To fully understand how these devices work, three different computational electromagnetic methods are formulated and implemented. The formulation of these methods start with the differential form of Maxwell's equation and are derived all the way down to the final simulation state. This is done sequentially and all the work is shown for comprehension and completeness.

These computational electromagnetic methods are then implemented into two different heuristic optimization algorithms. These optimization algorithms are used to develop three new and novel devices that solve the problems associated with all-dielectric frequency selective surfaces. All the devices developed in this work have been manufactured and experimentally tested. In the case of the high power devices, these were tested at the High Power Microwave Test Facility at White Sands Missile Range. One of the devices developed has the distinction of being the first known 3D printed all-dielectric frequency selective surface.

The devices developed in this work have survived environments where any known metallic frequency selective surfaces are destroyed and rendered useless. This work provides novel new frequency selective surfaces for these extreme applications.

## Table of Contents

|   |      |
|---|------|
| Acknowledgements.....   | iv   |
| Abstract.....   | v    |
| Table of Contents.....  | vi   |
| List of Figures.....  | viii |
| Chapter 1: Introduction to Microwave Frequency Selective Surfaces ..... | 1    |
| 1.1 History and applications of the frequency selective surfaces .....  | 1    |
| 1.2 Metallic frequency selective surfaces .....                         | 3    |
| 1.3 All-dielectric frequency selective surfaces .....                   | 6    |
| Chapter 2: Computational Electromagnetic Methods.....                   | 13   |
| 2.1 Finite-Difference Frequency-Domain.....                             | 13   |
| 2.2 Method of Lines.....  | 30   |
| 2.3 Rigorous Coupled-Wave Analysis.....                                 | 45   |
| Chapter 3: Numerical Optimization Techniques .....                      | 53   |
| 3.1 Introduction to FSS optimization.....                               | 53   |
| 3.2 Particle swarm optimization .....                                   | 56   |
| 3.3 Genetic algorithm optimization .....                                | 61   |
| Chapter 4: All-Dielectric FSS with Exiguous Periods.....                | 65   |
| 4.1 Device introduction.....  | 65   |
| 4.2 Baseline device design.....   | 66   |
| 4.3 Effect of finite length .....                                       | 68   |
| 4.4 Design approach.....  | 70   |
| 4.5 Experimental Results .....  | 72   |
| 4.6 Device conclusion.....  | 75   |
| Chapter 5: All-Dielectric FSS for HPM.....                              | 77   |
| 5.1 Device introduction.....  | 77   |
| 5.2 Design approach.....  | 78   |
| 5.3 PSO implementation .....  | 79   |
| 5.4 Finite length analysis .....  | 80   |
| 5.5 Optimized Crossed Grating FSS.....                                  | 82   |
| 5.6 Experimental Results .....  | 84   |
| 5.7 Device conclusion.....  | 88   |
| Chapter 6: 3D Printed All-Dielectric FSS for HPM Applications.....      | 90   |
| 6.1 Device introduction.....  | 90   |

|   |     |
|---|-----|
| 6.2 Phenotype generation.....   | 91  |
| 6.3: Device design.....   | 95  |
| 6.4 Experimental results and manufacture.....   | 98  |
| 6.5 Device conclusion.....  | 105 |
| Chapter 7: Conclusion and Future Work .....   | 106 |
| 7.1 Conclusion .....  | 106 |
| 7.2 Future work.....  | 108 |
| References.....   | 110 |
| Appendix.....   | 115 |
| A1: Normalization of the magnetic field component. ....                               | 115 |
| A2: Example derivative operator matrices with periodic boundary conditions .....      | 116 |
| A3: Derivation of the 2D FDFD wave equations .....                                    | 118 |
| A4: Derivation of the MOL PQ matrix equations .....                                   | 119 |
| A5: Derivation of the scattering matrix terms .....                                   | 120 |
| A6: Derivation of Redheffer's star product .....                                      | 125 |
| A7: Derivation of the longitudinal field component from the divergence equation. .... | 128 |
| Vita.....   | 129 |

## List of Figures

|   |    |
|---|----|
| Figure 1.1: Examples of FSSs currently in use.....  | 2  |
| Figure 1.2: Two examples of metallic FSSs. ....   | 4  |
| Figure 1.3: Dipole vs Slot array metallic FSS. ....   | 5  |
| Figure 1.4: Example all-dielectric FSS with associated spectra.....                             | 8  |
| Figure 1.5: A grating diffracts a wave into a set of discrete spatial harmonics.....            | 9  |
| Figure 1.6: Regions of resonance for the all-dielectric FSS described.....                      | 11 |
| Figure 1.7: Illustration of the physical mechanisms leading to guided-mode resonance.....       | 11 |
| Figure 2.1: Example of a central finite-difference approximation.....                           | 14 |
| Figure 2.2: Representation of a 3D Yee grid show staggered field components in space.....       | 15 |
| Figure 2.3: Illustration of a 2D Yee grid.....  | 15 |
| Figure 2.4: 3D simulation space example.....  | 19 |
| Figure 2.5: Illustration of a FDFD simulation space.....  | 27 |
| Figure 2.6: Illustration of a multilayer device.....  | 31 |
| Figure 2.7: Scattering matrix showing transmission and reflection of a incidence wave.....      | 37 |
| Figure 2.8: Scattering matrix showing the $i$ layer.....  | 37 |
| Figure 2.9: Illustration of the calculation of the global scattering matrix.....                | 42 |
| Figure 2.10: Illustration of the RCWA method.....   | 46 |
| Figure 3.2: Solution space of example all-dielectric FSS.....                                   | 55 |
| Figure 3.3: PSO particles randomly placed in a 2D solution space.....                           | 56 |
| Figure 3.4: Illustration of the inertia term.....   | 58 |
| Figure 3.5: Illustration of the cognitive term.....   | 59 |
| Figure 3.6: Illustration of the social term.....  | 60 |
| Figure 3.7: Illustration of the GAO method.....   | 62 |
| Figure 3.8: Illegitimate child phenotype generation.....  | 63 |
| Figure 4.1: Three step design procedure for an infinitely periodic all-dielectric FSS.....      | 67 |
| Figure 4.2: Baseline all-dielectric FSS design and its simulated performance.....               | 68 |
| Figure 4.3: Response of a all-dielectric FSS with varying number of periods.....                | 69 |
| Figure 4.4: Construction and operational principal of a exiguous-period all-dielectric FSS..... | 71 |
| Figure 4.5: Double parameter sweep for a 7 period all-dielectric FSS.....                       | 72 |
| Figure 4.6: Final design of 7 period all-dielectric FSS.....                                    | 73 |
| Figure 4.7: All-dielectric FSS with mounted reflectors inside a anechoic chamber.....           | 73 |
| Figure 4.8: Measured transmittance with and without reflectors of the all-dielectric FSS.....   | 74 |
| Figure 4.9 Measured transmittance and simulated spectra.....                                    | 75 |
| Figure 5.1: Illustration of finding the maximum bandwidth and transmittance.....                | 79 |
| Figure 5.2: PSO designed ruled grating all-dielectric FSS.....                                  | 81 |
| Figure 5.3: Ruled grating spectral response at TE polarization.....                             | 82 |
| Figure 5.4: PSO designed crossed grating all-dielectric frequency selective surface. 0.....     | 83 |
| Figure 5.5: Transmittance of all-dielectric FSS.....  | 83 |
| Figure 5.6: Field-of-view response for a center resonant frequency of 10.6 GHz.....             | 84 |
| Figure 5.7: All-dielectric FSS under test.....  | 85 |
| Figure 5.8: Experimental spectral response of the all-dielectric FSS.....                       | 86 |
| Figure 5.9: Field-of-view sweep of the all dielectric FSS.....                                  | 87 |
| Figure 5.10: Time domain response of the all-dielectric FSS illuminated.....                    | 88 |
| Figure 6.1: Example phenotype.....  | 92 |

|  |     |
|--|-----|
| Figure 6.2: This figure shows the generated 2D data array of random numbers.....             | 93  |
| Figure 6.3: This figure shows the truncated FFT 2D data array.....                           | 93  |
| Figure 6.4: In this figure the normalized truncated IFFT 2D grid. ....                       | 94  |
| Figure 6.5: Final GAO optimized device.....  | 96  |
| Figure 6.6: Transmittance spectra of the GAO optimized device. ....                          | 97  |
| Figure 6.7: FOV sweep of the optimized FSS. ....   | 98  |
| Figure 6.8. Transmittance spectra of GAO device .....  | 98  |
| Figure 6.8: Completed 3D printed FSS.....  | 100 |
| Figure 6.9: Powder packed 3D printed FSS.....  | 101 |
| Figure 6.10: Experimental testing of 3D printed FSS.....                                     | 102 |
| Figure 6.11: Experimental spectra of 3D printed FSS. ....                                    | 102 |
| Figure 6.12: Experimental FOV sweep of 3D printed FSS. ....                                  | 103 |
| Figure 6.13: Problems highlighted with powder packing.....                                   | 104 |
| Figure 6.14: Simulation spectra, corrected simulation spectra and experimental spectra ..... | 104 |
| Figure 7.1: Examples of 3D generated phenotypes. ....  | 108 |
| Figure 7.2: Example of a conformal 3D FSS.....   | 109 |

## **Chapter 1: Introduction to Microwave Frequency Selective Surfaces**

This chapter introduces the concepts of frequency selective surfaces, what they are, how they work, and what they are used for. A brief history is given and the two distinct types of frequency selective surfaces are described. The physical basis on how these devices work is explained and a summary of what challenges they both have and what needs to be solved is expanded on.

The all-dielectric frequency selective surfaces introduced in this chapter illustrate a novel, new approach on how microwaves can be filtered in extremely high-powered environments. This type of frequency selective surfaces had its own unique set of challenges that needed to be overcome to make this a viable technology in the high-power microwave field.

### **1.1 History and applications of the frequency selective surfaces**

First developed in the early 1900s by Guglielmo Marconi, frequency selective surfaces (FSSs) have been in use for many years [1]. These devices are used to filter electromagnetic waves passively by using the interference caused by periodic arrays of multiple materials, metallic elements or a combination of both on the incidence plane [2]. This interference causes a frequency selective response, filtering certain frequencies while letting others pass. These devices are also known to be able to filter angular spectrum as well, allowing waves at only the appropriate angles of incidence to propagate [3].

Introduced to the public during the United States first Gulf War, the Lockheed F-117 Nighthawk boosted interest in stealth and the frequency selective surface. The Nighthawk stealth aspect was designed using a combination of diffraction, radio frequency (RF) absorbent materials and FSSs [4]. While modification of radar cross section is considered the most publically exciting application of this technology, FSSs have many other uses. They have been used in radomes [5], dichroic sub-reflectors [6], lenses [7], radio frequency identification (RFID) [8], and protection from electromagnetic interference.

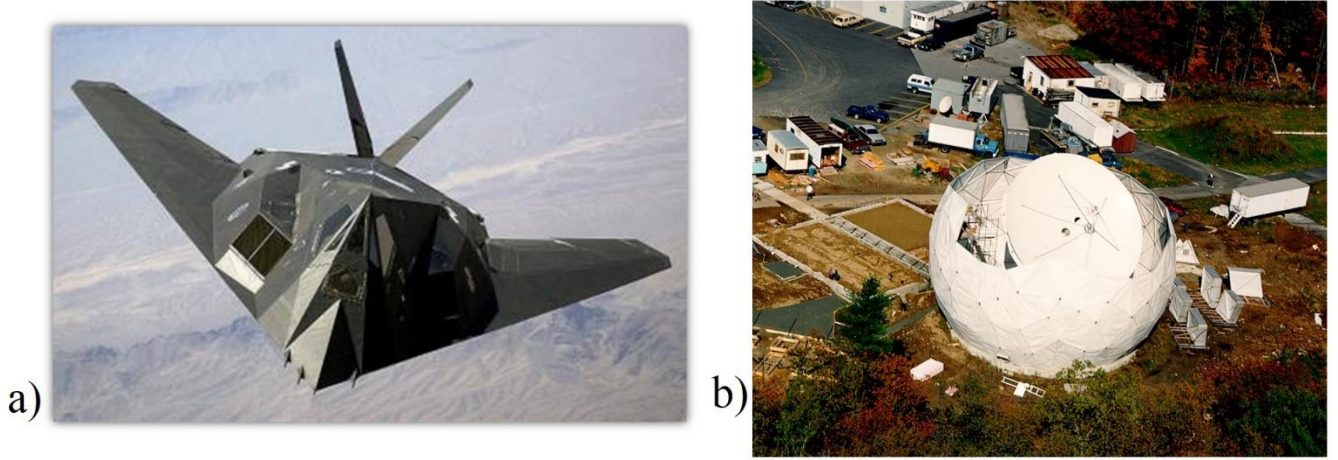


Figure 1.1: Examples of FSSs currently in use. a) Lockheed F-117 Nighthawk stealth fighter [9].  
b) Radome being constructed for NASA's Orbital DEbris RADar Calibration Spheres (ODERACS) [9].

Metallic FSSs are very good at filtering microwaves, but with the rise in space communications and pulsed power technologies, these FSSs are not able to handle the power generated in these types of systems [11]. Flashover and arcs caused by field enhancement, ohmic heating, and explosive electron emission, [12] and [13], are very common problems when using these device in high-power applications. This destructive phenomenon leads to many undesirable effects to the FSS such as pattern disruption and damage. Very recently, efforts have been made to encapsulate a miniature element FSS in a dielectric with a high breakdown voltage to raise the peak electric field the device can handle [14]. In ref [14], Li et al employed a miniaturized-element FSS to reduce the amplitude of the local electric field and tested their device at a peak power of 25 kW. Their FSS was cleverly composed of alternating layers of dielectric and metal grids so as to separate the capacitive and inductive layers. While this method works for peak powers of approximately 25 kW, anything higher has the same detrimental phenomenon as the traditional FSS.

The work described within this paper introduces a novel, and exciting type of frequency selective surfaces using only dielectrics. Borrowing ideas and devices traditionally used in optics,

all-dielectric frequency selective surfaces were designed, optimized, manufactured and tested at microwave frequencies. These devices have the distinct advantage of working at extraordinary power levels exceeding  $1 \text{ GW/m}^2$ . While these all-dielectric FSSs can handle vast amounts power they come with their own set of unique challenges that had to be overcome. Overcoming these challenges led to the formulation and coding of three different computational electromagnetic techniques and two numerical optimization algorithms.

Using a genetic algorithm optimization and fast Fourier transforms (FFT), an interesting and new type of all-dielectric device was designed exploiting the complex geometries that could never be manufactured before that are enabled by 3D printing. This device is the first known fully functional 3D printed all-dielectric FSS. The 3D printed device was able to withstand MWs of power while minimizing beam distortion in the pass-band at high-power. Being able to withstand these extreme environments, this FSS has the potential to be used in many applications in high-power RADAR and HPM protection systems. The methodology used to design this FSS has the potential to yield much better devices as the technology of 3D printing and computation power of computers evolves.

## **1.2 Metallic frequency selective surfaces**

Traditionally, frequency selective surfaces have been defined as “a periodic array of identical elements arranged as a one or two dimensional array” of metallic structures [4]. While this definition is extremely broad, all the possible combinations of “periodic arrays of identical elements” can be categorized into two distinct subclasses, dipole arrays and slot arrays. Examples of these two subclasses can be seen in Figure 1.2. Shown within this figure are two periodic arrays of metallic elements and slots on a dielectric substrate.

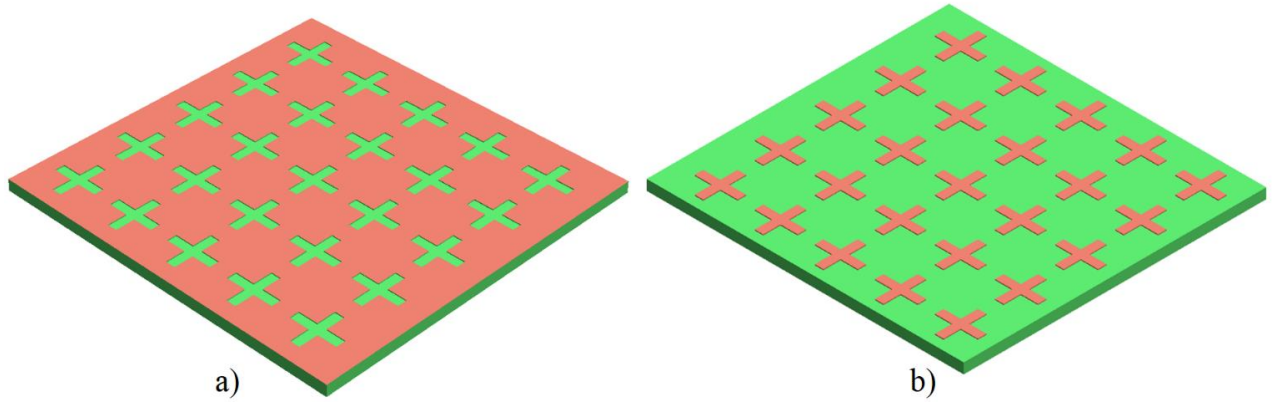


Figure 1.2: Two examples of metallic FSSs. a) Slot array on a dielectric sheet. b) Dipole array on a dielectric sheet.

Within the dipole subclass of the FSSs lies a great variety of geometries that further diversifies the type of shapes these devices can have. Through all the diversity in geometry the physical phenomenon on how they operate is the same. When an incident plane wave hits the dipole array FSS, it excites the metallic elements with electric currents causing the electrons within the elements to start oscillating. This electron oscillation in turn starts producing its own radiating electric fields as a array of tiny radiating antennas. It is the interference of this element radiation with the incident plane wave that produces the frequency selectivity response in these devices.

The slot array subclass is the same as the dipole array except for one key difference. Instead of inducing oscillating electric currents on metallic elements, the incident plane wave induces oscillating magnetic currents on the metallic surface. These oscillating magnetic currents in turn cause the surface to start radiating its own field. Like the dipole array it is the interference of this surface radiation with the incident plane wave that produces the frequency selectivity response in these devices.

There is a very interesting relationship between the dipole and slot array FSSs. In most cases the dipole array acts as a band-stop filter while its complimentary slot array as a band-pass. This is known as Babinet's principal [15]. Figure 1.2 is a perfect example of what complimentary FSSs look like. Babinet's principle is very important in the design and study of metallic FSSs as it provides an intuitive example that helps in understanding the physics behind these types of FSSs.

To illustrate Babinet's principal, a simulation was performed using a numerical modeling technique known as method of lines. In this simulation a simple cross dipole array was created and modeled. The cross dipole was given the same thickness as what is normal traces on PCB and the dielectric constant of the substrate was the same as the materials used in typical PCBs. The dimensions of the dipole array was optimized using a gradient descent method to put its resonance right on the normalized wavelength. Its complimentary slot array was then simulated. This can be seen in Figure 1.3.

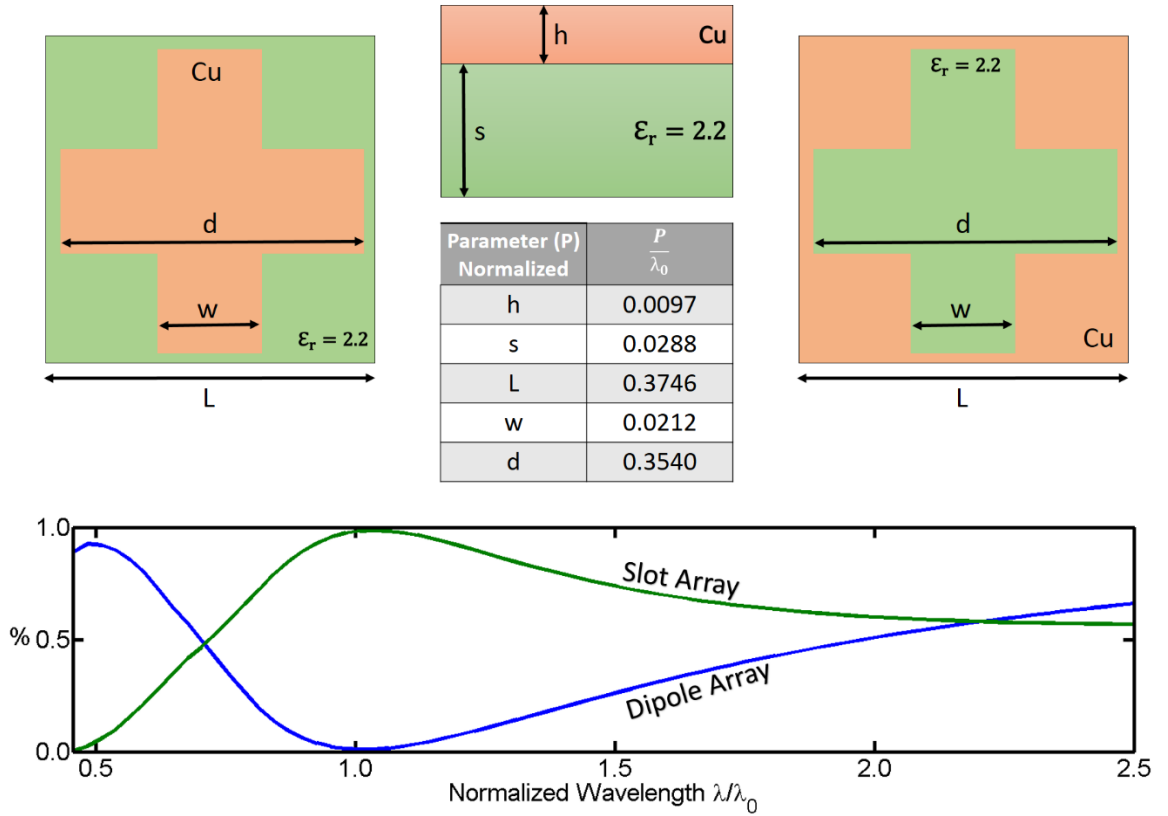


Figure 1.3: Dipole vs Slot array metallic FSS.

Shown in Figure 1.3 are the transmittance spectra of the two devices, a dipole and slot array FSSs. The dipole array is acting as a band-stop filter while its complimentary slot array acts as a band-pass.

The metallic FSS provides a great amount bandwidth and is relatively insensitive to angle of incidence. This is in part to the way that the incident electromagnetic waves interact more strongly with metals than they do with dielectrics. Though spectra wise these devices are very good, there are flaws that can severely affect their performance. One of the flaws is that these devices are usually composite devices, metal traces sitting on a dielectric slab. This can lead to delamination and layer separation problems when they are put in non-ideal environments which include, high vibrations, rapid temperature fluctuations, and moisture [16], [17]. These types of environments are very common on the outside of aircraft, naval vehicles and other types of machinery. Delamination can severely impact performance and in the case of high-power applications like RADAR, causing catastrophic damages to the FSS. The other important flaw with this technology is also due to its greatest strength, its strong interaction with metals. In high-power environments, metals have a tendency to experience explosive electron emission and plasma generation [12]. The electric fields of these metallic FSSs collect at the edges of the elements and magnify, leading to breakdowns in the air and dielectric [11]. These breakdowns have the potential to destroy the FSS, rendering it useless, and distort the incoming/outgoing waves. Recent progress has shown that clever engineering of the inductance and capacitance of these devices can drastically improve the durability in high-power environments [14], but it can't compare to the all-dielectric alternative in power handling capability. In conclusion, for low-power and stable environments, like the inside of a receiving antenna's radome, metallic FSSs provide superior spectra response and performance. For extreme and high voltage environments, these devices breakdown and cease working.

### **1.3 All-dielectric frequency selective surfaces**

Within the all-dielectric frequency selective surface spectrum there are several different technologies that can be used. These include, stacks of dielectric layers, naturally absorbing materials, and devices that use guided-mode resonance.

Using stacks of dielectric layers, one can create distributed Bragg reflectors to achieve a frequency selective response [18]. These filters provide a broadband response and can be made to provide a large amount of suppression to transmitted power. The Bragg reflector is a very good technology for application in the optical frequency ranges. The thickness of the layers used in these device is often on the order of a quarter of a wavelength and 100s of them are needed to achieve the desired response. In optical frequencies, this has no consequence. In the radio frequency ranges, this leads to prohibitively large sizes. These device are also made of composite materials, alternating dielectric layers, which would have the same problems with delamination as metallic FSSs. Because of these limitations, a different type of all-dielectric FSS needed to be used.

Naturally absorbing materials can provide a very large broadband response and depending on the amount of loss in the material, can have large amounts of suppression to the transmitted power [19]. These materials are very lossy, as this is the main mechanism used to provide a filtering response. While this provides a very large broadband response, it makes the ability to create notch filters, and transmit out of band almost impossible. The loss in these materials is also very problematic in high-power environments as the loss experienced is turned to heat. If not taken into consideration this can have an extremely detrimental effect to the device. Because of these limitations and the limitation associated with other all-dielectric FSS technologies, guided-mode resonance was chosen as the filtering phenomenon for use in this research.

A type of all-dielectric frequency selective surface, also known as a guided-mode resonance (GMR) filter, is formed whenever a slab waveguide and a grating are brought into close proximity so that they are electromagnetically coupled [20]-[22]. The bandwidth of these FSSs can be made arbitrarily small by reducing the contrast of the grating and slab, while the filter response can be made symmetric with virtually no ripple outside of the pass band for both transmission and reflection type filters. Efficiency on these FSSs can approach 100% on resonance and devices can be constructed with multiple resonances to increase bandwidth. A simple example all-dielectric FSS was generated to show the reader exactly what one of these devices looks like and what the typical spectra is. This can be seen in Figure 1.4.

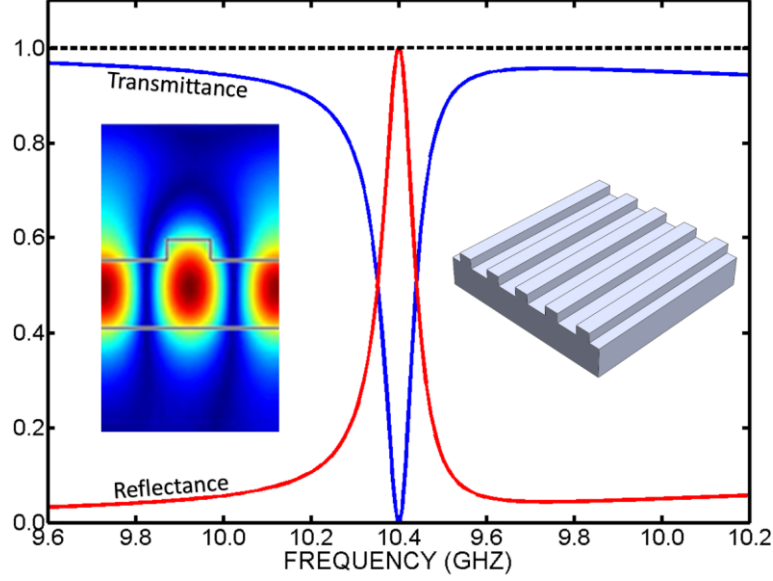


Figure 1.4: Example all-dielectric FSS with associated spectra. On the left side the guided-mode resonance can be seen and on the right the device itself. The field shown is from 10.4 GHz.

There are two physical mechanisms occurring simultaneously and each must be understood to fully explain guided-mode resonance. The first is diffraction from a grating as illustrated in Figure 1.5. In this figure it can be seen that an incident plane-wave diffracts into a quantifiable number of spatial harmonics when it is incident on a grating. The amplitudes of the diffracted harmonics are found by solving Maxwell's equations, while the directions are quantified through the grating equation [24]. Eq. (1.3.1) shows the grating equation.

$$\sqrt{\epsilon_{\text{avg}}} \sin \theta_m = \sqrt{\epsilon_{\text{inc}}} \sin \theta_{\text{inc}} - m \frac{\lambda_0}{\Lambda} \quad (1.3.1)$$

In this equation,  $\epsilon_{\text{avg}}$  is the average dielectric constant where the direction of the spatial harmonics are being calculated,  $\epsilon_{\text{inc}}$  is the dielectric constant outside the all-dielectric FSS,  $\theta_m$  is the angle of the  $m^{\text{th}}$  spatial harmonic,  $\theta_{\text{inc}}$  is the angle of incidence of the applied wave,  $\lambda_0$  is the free space wavelength, and  $\Lambda$  is the period of the grating.

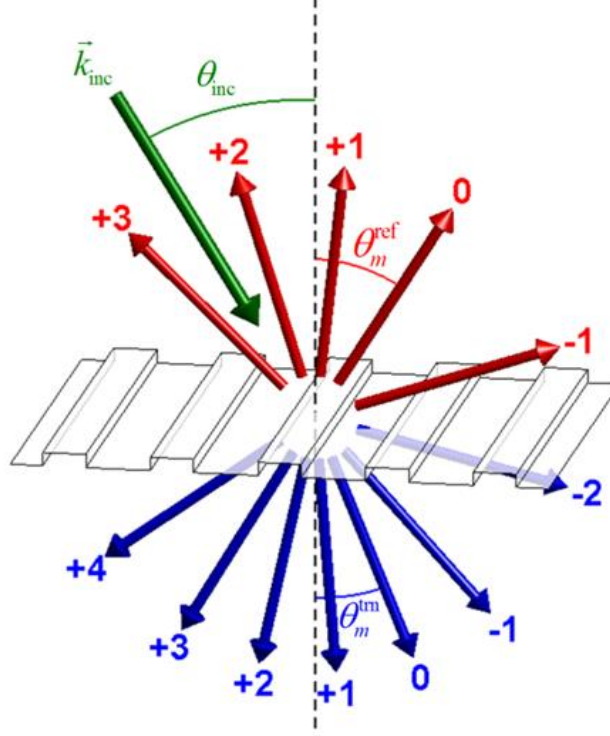


Figure 1.5: A grating diffracts a wave into a set of discrete spatial harmonics [23].

Gratings with periods longer than the wavelength will diffract into more than one harmonic. The angles of the spatial harmonics depend on the diffraction order, materials, wavelength, and grating period. These angles are calculated from the grating equation.

The second mechanism is guiding within the slab. Wave guiding can only occur when the effective refractive index of the guided-mode is greater than the surrounding media and less than the refractive index of the slab itself. This condition can be quantified in terms of dielectric constant as

$$\sqrt{\epsilon_{\text{inc}}} \leq \left| \frac{\beta_m}{k_0} \right| < \sqrt{\epsilon_{\text{avg}}} \quad (1.3.2)$$

where  $k_0$  is the free space wave number and  $\beta_m$  is the propagation constant of the  $m^{\text{th}}$  order mode. From the ray-tracing view of a slab waveguide, a guided-mode can be envisioned as a ray propagating at an angle  $\theta_m$  within the slab. This is related to the propagation constant through

$$\frac{\beta_m}{k_0} = \sqrt{\epsilon_{\text{avg}}} \sin \theta_m \quad (1.3.3)$$

Guided-mode resonance occurs only when the angle of the diffracted spatial harmonic- matches exactly that of a guided-mode in the slab. At resonance, the propagation constant can be related to the angle of incidence by substituting Eq. (1.3.3) into Eq. (1.3.1). A condition for guided-mode resonance is derived by combining this with Eq. (1.3.2). This leads to the formulation of Eq. (1.3.4)

$$\sqrt{\epsilon_{\text{inc}}} \leq \left| \sqrt{\epsilon_{\text{inc}}} \sin \theta_{\text{inc}} - m \frac{\lambda_0}{\Lambda} \right| < \sqrt{\epsilon_{\text{avg}}} \quad (1.3.4)$$

Equation (1.3.4) can be used to identify the regions of resonance as a function of angle of incidence and grating period. A diagram illustrating this relation was generated for the all-dielectric FSS described in Figure 1.4 and is shown in Figure 1.6.

Some important attributes of all-dielectric FSSs can be observed in this diagram. First, the positions of the resonances are a function of the angle of incidence,  $\theta_{\text{inc}}$ , and grating period,  $\Lambda$ . Second, the number of resonances increases as the grating period is increased relative to the wavelength due to the existence of multiple spatial harmonics.

With this background, the overall operation of the all-dielectric FSS can be understood. An applied wave is diffracted by the grating into a number of discrete spatial harmonics. When a precise phase matching condition is satisfied, a diffracted harmonic exactly matches a guided-mode supported by the slab waveguide and a resonance is excited over a narrow band of frequencies. At resonance, the applied wave is partially coupled into the guided-mode across the entire aperture of the FSS. The remaining power is either reflected or transmitted through the FSS. The portion of power coupled into the guided-mode propagates through the slab waveguide, but leaks out across the aperture from the slab due to the interaction with the grating.

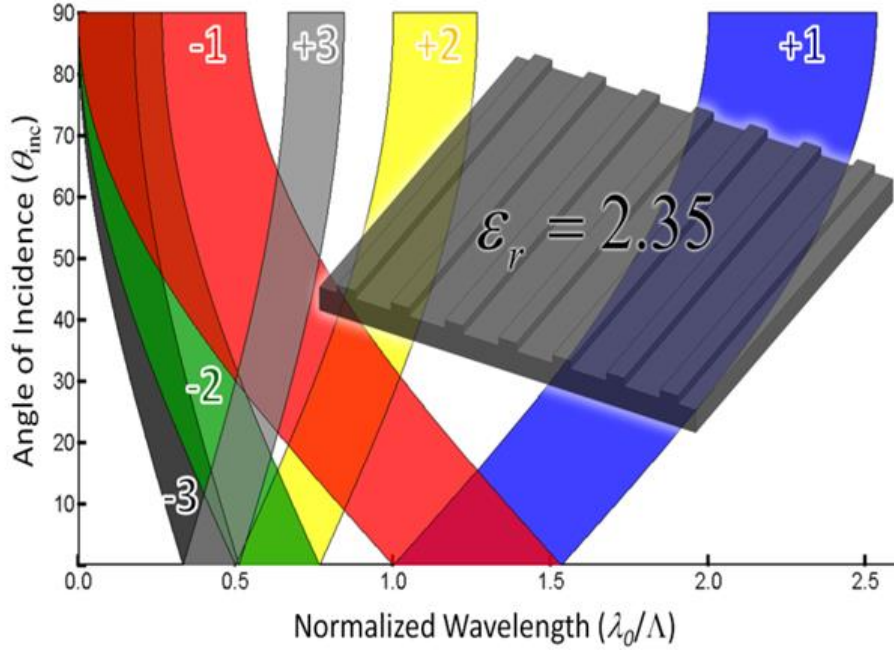


Figure 1.6: Regions of resonance for the all-dielectric FSS described [23].

This leakage is a necessary condition to satisfy the reciprocity theorem [26]. Waves out-coupled on either side of the FSS combine out of phase with reflected and transmitted portions of the applied wave to produce an overall frequency response. The guided-mode resonance concept is illustrated in Figure 1.7. Outside of the FSS, the diagram shows the incident, reflected, and transmitted waves. Inside the slab, ray traced versions of the guided-modes are shown.

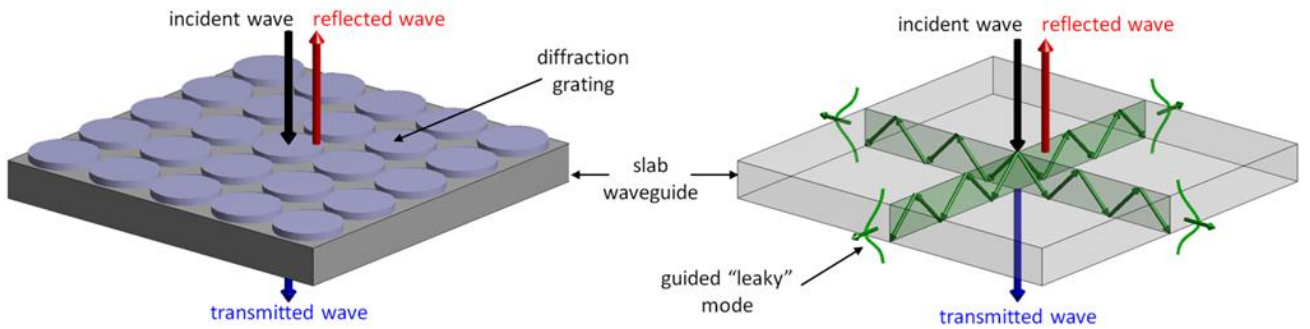


Figure 1.7: Illustration of the physical mechanisms leading to guided-mode resonance in all-dielectric FSSs [23].

Being monolithic and made entirely from dielectric, these FSSs do not suffer from the same problems as their metallic counterparts. Their monolithic design makes them very robust to vibration, temperature fluctuations and other environmental conditions. The completely dielectric construction works very well in high-power environment because of the higher breakdown voltage intrinsic to some dielectrics and because the fields disperse more evenly and have less interaction within the dielectrics than they do with metals. That being said, all-dielectric FSSs come with their own set of challenges that need to be overcome, to make them a viable alternative to their metallic brethren.

The first challenge is all-dielectric FSSs are almost always designed assuming that the grating is infinitely periodic. Due to the physics of guided-mode resonance, devices must often be hundreds of grating periods long for a finite-size structure to approach the performance of the infinitely periodic structure [27]. At radio frequencies, this often leads to prohibitively large devices that are dozens of meters in length and makes it very difficult to produce a strong frequency response in a competing form factor.

The other challenge with these devices is their bandwidth and field-of-view (FOV) are prohibitively narrow, with a fractional bandwidth (FBW) typically less than 1% and FOV often much less than  $1^\circ$ . The FBW and FOV limitation leads to problems for this technology's use in applications that require broadband performance, such as ultra-wideband radar [28]-[30].

The work described within this dissertation solves these challenges and provides 3 novel designs using GMR that have been optimized, manufactured and fully tested. These devices show that this type of FSS can be a viable, and in cases, a better alternative to metallic FSSs.

## Chapter 2: Computational Electromagnetic Methods

To be able to effectively study and develop different types of FSSs, methods need to be developed that can solve Maxwell's equations to predict their electromagnetic behavior. This chapter provides three different methods that can be used to effectively simulate any type of FSS, be it metallic or dielectric.

These computational electromagnetic methods all start with the differential form of Maxwell's equations and then are derived all the way down to the final simulation state. This allows for easy comprehension on how the methods work and its implementation. Each method is broken down and explained. The pros and cons are given for what the method can handle and suggestions for what method should be used to model different types of FSSs.

### 2.1 Finite-Difference Frequency-Domain

The finite-difference frequency domain (FDFD) method is a fully numerical modeling technique used to simulate the electromagnetic interaction and response of different materials and complex devices in the frequency domain [25], [31] - [34]. It provides a completely rigorous and vectorized solution to Maxwell's equations. This method has the advantages in that the electric fields can be inherently visualized with no additional steps, it can easily simulate metals and high dielectric constant materials and it intrinsically handles different angles of incidence. Being a frequency-domain method using discrete frequency points, it can easily and quickly detect and resolve very narrow resonances. This makes it ideal for the study of 2D all-dielectric FSSs using GMR.

To be able to formulate this method, three very important concepts need to be addressed. The first is the concept of the finite-difference approximation of a derivative. In this formulation, a first order derivative is approximated using a central finite-difference [35]. This simple type of finite-difference is just the second point on an arbitrary function subtracted from the first and divided by the difference between them as illustrated in Figure 2.1.

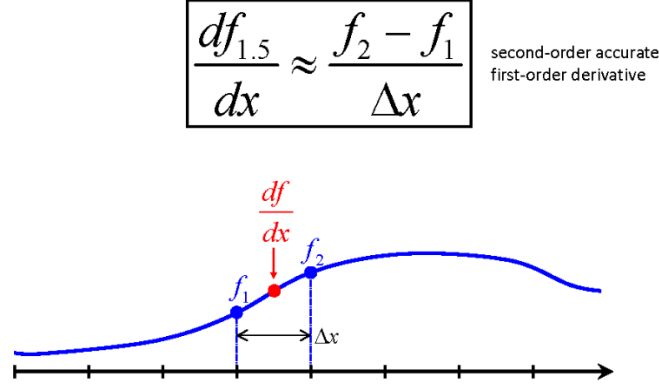


Figure 2.1: Example of a central finite-difference approximation of a second-order accurate first-order derivative. Courtesy of [36].

This is the type of finite-difference used to approximate the partial differential equations (PDEs) later derived from Maxwell's equations. Because this type of operation is linear, it can be transformed into a matrix operator. This is a very important step in the formulation of this method in that it greatly simplifies the math and “book keeping” needed for implementation.

The second concept is the formulation of the Yee grid [37]. This concept was first developed for the finite-difference time domain (FDTD) method [38]. In this method, the computational grid is split into two different grids, a grid for the E-field and one for the H-field. First the E-field is calculated and then from this calculated E-field the H-field is calculated. This sequence is repeated throughout the grid simulating the propagation of an electromagnetic wave. The consequence of this type of simulation is that the fields are staggered in space and time. The Yee grid can be seen in Figure 2.2. This figure shows the six field components staggered on a Yee grid. Though developed for FDTD, this concept is also used for the FDFD method as it solves the problems associated with using a collocated grids [37].

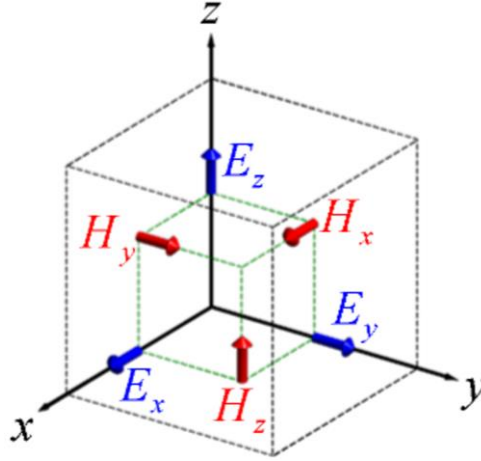


Figure 2.2: Representation of a 3D Yee grid show staggered field components in space [36].

The third and final concept is a purely personal one for the author, the naming convention of the different types of polarization of a linearly polarized wave. Traditionally the two labels for linearly polarized waves have been TE and TM modes. The definition of these two labels are based on the lack of field in the direction of propagation. The TE, transverse electric, mode has no electric field in the direction of propagation, while the same is true for the TM, transverse magnetic, mode with the magnetic fields. For some scenarios and certain wave angle-of-incidences, this definition falls apart with both the TE and TM modes fulfilling the given definition. It is more intuitive to define the modes based on the field that is in the  $z$  direction of propagation. Doing this, there is no question to what polarization the wave is propagating. Therefore throughout this chapter the author uses the nomenclature of  $E_z$  for the traditional TM-mode and  $H_z$  for the TE-mode.

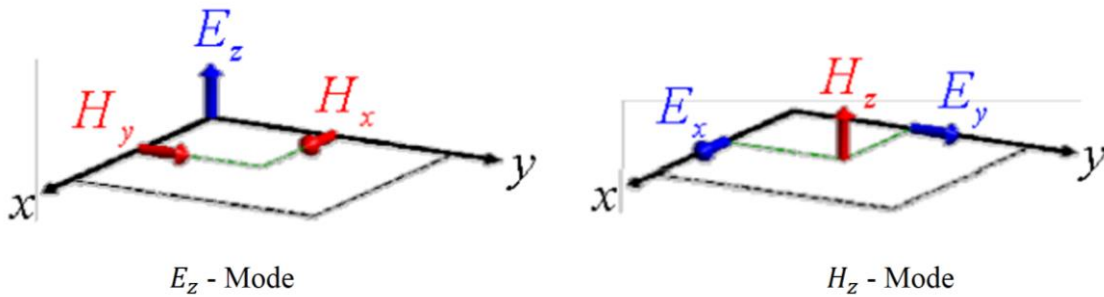


Figure 2.3: Illustration of a 2D Yee grid showing E and H mode with their transverse components [36].

The formulation for the FDFD method begins with the differential form of Maxwell's Equations in the frequency domain. Specifically the curl equations are used. The divergence equations are not used as there are no free charges being built into this model and this is taken care of through the use Yee grid.

$$\begin{aligned}\nabla \times \vec{E} &= -j\omega[\mu]\vec{H} \\ \nabla \times \vec{H} &= j\omega[\varepsilon]\vec{E}\end{aligned}\tag{1.3.5}$$

From here the magnetic field is normalized using the following variable.

$$\tilde{H} = -j\sqrt{\frac{\mu_0}{\varepsilon_0}}\vec{H}\tag{1.3.6}$$

This new magnetic field value is then substituted into the equations in (1.3.5) to normalize the values leading to the equations

$$\nabla \times \vec{E} = k_0[\mu_r]\tilde{H}\tag{1.3.7}$$

$$\nabla \times \tilde{H} = k_0[\varepsilon_r]\vec{E}\tag{1.3.8}$$

where  $[\varepsilon_r]$  is the relative permittivity tensor,  $[\mu_r]$  is the relative permeability tensor and

$$k_0 = \omega\sqrt{\mu_0\varepsilon_0}\tag{1.3.9}$$

This normalization was done to bring the magnitude of the  $\tilde{H}$  field into the same order of magnitude as that of the  $\vec{E}$ . By doing this, the rounding error occurred during simulation can be minimized. Another product of this normalization is that the complex number  $j$  is canceled. This leads to an easier to understand formulation. The arithmetic used in this normalization can be viewed in Appendix A1.

After normalization, the curl equations are expanded into their Cartesian form.

$$\begin{aligned}
\frac{\partial \vec{E}_z}{\partial y} - \frac{\partial \vec{E}_y}{\partial z} &= k_0 \left( \mu_{xx} \tilde{H}_x + \mu_{xy} \tilde{H}_y + \mu_{xz} \tilde{H}_z \right) \\
\nabla \times \vec{E} = k_0 [\mu_r] \tilde{H} &\rightarrow \frac{\partial \vec{E}_x}{\partial z} - \frac{\partial \vec{E}_z}{\partial x} = k_0 \left( \mu_{yx} \tilde{H}_x + \mu_{yy} \tilde{H}_y + \mu_{yz} \tilde{H}_z \right) \\
\frac{\partial \vec{E}_y}{\partial x} - \frac{\partial \vec{E}_x}{\partial y} &= k_0 \left( \mu_{zx} \tilde{H}_x + \mu_{zy} \tilde{H}_y + \mu_{zz} \tilde{H}_z \right)
\end{aligned} \tag{1.3.10}$$

$$\begin{aligned}
\frac{\partial \tilde{H}_z}{\partial y} - \frac{\partial \tilde{H}_y}{\partial z} &= k_0 \left( \varepsilon_{xx} \vec{E}_x + \varepsilon_{xy} \vec{E}_y + \varepsilon_{xz} \vec{E}_z \right) \\
\nabla \times \tilde{H} = k_0 [\varepsilon_r] \vec{E} &\rightarrow \frac{\partial \tilde{H}_x}{\partial z} - \frac{\partial \tilde{H}_z}{\partial x} = k_0 \left( \varepsilon_{yx} \vec{E}_x + \varepsilon_{yy} \vec{E}_y + \varepsilon_{yz} \vec{E}_z \right) \\
\frac{\partial \tilde{H}_y}{\partial x} - \frac{\partial \tilde{H}_x}{\partial y} &= k_0 \left( \varepsilon_{zx} \vec{E}_x + \varepsilon_{zy} \vec{E}_y + \varepsilon_{zz} \vec{E}_z \right)
\end{aligned} \tag{1.3.11}$$

The grid upon which the device will be built and simulated is then normalized canceling out the  $k_0$  value.

$$x' = k_0 x \quad y' = k_0 y \quad z' = k_0 z \tag{1.3.12}$$

Eq. (1.3.12) is then substituted into Eqs. (1.3.10) and (1.3.11) leading to

$$\begin{aligned}
\frac{\partial \vec{E}_z}{\partial y'} - \frac{\partial \vec{E}_y}{\partial z'} &= \mu_{xx} \tilde{H}_x + \mu_{xy} \tilde{H}_y + \mu_{xz} \tilde{H}_z \\
\frac{\partial \vec{E}_x}{\partial z'} - \frac{\partial \vec{E}_z}{\partial x'} &= \mu_{yx} \tilde{H}_x + \mu_{yy} \tilde{H}_y + \mu_{yz} \tilde{H}_z \\
\frac{\partial \vec{E}_y}{\partial x'} - \frac{\partial \vec{E}_x}{\partial y'} &= \mu_{zx} \tilde{H}_x + \mu_{zy} \tilde{H}_y + \mu_{zz} \tilde{H}_z
\end{aligned} \tag{1.3.13}$$

$$\begin{aligned}
\frac{\partial \tilde{H}_z}{\partial y'} - \frac{\partial \tilde{H}_y}{\partial z'} &= \varepsilon_{xx} \vec{E}_x + \varepsilon_{xy} \vec{E}_y + \varepsilon_{xz} \vec{E}_z \\
\frac{\partial \tilde{H}_x}{\partial z'} - \frac{\partial \tilde{H}_z}{\partial x'} &= \varepsilon_{yx} \vec{E}_x + \varepsilon_{yy} \vec{E}_y + \varepsilon_{yz} \vec{E}_z \\
\frac{\partial \tilde{H}_y}{\partial x'} - \frac{\partial \tilde{H}_x}{\partial y'} &= \varepsilon_{zx} \vec{E}_x + \varepsilon_{zy} \vec{E}_y + \varepsilon_{zz} \vec{E}_z
\end{aligned} \tag{1.3.14}$$

From here an assumption is made that this model will only use diagonally anisotropic materials.

This converts the material tensors to the following form:

$$\begin{bmatrix} \epsilon_{xx} & \epsilon_{xy} & \epsilon_{xz} \\ \epsilon_{yx} & \epsilon_{yy} & \epsilon_{yz} \\ \epsilon_{zx} & \epsilon_{zy} & \epsilon_{zz} \end{bmatrix} \rightarrow \begin{bmatrix} \epsilon_{xx} & 0 & 0 \\ 0 & \epsilon_{yy} & 0 \\ 0 & 0 & \epsilon_{zz} \end{bmatrix} \quad (1.3.15)$$

$$\begin{bmatrix} \mu_{xx} & \mu_{xy} & \mu_{xz} \\ \mu_{yx} & \mu_{yy} & \mu_{yz} \\ \mu_{zx} & \mu_{zy} & \mu_{zz} \end{bmatrix} \rightarrow \begin{bmatrix} \mu_{xx} & 0 & 0 \\ 0 & \mu_{yy} & 0 \\ 0 & 0 & \mu_{zz} \end{bmatrix} \quad (1.3.16)$$

Substituting Eq. (1.3.15) and Eq. (1.3.16) into Eqs. (1.3.13) and (1.3.14) yields

$$\begin{aligned} \frac{\partial \vec{E}_z}{\partial y'} - \frac{\partial \vec{E}_y}{\partial z'} &= \mu_{xx} \tilde{H}_x \\ \frac{\partial \vec{E}_x}{\partial z'} - \frac{\partial \vec{E}_z}{\partial x'} &= \mu_{yy} \tilde{H}_y \\ \frac{\partial \vec{E}_y}{\partial x'} - \frac{\partial \vec{E}_x}{\partial y'} &= \mu_{zz} \tilde{H}_z \end{aligned} \quad (1.3.17)$$

$$\begin{aligned} \frac{\partial \tilde{H}_z}{\partial y'} - \frac{\partial \tilde{H}_y}{\partial z'} &= \epsilon_{xx} \vec{E}_x \\ \frac{\partial \tilde{H}_x}{\partial z'} - \frac{\partial \tilde{H}_z}{\partial x'} &= \epsilon_{yy} \vec{E}_y \\ \frac{\partial \tilde{H}_y}{\partial x'} - \frac{\partial \tilde{H}_x}{\partial y'} &= \epsilon_{zz} \vec{E}_z \end{aligned} \quad (1.3.18)$$

Next the finite-difference approximations need to be applied to the normalized curl equations in Eqs. (1.3.17) and (1.3.18). In this approximation, a 3D grid made up of  $i$  by  $j$  by  $k$  elements is assumed.

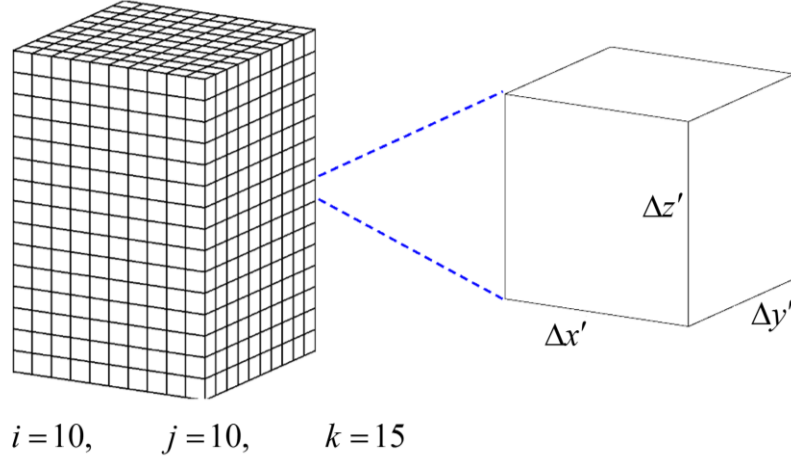


Figure 2.4: 3D simulation space example. [36]

The finite-difference approximation is then staggered to account for the staggered fields of the Yee grid shown in Figure 2.2. This leads to the following equations:

$$\begin{aligned}
 \frac{E_z^{i,j+1,k} - E_z^{i,j,k}}{\Delta y'} - \frac{E_y^{i,j,k+1} - E_y^{i,j,k}}{\Delta z'} &= \mu_{xx}^{i,j,k} \tilde{H}_x^{i,j,k} \\
 \frac{E_x^{i,j,k+1} - E_x^{i,j,k}}{\Delta z'} - \frac{E_z^{i+1,j,k} - E_z^{i,j,k}}{\Delta x'} &= \mu_{yy}^{i,j,k} \tilde{H}_y^{i,j,k} \\
 \frac{E_y^{i+1,j,k} - E_y^{i,j,k}}{\Delta x'} - \frac{E_x^{i,j+1,k} - E_x^{i,j,k}}{\Delta y'} &= \mu_{zz}^{i,j,k} \tilde{H}_z^{i,j,k}
 \end{aligned} \tag{1.3.19}$$

$$\begin{aligned}
 \frac{\tilde{H}_z^{i,j,k} - \tilde{H}_z^{i,j-1,k}}{\Delta y'} - \frac{\tilde{H}_y^{i,j,k} - \tilde{H}_y^{i,j,k-1}}{\Delta z'} &= \epsilon_{xx}^{i,j,k} E_x^{i,j,k} \\
 \frac{\tilde{H}_x^{i,j,k} - \tilde{H}_x^{i,j,k-1}}{\Delta z'} - \frac{\tilde{H}_z^{i,j,k} - \tilde{H}_z^{i-1,j,k}}{\Delta x'} &= \epsilon_{yy}^{i,j,k} E_y^{i,j,k} \\
 \frac{\tilde{H}_y^{i,j,k} - \tilde{H}_y^{i-1,j,k}}{\Delta x'} - \frac{\tilde{H}_x^{i,j,k} - \tilde{H}_x^{i,j-1,k}}{\Delta y'} &= \epsilon_{zz}^{i,j,k} E_z^{i,j,k}
 \end{aligned} \tag{1.3.20}$$

At this point Eqs. (1.3.19) and (1.3.20) are assumed to be two dimensional. This assumption states  $\partial/\partial z = 0$ , meaning that the simulation space is uniform and there is no propagation in the  $z$  direction. Applying this assumption, it can be seen that Maxwell's equations split into two distinct sets of three coupled equations.

$$\begin{aligned} \frac{E_y^{i+1,j} - E_y^{i,j}}{\Delta x'} - \frac{E_x^{i,j+1} - E_x^{i,j}}{\Delta y'} &= \mu_{zz}^{i,j} \tilde{H}_z^{i,j} \\ \frac{\tilde{H}_z^{i,j} - \tilde{H}_z^{i,j-1}}{\Delta y'} &= \varepsilon_{xx}^{i,j} E_x^{i,j} \end{aligned} \quad (1.3.21)$$

$$\begin{aligned} -\frac{\tilde{H}_z^{i,j} - \tilde{H}_z^{i-1,j}}{\Delta x'} &= \varepsilon_{yy}^{i,j} E_y^{i,j} \\ \frac{\tilde{H}_y^{i,j} - \tilde{H}_y^{i-1,j}}{\Delta x'} - \frac{\tilde{H}_x^{i,j} - \tilde{H}_x^{i,j-1}}{\Delta y'} &= \varepsilon_{zz}^{i,j} E_z^{i,j} \\ \frac{E_z^{i,j+1} - E_z^{i,j}}{\Delta y'} &= \mu_{xx}^{i,j} \tilde{H}_x^{i,j} \\ -\frac{E_z^{i+1,j} - E_z^{i,j}}{\Delta x'} &= \mu_{yy}^{i,j} \tilde{H}_y^{i,j} \end{aligned} \quad (1.3.22)$$

From here it can also be seen that these equations need be written for each block of simulation space and solved simultaneously. It can also be inferred from Eqs. (1.3.21) and (1.3.22) that the operations contained within are completely linear operations.

This leads to the conclusion that these equations can be completely rewritten in block matrix form and derivative operators created that perform the above calculations for every point on the grid. These derivative operators are created by generalizing the equations above into the following block matrix form. Below are examples of the derivative operators for a simple 2 by 2 grid.

$$\begin{aligned} \left. \frac{\partial E}{\partial x'} \right|_{i+\frac{1}{2}} &\cong \frac{E_{i+1} - E_i}{\Delta x'} \\ &\downarrow \\ \mathbf{D}_x^E \mathbf{E} &= \frac{1}{\Delta x'} \begin{bmatrix} -1 & 1 & 0 & 0 \\ 0 & -1 & 1 & 0 \\ 0 & 0 & -1 & 1 \\ 0 & 0 & 0 & -1 \end{bmatrix} \begin{bmatrix} E_1 \\ E_2 \\ E_3 \\ E_4 \end{bmatrix} = \begin{bmatrix} \frac{\partial}{\partial x'} E_{1.5} \\ \frac{\partial}{\partial x'} E_{2.5} \\ \frac{\partial}{\partial x'} E_{3.5} \\ \frac{\partial}{\partial x'} E_{4.5} \end{bmatrix} \end{aligned} \quad (1.3.23)$$

$$\begin{aligned}
& \left. \frac{\partial E}{\partial y'} \right|_{j+\frac{1}{2}} \cong \frac{E_{j+1} - E_j}{\Delta y'} \\
& \quad \downarrow \\
\mathbf{D}_y^E \mathbf{E} &= \frac{1}{\Delta y'} \begin{bmatrix} -1 & 0 & 1 & 0 \\ 0 & -1 & 0 & 1 \\ 0 & 0 & -1 & 0 \\ 0 & 0 & 0 & -1 \end{bmatrix} \begin{bmatrix} E_1 \\ E_2 \\ E_3 \\ E_4 \end{bmatrix} = \begin{bmatrix} \frac{\partial}{\partial y'} E_{1.5} \\ \frac{\partial}{\partial y'} E_{2.5} \\ \frac{\partial}{\partial y'} E_{3.5} \\ \frac{\partial}{\partial y'} E_{4.5} \end{bmatrix} \tag{1.3.24}
\end{aligned}$$

It is useful to note that the derivative operators for the  $\tilde{H}$  field are the negative complex Hermitian of the derivative operators for the  $\vec{E}$  field. This information can be used to reduce the amount of calculation needed to build these derivative operators.

$$\begin{aligned}
& \left. \frac{\partial \tilde{H}}{\partial x'} \right|_{i-\frac{1}{2}} \cong \frac{\tilde{H}_i - \tilde{H}_{i-1}}{\Delta x'} \\
& \quad \downarrow \\
\mathbf{D}_x^H \tilde{\mathbf{H}} &= \frac{1}{\Delta x'} \begin{bmatrix} 1 & 0 & 0 & 0 \\ -1 & 1 & 0 & 0 \\ 0 & -1 & 1 & 0 \\ 0 & 0 & -1 & 1 \end{bmatrix} \begin{bmatrix} \tilde{H}_1 \\ \tilde{H}_2 \\ \tilde{H}_3 \\ \tilde{H}_4 \end{bmatrix} = \begin{bmatrix} \frac{\partial}{\partial x'} \tilde{H}_{0.5} \\ \frac{\partial}{\partial x'} \tilde{H}_{1.5} \\ \frac{\partial}{\partial x'} \tilde{H}_{2.5} \\ \frac{\partial}{\partial x'} \tilde{H}_{3.5} \end{bmatrix} \tag{1.3.25}
\end{aligned}$$

$$\begin{aligned}
& \left. \frac{\partial \tilde{H}}{\partial y'} \right|_{j-\frac{1}{2}} \cong \frac{\tilde{H}_j - \tilde{H}_{j-1}}{\Delta y'} \\
& \quad \downarrow \\
& \mathbf{D}_y^H \tilde{\mathbf{H}} = \frac{1}{\Delta y'} \begin{bmatrix} -1 & 0 & 0 & 0 \\ 0 & -1 & 0 & 0 \\ 1 & 0 & -1 & 0 \\ 0 & 1 & 0 & -1 \end{bmatrix} \begin{bmatrix} \tilde{H}_1 \\ \tilde{H}_2 \\ \tilde{H}_3 \\ \tilde{H}_4 \end{bmatrix} = \begin{bmatrix} \frac{\partial}{\partial y'} \tilde{H}_{0.5} \\ \frac{\partial}{\partial y'} \tilde{H}_{1.5} \\ \frac{\partial}{\partial y'} \tilde{H}_{2.5} \\ \frac{\partial}{\partial y'} \tilde{H}_{3.5} \end{bmatrix} \quad (1.3.26)
\end{aligned}$$

At this point the derivative operators are almost complete. Two more steps are needed to make them work appropriately. First numerical boundary conditions need to be implemented. To incorporate a periodic boundary condition, a Dirichlet boundary [39] is incorporated first. In the formulation of the derivative operators, this is simply a 0 at the grid boundary point.

Next the phase tilt as described from the Bloch-Floquet theorem [40] needs to be accounted for. The Bloch-Floquet theorem states that “waves in periodic structures take on the same periodicity and symmetry as the structure itself” [36]. Since we are implementing periodic boundary conditions we need to obey the Bloch-Floquet theorem. Below is the Bloch-Floquet theorem.

$$\vec{E}(\vec{r}) = \vec{A}_{\vec{\beta}}(\vec{r}) e^{j\vec{\beta} \cdot \vec{r}} \quad (1.3.27)$$

In this equation,  $\vec{E}(\vec{r})$  is the vector electric field,  $\vec{A}_{\vec{\beta}}(\vec{r})$  is the vector periodic envelope, and  $e^{j\vec{\beta} \cdot \vec{r}}$  is the plane wave phase term that has to be corrected for. To account for this “phase tilt” the plane wave phase term is incorporated into the derivative operator. In this formulation of the FDFD method the “phase tilt” term takes the following form where  $\Lambda_x$  the period length.

$$e^{j\vec{\beta} \cdot \vec{r}} \rightarrow e^{j\beta \Lambda_x} \quad (1.3.28)$$

This term is inserted into the derivative operator where ever a numerical boundary occurs. Below is shown the corrected derivative operators with the periodic boundary condition changes in red.

$$\mathbf{D}_x^E \mathbf{E} = \frac{1}{\Delta x'} \begin{bmatrix} -1 & 1 & 0 & 0 \\ e^{j\beta\Lambda_x} & -1 & \mathbf{0} & 0 \\ 0 & 0 & -1 & 1 \\ 0 & 0 & e^{j\beta\Lambda_x} & -1 \end{bmatrix} \begin{bmatrix} E_1 \\ E_2 \\ E_3 \\ E_4 \end{bmatrix} \quad (1.3.29)$$

$$\mathbf{D}_y^E \mathbf{E} = \frac{1}{\Delta y'} \begin{bmatrix} -1 & 0 & 1 & 0 \\ 0 & -1 & 0 & 1 \\ e^{j\beta\Lambda_x} & 0 & -1 & 0 \\ 0 & e^{j\beta\Lambda_x} & 0 & -1 \end{bmatrix} \begin{bmatrix} E_1 \\ E_2 \\ E_3 \\ E_4 \end{bmatrix} \quad (1.3.30)$$

$$\mathbf{D}_x^H \tilde{\mathbf{H}} = \frac{1}{\Delta x'} \begin{bmatrix} 1 & e^{j\beta\Lambda_x} & 0 & 0 \\ -1 & 1 & 0 & 0 \\ 0 & \mathbf{0} & 1 & e^{j\beta\Lambda_x} \\ 0 & 0 & -1 & 1 \end{bmatrix} \begin{bmatrix} \tilde{H}_1 \\ \tilde{H}_2 \\ \tilde{H}_3 \\ \tilde{H}_4 \end{bmatrix} \quad (1.3.31)$$

$$\mathbf{D}_y^H \tilde{\mathbf{H}} = \frac{1}{\Delta y'} \begin{bmatrix} -1 & 0 & e^{j\beta\Lambda_x} & 0 \\ 0 & -1 & 0 & e^{j\beta\Lambda_x} \\ 1 & 0 & -1 & 0 \\ 0 & 1 & 0 & -1 \end{bmatrix} \begin{bmatrix} \tilde{H}_1 \\ \tilde{H}_2 \\ \tilde{H}_3 \\ \tilde{H}_4 \end{bmatrix} \quad (1.3.32)$$

Larger example derivative operators can be viewed in Appendix A2. Once the derivative operators are completed, the right hand of the curl equations can be put into block matrix form. This is a simple point by point multiplication of the materials put in a diagonal matrix.

$$\boldsymbol{\varepsilon}_r \mathbf{E}_i = \begin{bmatrix} \varepsilon_1 & 0 & 0 \\ 0 & \ddots & 0 \\ 0 & 0 & \varepsilon_r \end{bmatrix} \begin{bmatrix} E_1 \\ \vdots \\ E_i \end{bmatrix} \quad (1.3.33)$$

$$\boldsymbol{\mu}_r \tilde{\mathbf{H}}_i = \begin{bmatrix} \mu_1 & 0 & 0 \\ 0 & \ddots & 0 \\ 0 & 0 & \mu_r \end{bmatrix} \begin{bmatrix} \tilde{H}_1 \\ \vdots \\ \tilde{H}_i \end{bmatrix} \quad (1.3.34)$$

Combining all this together and implementing it with Eqs. (1.3.21) and (1.3.22) yields the 2D Maxwell's curl equations in block matrix form.

$\mathbf{E}_z$  Mode:

$$\mathbf{D}_x^H \tilde{\mathbf{H}}_y - \mathbf{D}_y^H \tilde{\mathbf{H}}_x = \boldsymbol{\varepsilon}_{zz} \mathbf{E}_z \quad (1.3.35)$$

$$\mathbf{D}_y^E \mathbf{E}_z = \boldsymbol{\mu}_{xx} \tilde{\mathbf{H}}_x \quad (1.3.36)$$

$$-\mathbf{D}_x^E \mathbf{E}_z = \boldsymbol{\mu}_{yy} \tilde{\mathbf{H}}_y \quad (1.3.37)$$

$\mathbf{H}_z$  Mode:

$$\mathbf{D}_x^E \mathbf{E}_y - \mathbf{D}_y^E \mathbf{E}_x = \boldsymbol{\mu}_{zz} \tilde{\mathbf{H}}_z \quad (1.3.38)$$

$$\mathbf{D}_y^H \tilde{\mathbf{H}}_z = \boldsymbol{\varepsilon}_{xx} \mathbf{E}_x \quad (1.3.39)$$

$$-\mathbf{D}_x^H \tilde{\mathbf{H}}_z = \boldsymbol{\varepsilon}_{yy} \mathbf{E}_y \quad (1.3.40)$$

From here the Helmholtz wave equations, [41] and [42], are derived. To derive this equation for the  $\mathbf{E}_z$  mode, one must first solve for the  $\tilde{\mathbf{H}}_x$  and  $\tilde{\mathbf{H}}_y$  term in Eqs. (1.3.36) and (1.3.37). These values are then substituted back into Eq. (1.3.35). This derivation applies to the  $\tilde{\mathbf{H}}_z$  mode as well, except one must solve for the  $\mathbf{E}_x$  and  $\mathbf{E}_y$  terms in Eqs. (1.3.39) and (1.3.40). These terms are then substituted back into Eq. (1.3.38). After doing the arithmetic shown in Appendix A3, the final wave equations are derived.

$\mathbf{E}_z$  Mode

$$\begin{aligned} \mathbf{A}_E \mathbf{E}_z &= 0 \\ \mathbf{A}_E &= \mathbf{D}_x^H \boldsymbol{\mu}_{yy}^{-1} \mathbf{D}_x^E + \mathbf{D}_y^H \boldsymbol{\mu}_{xx}^{-1} \mathbf{D}_y^E + \boldsymbol{\varepsilon}_{zz} \end{aligned} \quad (1.3.41)$$

$\mathbf{H}_z$  Mode

$$\mathbf{A}_H \tilde{\mathbf{H}}_z = 0 \quad (1.3.42)$$

$$\mathbf{A}_H = \mathbf{D}_x^E \boldsymbol{\epsilon}_{yy}^{-1} \mathbf{D}_x^H + \mathbf{D}_y^E \boldsymbol{\epsilon}_{xx}^{-1} \mathbf{D}_y^H + \boldsymbol{\mu}_{zz}$$

With the wave equations derived, absorbing boundary layers need to be added to the simulation space. Without these boundaries the source would just bounce around indefinitely and cause errors within the simulation. The most common absorbing boundaries used in the FDFD and FDTD methods are the uniaxial perfectly matched layer (PML) boundary [38]. The PML absorbing boundary works by perfectly matching the impedance of an incidence wave at any angle, and by introducing a significant amount of loss within its area of influence. The perfectly matched impedance reduces reflection of a wave entering the PML region while the large amount of loss totally absorbs all its energy. The loss is introduced using an exponential term starting with no loss to maximum loss. This helps also with the minimization of reflections. These regions are built into the simulation space, so they are absorbed into the material tensors. Maxwell's curl equations with the PML tensors added are shown below.

$$\begin{aligned} \nabla \times \vec{E} &= k_0 \left( [\mu_r] [\bar{\bar{s}}] \right) \tilde{H} \\ \nabla \times \tilde{H} &= k_0 \left( [\epsilon_r] [\bar{\bar{s}}] \right) \vec{E} \end{aligned} \quad (1.3.43)$$

The PML must be implemented in a tensor form to correctly match the impedance at any angle of incidence. This tensor takes on the following form.

$$[\bar{\bar{s}}] = \begin{bmatrix} \frac{s_y s_z}{s_x} & 0 & 0 \\ 0 & \frac{s_x s_z}{s_y} & 0 \\ 0 & 0 & \frac{s_x s_y}{s_z} \end{bmatrix} \quad (1.3.44)$$

Where

$$\begin{aligned}
s_x(x) &= \left(1 + a_{\max} \left(\frac{x}{L_x}\right)^p\right) \left(1 + \frac{\eta_0}{jk_0} \sigma_{\max} \sin^2\left(\frac{\pi x}{2L_x}\right)\right) \\
s_y(y) &= \left(1 + a_{\max} \left(\frac{y}{L_y}\right)^p\right) \left(1 + \frac{\eta_0}{jk_0} \sigma_{\max} \sin^2\left(\frac{\pi y}{2L_y}\right)\right) \\
s_z(z) &= \left(1 + a_{\max} \left(\frac{z}{L_z}\right)^p\right) \left(1 + \frac{\eta_0}{jk_0} \sigma_{\max} \sin^2\left(\frac{\pi z}{2L_z}\right)\right)
\end{aligned} \tag{1.3.45}$$

$$\begin{aligned}
0 &\leq a_{\max} \leq 5 \\
3 &\leq p \leq 5 \\
\sigma_{\max} &\approx 1
\end{aligned}$$

The abruptness at which the loss is implemented into the PML can be adjusted with the  $a_{\max}$  and  $p$  terms. The  $\sigma_{\max}$  adjusts the amount of loss while the  $L_x$ ,  $L_y$  and  $L_z$  terms are the number of grid cells wide the PML region is. With the PML regions implemented a source is now ready to be derived.

As they are at this moment, the solution to Eqs. (1.3.41) and (1.3.42) are trivial as there is no excitation added. A source must be implemented. A source term  $\mathbf{f}$  is implemented in through the right side of Eqs. (1.3.41) and (1.3.42).

$$\begin{aligned}
\mathbf{A}_E \mathbf{E}_z &= \mathbf{f} \\
\mathbf{A}_H \tilde{\mathbf{H}}_z &= \mathbf{f}
\end{aligned} \tag{1.3.46}$$

In this formulation of the FDFD method the source takes on the form of electromagnetic plane wave. An electromagnetic plane wave can be numerically described through the following equation.

$$E_{\text{src}}(\vec{r}) = e^{-j\vec{k}_{\text{inc}} \cdot \vec{r}} \tag{1.3.47}$$

This plane wave source term is implemented into the simulation through the total-field/scatter-field (TF/SF) source method [38]. In this method the total-field shows all the interface of scattered and source waves, while the scatter-field only shows the scattered waves. In Ref. [43], the author

showed that this TF/SF field interface could be easily and arbitrarily controlled using a  $\mathbf{Q}$  masking matrix. This masking matrix allows one to put the TF/SF interfaces anywhere in the grid. The  $\mathbf{Q}$  masking matrix is just a matrix the size of the simulation space that is made up of 1s and 0s. A zero signifies a total-field quantity, while a one signifies a scatter-field quantity.

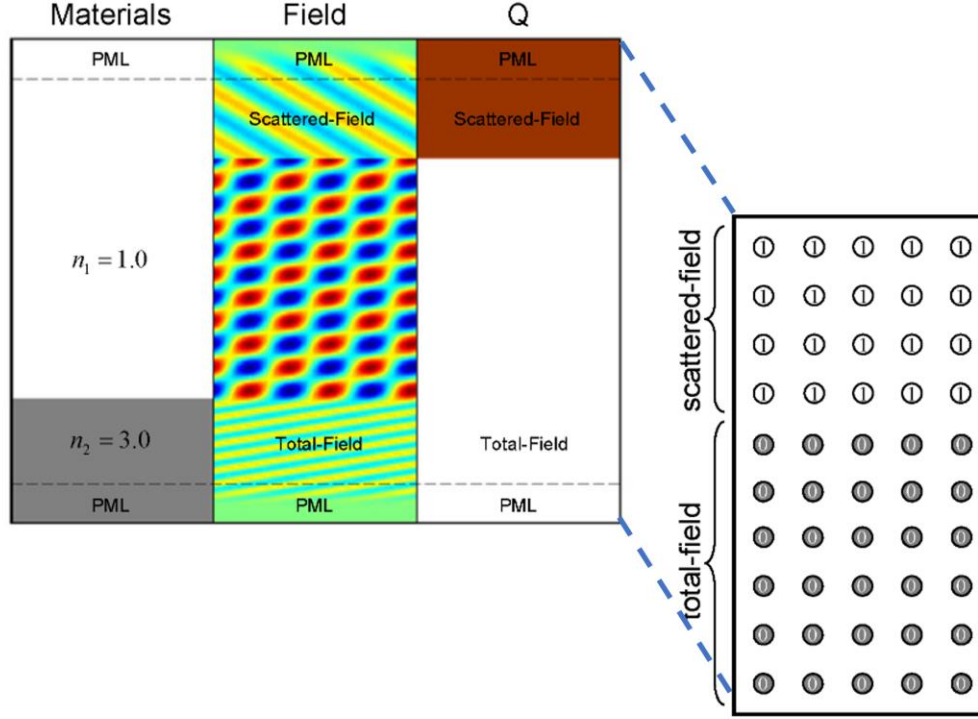


Figure 2.5: Illustration of a FDFD simulation space showing the PMLs, TF/SF interfaces and an example  $\mathbf{Q}$  masking matrix [36].

To implement the TF/SF source method, the Eq. (1.3.47) is generalized to work with the linear algebra operators that were derived earlier.

$$\mathbf{f}_{\text{src}} = e^{-j(k_x \mathbf{x} + k_y \mathbf{y})} = \begin{bmatrix} f_{1,1} \\ \vdots \\ f_{N_x, N_y} \end{bmatrix} \quad (1.3.48)$$

In Eq. (1.3.48),  $N_x$  and  $N_y$  are the number of grid cells the simulation space occupies. This equation is then implemented through the masking equation.

$$\begin{aligned}\mathbf{f}_E &= (\mathbf{Q}\mathbf{A}_E - \mathbf{A}_E\mathbf{Q})\mathbf{f}_{\text{src}} \\ \mathbf{f}_H &= (\mathbf{Q}\mathbf{A}_H - \mathbf{A}_H\mathbf{Q})\mathbf{f}_{\text{src}}\end{aligned}\tag{1.3.49}$$

These equations are then substituted into the equations in Eq. (1.3.46).

$$\begin{aligned}\mathbf{A}_E\mathbf{E}_z &= \mathbf{f}_E \\ \mathbf{A}_H\tilde{\mathbf{H}}_z &= \mathbf{f}_H\end{aligned}\tag{1.3.50}$$

From here it can be seen that the fields  $\mathbf{E}_z$  and  $\tilde{\mathbf{H}}_z$  can be solved for by backwards dividing the derivative operator equation,  $\mathbf{A}_E$  and  $\mathbf{A}_H$ , with the derived source matrices,  $\mathbf{f}_E$  and  $\mathbf{f}_H$ . These solved fields are the end of the FDFD method itself.

After the fields have been calculated, all that remains is the post processing of the calculated fields for the data required. For most cases, and in the case of simulating these all-dielectric FSSs, the data that needs to be extracted is the overall transmittance and reflectance of the device. This is accomplished through the summation of all the generated spatial harmonic diffraction efficiencies of the record planes of the device [25]. The record planes are a slice of the calculated fields, usually one cell thick that is taken before the PML layers. The diffraction efficiency calculation starts with removing the phase tilt term that was added from the derivative operators.

$$\begin{aligned}E'_{\text{ref}}(x) &= E_{\text{ref}}(x)e^{-j\beta\Lambda_x} \\ E'_{\text{tm}}(x) &= E_{\text{tm}}(x)e^{-j\beta\Lambda_x}\end{aligned}\tag{1.3.51}$$

Next, a fast Fourier transform (FFT) is applied to the field values.

$$\begin{aligned}S_{\text{ref}}(n) &= \text{FFT}\{E'_{\text{ref}}(h)\} \\ S_{\text{tm}}(n) &= \text{FFT}\{E'_{\text{tm}}(h)\}\end{aligned}\tag{1.3.52}$$

This outputs all the complex amplitudes of all the spatial harmonics contained within the record plane. The individual harmonic number is denoted as  $m$ . The wave vector components  $k$  of the spatial harmonics are then calculated. First the,  $x$  component of the wave vector is calculated. In Eq. (1.3.53)  $\epsilon_{\text{inc}}$  and  $\mu_{\text{inc}}$  are material properties that the incident wave is in, and  $\theta$  is the angle of incidence.

$$k_{x,n} = k_0 \sqrt{\epsilon_{\text{inc}} \mu_{\text{inc}}} \sin \theta - \frac{2\pi m}{\Lambda} \quad (1.3.53)$$

$$m = -\frac{N_x}{2}, \dots, -2, -1, 0, 1, 2, \dots, \frac{N_x}{2}$$

Next the  $y$  component needs to be calculated. Two  $y$  components are needed, one for the reflection side and one for the transmitted.

$$k_{y,n}^{\text{ref}} = \begin{cases} \sqrt{k_0^2 \epsilon_{\text{ref}} \mu_{\text{ref}} - k_{x,n}^2} & k_0 \sqrt{\epsilon_{\text{ref}} \mu_{\text{ref}}} \geq k_{x,n} \\ -j \sqrt{k_{x,n}^2 - k_0^2 \epsilon_{\text{ref}} \mu_{\text{ref}}} & k_0 \sqrt{\epsilon_{\text{ref}} \mu_{\text{ref}}} < k_{x,n} \end{cases} \quad (1.3.54)$$

$$k_{y,n}^{\text{trn}} = \begin{cases} \sqrt{k_0^2 \epsilon_{\text{trn}} \mu_{\text{trn}} - k_{x,n}^2} & k_0 \sqrt{\epsilon_{\text{trn}} \mu_{\text{trn}}} \geq k_{x,n} \\ -j \sqrt{k_{x,n}^2 - k_0^2 \epsilon_{\text{trn}} \mu_{\text{trn}}} & k_0 \sqrt{\epsilon_{\text{trn}} \mu_{\text{trn}}} < k_{x,n} \end{cases} \quad (1.3.55)$$

In Eqs. (1.3.54) and (1.3.55),  $\epsilon_{\text{ref}}$ ,  $\mu_{\text{ref}}$ ,  $\epsilon_{\text{trn}}$ , and  $\mu_{\text{trn}}$  are the material properties of the material that is in each specific spatial harmonic. These derived terms are then substituted in the transmittance and reflectance power equations and summed [25].

$$REF = \sum_{n=1}^{N_x} \left\{ |S_{\text{ref}}(n)|^2 \cdot \text{Re} \left[ \frac{k_{y,n}^{\text{ref}}}{k_0 \sqrt{\epsilon_{\text{inc}} \mu_{\text{inc}}} \cos \theta} \right] \right\} \quad (1.3.56)$$

$$TRN = \sum_{n=1}^{N_x} \left\{ |S_{\text{trn}}(n)|^2 \cdot \text{Re} \left[ \frac{k_{y,n}^{\text{trn}}}{k_0 \sqrt{\epsilon_{\text{inc}} \mu_{\text{inc}}} \cos \theta} \right] \right\} \quad (1.3.57)$$

To check for convergence and to see if the model is working correctly, the  $REF$  and  $TRN$  values can be summed and checked to see if they equal one. This is due to the conservation of energy law. This check only works for lossless materials.

$$CON = REF + TRN \quad (1.3.58)$$

The FDFD numerical method is very powerful tool for analyzing all-dielectric FSSs. It provides a fully rigorous numerical solution to Maxwell's equation. Though powerful, it does have its drawbacks. One of the major drawbacks of this method is its use and implementation of the finite-difference approximation. Because of this approximation, this method is only as accurate as the smallest grid resolution allowed. The smaller grid resolution is, the finer the detail it can accurately simulate.

Practical experience has shown that 20 steps per wavelength in the highest permittivity material being simulated is a good point to start at when checking for convergence.

Another major drawback to this method is in its massive computational requirements. Being that this method uses linear algebra, data operations and storage can become very large. This limits its use to two dimensions or very small three dimensional grids. This problem is especially troublesome when simulating devices with very fine details as the grid resolution needed for convergence is very small; leading to massive matrices. The largest computation used for this method is a backwards matrix division. This can be a very slow operation to calculate, especially with large matrices. This method also has problems handling curved surfaces. Step approximations need to be taken to simulate a curved surface. When it comes to 3D simulations other methods shine, especially one in particular for 3D all-dielectric devices.

## **2.2 Method of Lines**

Method of lines (MOL) is a fully 3D semi-analytical modeling technique used to simulate the electromagnetic interaction and response of different materials and complex devices in the frequency domain [44],[45]. MOL provides a fully rigorous solution to Maxwell's equations and is very good for simulating multilayer periodic devices with metal and high dielectric contrasts. In this method, two out of the three independent variables in Maxwell's equation are discretized, while one is solved analytically. In this formulation, the variables  $x$  and  $y$  will be handled numerically with the finite-difference method, and the wave propagation in the  $z$  direction will be handled analytically. Discretizing the  $x$  and  $y$  variables allows the PDEs of Maxwell's equations

to be transformed into a set of common ordinary differential equations (ODEs). The solution of this ODE takes on the form of a common eigenvalue problem. The eigenvalues and eigenvectors calculated describe all the propagating modes of the device.

Through basic EM theory it is known that when a propagating mode encounters a boundary, i.e. different materials or geometries that the power in the modes shuffles. This shuffling of powers can create new dominant propagating modes. In a uniform medium, the modes only accumulates phase. In MOL, this phase accumulation is analytically solved. The device being simulated is quantized in the  $z$  direction. This creates layers that the phase can be analytically applied through. The modes are solved at each boundary layer, propagated and then connected to each other through scattering matrices to calculate the overall response of the device. This can be seen in Figure 2.6.

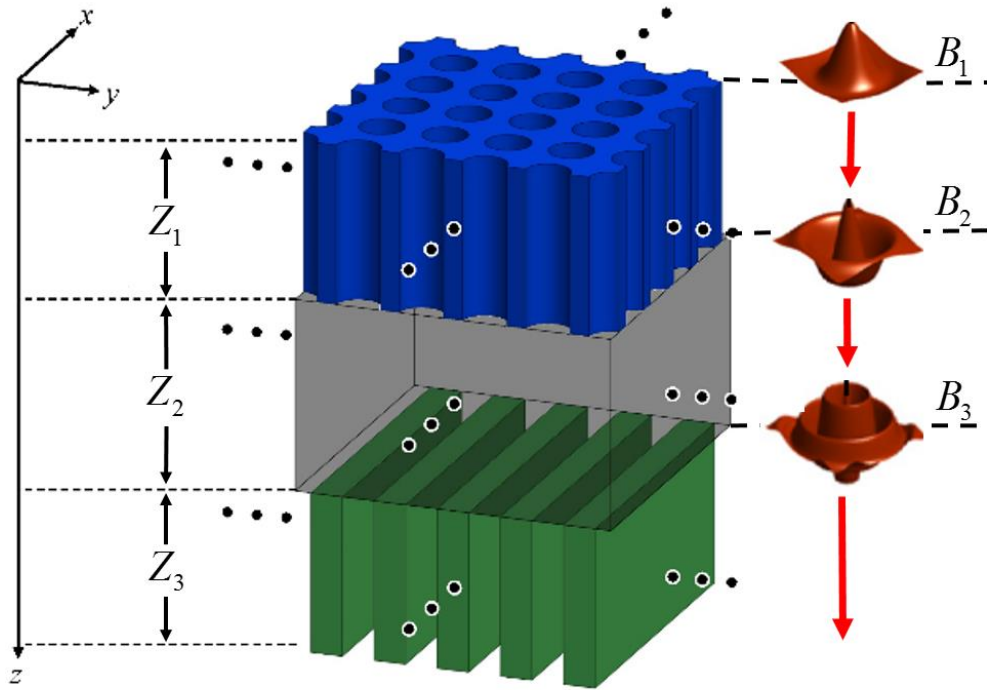


Figure 2.6: Illustration of a multilayer device. This diagram shows the mode shuffling and propagation at boundaries through the device.[36]

The formulation for the MOL starts the same as the FDFD method outlined in Section 2.1. Maxwell's equations are normalized and expanded. Eqs. (1.3.17) and (1.3.18) are then put into block matrix form except for the  $z$  partial derivative. The derivative operators used in this method are the same ones as used in the FDFD method. Their formulation is outlined from Eq. (1.3.23) to Eq. (1.3.32)

At this point the partial derivative of  $z$  becomes a regular derivative because it is the only variable left.

$$\mathbf{D}_y^E \mathbf{E}_z - \frac{d}{dz'} \mathbf{E}_y = \boldsymbol{\mu}_{xx} \tilde{\mathbf{H}}_x \quad (1.4.1)$$

$$\frac{d}{dz'} \mathbf{E}_x - \mathbf{D}_x^E \mathbf{E}_z = \boldsymbol{\mu}_{yy} \tilde{\mathbf{H}}_y \quad (1.4.2)$$

$$\mathbf{D}_x^E \mathbf{E}_y - \mathbf{D}_y^E \mathbf{E}_x = \boldsymbol{\mu}_{zz} \tilde{\mathbf{H}}_z \quad (1.4.3)$$

$$\mathbf{D}_y^H \tilde{\mathbf{H}}_z - \frac{d}{dz'} \tilde{\mathbf{H}}_y = \boldsymbol{\epsilon}_{xx} \mathbf{E}_x \quad (1.4.4)$$

$$\frac{d}{dz'} \tilde{\mathbf{H}}_x - \mathbf{D}_x^H \tilde{\mathbf{H}}_z = \boldsymbol{\epsilon}_{yy} \mathbf{E}_y \quad (1.4.5)$$

$$\mathbf{D}_x^H \tilde{\mathbf{H}}_y - \mathbf{D}_y^H \tilde{\mathbf{H}}_x = \boldsymbol{\epsilon}_{zz} \mathbf{E}_z \quad (1.4.6)$$

Next, Eqs. (1.4.3) and (1.4.6) are solved  $\mathbf{E}_z$  and  $\tilde{\mathbf{H}}_z$ . This eliminates the longitudinal components of the fields.

$$\tilde{\mathbf{H}}_z = \boldsymbol{\mu}_{zz}^{-1} (\mathbf{D}_x^E \mathbf{E}_y - \mathbf{D}_y^E \mathbf{E}_x) \quad (1.4.7)$$

$$\mathbf{E}_z = \boldsymbol{\epsilon}_{zz}^{-1} (\mathbf{D}_x^H \tilde{\mathbf{H}}_y - \mathbf{D}_y^H \tilde{\mathbf{H}}_x) \quad (1.4.8)$$

Eq. (1.4.7) is substituted into Eqs. (1.4.4) and (1.4.5) while Eq. (1.4.8) is substituted into Eqs. (1.4.1) and (1.4.2). Once this is complete, the  $\frac{d}{dz}$  term is solved for. This derivation can be viewed in Appendix A4.

$$\frac{d}{dz'} \mathbf{E}_x = -\mathbf{D}_x^E \boldsymbol{\epsilon}_{zz}^{-1} \mathbf{D}_y^H \tilde{\mathbf{H}}_x + (\boldsymbol{\mu}_{yy} + \mathbf{D}_x^E \boldsymbol{\epsilon}_{zz}^{-1} \mathbf{D}_x^H) \tilde{\mathbf{H}}_y \quad (1.4.9)$$

$$\frac{d}{dz'} \mathbf{E}_y = -(\boldsymbol{\mu}_{xx} + \mathbf{D}_y^E \boldsymbol{\epsilon}_{zz}^{-1} \mathbf{D}_y^H) \tilde{\mathbf{H}}_x + \mathbf{D}_y^E \boldsymbol{\epsilon}_{zz}^{-1} \mathbf{D}_x^H \tilde{\mathbf{H}}_y \quad (1.4.10)$$

$$\frac{d}{dz'} \tilde{\mathbf{H}}_x = -\mathbf{D}_x^H \boldsymbol{\mu}_{zz}^{-1} \mathbf{D}_y^E \mathbf{E}_x + (\boldsymbol{\epsilon}_{yy} + \mathbf{D}_x^H \boldsymbol{\mu}_{zz}^{-1} \mathbf{D}_x^E) \mathbf{E}_y \quad (1.4.11)$$

$$\frac{d}{dz'} \tilde{\mathbf{H}}_y = -(\boldsymbol{\epsilon}_{xx} + \mathbf{D}_y^H \boldsymbol{\mu}_{zz}^{-1} \mathbf{D}_y^E) \mathbf{E}_x + \mathbf{D}_y^H \boldsymbol{\mu}_{zz}^{-1} \mathbf{D}_x^E \mathbf{E}_y \quad (1.4.12)$$

These equations can now be put into block matrix form.

$$\frac{d}{dz'} \begin{bmatrix} \mathbf{E}_x \\ \mathbf{E}_y \end{bmatrix} = \begin{bmatrix} -\mathbf{D}_x^E \boldsymbol{\epsilon}_{zz}^{-1} \mathbf{D}_y^H & (\boldsymbol{\mu}_{yy} + \mathbf{D}_x^E \boldsymbol{\epsilon}_{zz}^{-1} \mathbf{D}_x^H) \\ -(\boldsymbol{\mu}_{xx} + \mathbf{D}_y^E \boldsymbol{\epsilon}_{zz}^{-1} \mathbf{D}_y^H) & \mathbf{D}_y^E \boldsymbol{\epsilon}_{zz}^{-1} \mathbf{D}_x^H \end{bmatrix} \begin{bmatrix} \tilde{\mathbf{H}}_x \\ \tilde{\mathbf{H}}_y \end{bmatrix} \quad (1.4.13)$$

$$\frac{d}{dz'} \begin{bmatrix} \tilde{\mathbf{H}}_x \\ \tilde{\mathbf{H}}_y \end{bmatrix} = \begin{bmatrix} -\mathbf{D}_x^H \boldsymbol{\mu}_{zz}^{-1} \mathbf{D}_y^E & (\boldsymbol{\epsilon}_{yy} + \mathbf{D}_x^H \boldsymbol{\mu}_{zz}^{-1} \mathbf{D}_x^E) \\ -(\boldsymbol{\epsilon}_{xx} + \mathbf{D}_y^H \boldsymbol{\mu}_{zz}^{-1} \mathbf{D}_y^E) & \mathbf{D}_y^H \boldsymbol{\mu}_{zz}^{-1} \mathbf{D}_x^E \end{bmatrix} \begin{bmatrix} \mathbf{E}_x \\ \mathbf{E}_y \end{bmatrix} \quad (1.4.14)$$

Eqs. (1.4.13) and (1.4.14) are then written in the standard  $\mathbf{P}$  and  $\mathbf{Q}$  form.

$$\frac{d}{dz'} \begin{bmatrix} \mathbf{E}_x \\ \mathbf{E}_y \end{bmatrix} = \mathbf{P} \begin{bmatrix} \tilde{\mathbf{H}}_x \\ \tilde{\mathbf{H}}_y \end{bmatrix} \quad \mathbf{P} = \begin{bmatrix} -\mathbf{D}_x^E \boldsymbol{\epsilon}_{zz}^{-1} \mathbf{D}_y^H & (\boldsymbol{\mu}_{yy} + \mathbf{D}_x^E \boldsymbol{\epsilon}_{zz}^{-1} \mathbf{D}_x^H) \\ -(\boldsymbol{\mu}_{xx} + \mathbf{D}_y^E \boldsymbol{\epsilon}_{zz}^{-1} \mathbf{D}_y^H) & \mathbf{D}_y^E \boldsymbol{\epsilon}_{zz}^{-1} \mathbf{D}_x^H \end{bmatrix} \quad (1.4.15)$$

$$\frac{d}{dz'} \begin{bmatrix} \tilde{\mathbf{H}}_x \\ \tilde{\mathbf{H}}_y \end{bmatrix} = \mathbf{Q} \begin{bmatrix} \mathbf{E}_x \\ \mathbf{E}_y \end{bmatrix} \quad \mathbf{Q} = \begin{bmatrix} -\mathbf{D}_x^H \boldsymbol{\mu}_{zz}^{-1} \mathbf{D}_y^E & (\boldsymbol{\epsilon}_{yy} + \mathbf{D}_x^H \boldsymbol{\mu}_{zz}^{-1} \mathbf{D}_x^E) \\ -(\boldsymbol{\epsilon}_{xx} + \mathbf{D}_y^H \boldsymbol{\mu}_{zz}^{-1} \mathbf{D}_y^E) & \mathbf{D}_y^H \boldsymbol{\mu}_{zz}^{-1} \mathbf{D}_x^E \mathbf{E}_y \end{bmatrix} \quad (1.4.16)$$

From here, Eq. (1.4.15) is differentiated with respect to the  $z'$  variable.

$$\frac{d^2}{dz'^2} \begin{bmatrix} \mathbf{E}_x \\ \mathbf{E}_y \end{bmatrix} = \mathbf{P} \frac{d}{dz'} \begin{bmatrix} \tilde{\mathbf{H}}_x \\ \tilde{\mathbf{H}}_y \end{bmatrix} \quad (1.4.17)$$

At this point it can be seen that the left side of Eq. (1.4.17) is the same as the left side of Eq. (1.4.16). Eq. (1.4.16) is now substituted into Eq. (1.4.17) eliminating the magnetic fields.

$$\frac{d^2}{dz'^2} \begin{bmatrix} \mathbf{E}_x \\ \mathbf{E}_y \end{bmatrix} = \mathbf{PQ} \begin{bmatrix} \mathbf{E}_x \\ \mathbf{E}_y \end{bmatrix} \quad (1.4.18)$$

The wave equation can now be derived from Eq. (1.4.18).

$$\frac{d^2}{dz'^2} \begin{bmatrix} \mathbf{E}_x \\ \mathbf{E}_y \end{bmatrix} - \boldsymbol{\Omega}^2 \begin{bmatrix} \mathbf{E}_x \\ \mathbf{E}_y \end{bmatrix} = 0 \quad \boldsymbol{\Omega}^2 = \mathbf{PQ} \quad (1.4.19)$$

The second order differential equation in Eq. (1.4.19) is a very easy to solve equation that has a well-known analytical solution.

$$\begin{bmatrix} \mathbf{E}_x(z') \\ \mathbf{E}_y(z') \end{bmatrix} = e^{-\boldsymbol{\Omega}z'} \mathbf{a}^+ + e^{\boldsymbol{\Omega}z'} \mathbf{a}^- \quad (1.4.20)$$

In Eq. (1.4.20) the terms  $\mathbf{a}^+$  and  $\mathbf{a}^-$  are column vectors containing the proportionality constants of all the solved modes while the positive and negative superscripts denote forward and backward propagating waves. At this point in the derivations it is important to note that we are dealing with matrices. Because of this fact, a linear algebra identity must be implemented to be able to apply the  $e^{\boldsymbol{\Omega}z'}$  function. This identity states that for any arbitrary function  $f(\ )$  working on matrix  $\mathbf{A}$  can be implemented via the Jordan canonical form [46]:

$$f(\mathbf{A}) = \mathbf{W} \cdot f(\boldsymbol{\lambda}) \cdot \mathbf{W}^{-1} \quad (1.4.21)$$

In this equation  $\mathbf{W}$  is the eigenvector matrix calculated from  $\mathbf{\Omega}^2$ , and  $\lambda$  are the eigenvalues. This identity is applied to Eq. (1.4.20) to solve the exponential function.

$$\begin{bmatrix} \mathbf{E}_x(z') \\ \mathbf{E}_y(z') \end{bmatrix} = \mathbf{W}e^{-\lambda z'}\mathbf{W}^{-1}\mathbf{a}^+ + \mathbf{W}e^{\lambda z'}\mathbf{W}^{-1}\mathbf{a}^- \quad (1.4.22)$$

The proportionality constants of this equation have yet to be calculated. Because of this they can be combined with the  $\mathbf{W}^{-1}$  term to produce column vectors of proportionality constants, simplifying the equation.

$$\begin{bmatrix} \mathbf{E}_x(z') \\ \mathbf{E}_y(z') \end{bmatrix} = \mathbf{W}e^{-\lambda z'}\mathbf{c}^+ + \mathbf{W}e^{\lambda z'}\mathbf{c}^- \quad \begin{matrix} \mathbf{c}^+ = \mathbf{W}^{-1}\mathbf{a}^+ \\ \mathbf{c}^- = \mathbf{W}^{-1}\mathbf{a}^- \end{matrix} \quad (1.4.23)$$

The solution for the magnetic fields is derived the same way as with the electric field, except in this derivation,  $\mathbf{V}$  is used as the eigenvalue solution of the  $\mathbf{\Omega}^2$  term and has a negative sign assigned to it.

$$\begin{bmatrix} \tilde{\mathbf{H}}_x(z') \\ \tilde{\mathbf{H}}_y(z') \end{bmatrix} = -\mathbf{V}e^{-\lambda z'}\mathbf{c}^+ + \mathbf{V}e^{\lambda z'}\mathbf{c}^- \quad \begin{matrix} \mathbf{c}^+ = \mathbf{W}^{-1}\mathbf{a}^+ \\ \mathbf{c}^- = \mathbf{W}^{-1}\mathbf{a}^- \end{matrix} \quad (1.4.24)$$

At this point with all the information available, the variable  $\mathbf{V}$  can be solved for. First Eq. (1.4.24) is differentiated with respect to  $z'$ .

$$\frac{d}{dz'} \begin{bmatrix} \tilde{\mathbf{H}}_x(z') \\ \tilde{\mathbf{H}}_y(z') \end{bmatrix} = \mathbf{V}\lambda e^{-\lambda z'}\mathbf{c}^+ + \mathbf{V}\lambda e^{\lambda z'}\mathbf{c}^- \quad (1.4.25)$$

From here, Eq. (1.4.23) can be substituted into Eq. (1.4.16).

$$\frac{d}{dz'} \begin{bmatrix} \tilde{\mathbf{H}}_x \\ \tilde{\mathbf{H}}_y \end{bmatrix} = \mathbf{Q} \begin{bmatrix} \mathbf{E}_x(z') \\ \mathbf{E}_y(z') \end{bmatrix} = \mathbf{Q}\mathbf{W}e^{-\lambda z'}\mathbf{c}^+ + \mathbf{Q}\mathbf{W}e^{\lambda z'}\mathbf{c}^- \quad (1.4.26)$$

By inspecting Eqs. (1.4.25) and (1.4.26), it can be seen that the following is true.

$$\mathbf{V}\lambda = \mathbf{Q}\mathbf{W} \rightarrow \mathbf{V} = \mathbf{Q}\mathbf{W}\lambda^{-1} \quad (1.4.27)$$

With all the variables solved and accounted for Eqs. (1.4.23) and (1.4.24) can be put into block matrix form and given their own variable.

$$\Psi(z') = \begin{bmatrix} \mathbf{E}_x(z') \\ \mathbf{E}_y(z') \\ \tilde{\mathbf{H}}_x(z') \\ \tilde{\mathbf{H}}_y(z') \end{bmatrix} = \begin{bmatrix} \mathbf{W} & \mathbf{W} \\ -\mathbf{V} & \mathbf{V} \end{bmatrix} \begin{bmatrix} e^{-\lambda z'} & 0 \\ 0 & e^{\lambda z'} \end{bmatrix} \begin{bmatrix} \mathbf{c}^+ \\ \mathbf{c}^- \end{bmatrix} \quad (1.4.28)$$

This solution can be interpreted the following way.  $\Psi(z')$  is the sum of all the modes that exist in within the specified material segment or layer. The  $\mathbf{W}$  and  $\mathbf{V}$  terms are a square matrix that describes the modes that exist within the layer quantifying the relative amplitudes of the  $E$  and  $\tilde{H}$  fields while the  $e^{\lambda z'}$  term is a diagonal matrix describing the phase, loss or gain, and propagation of the modes. Term  $\mathbf{c}$  is a column vector containing all the amplitude coefficients of the modes.

At this point of the derivation, the complete picture of the MOL method for one layer is shown. For any practical application of this method, the solved fields needs to be iterated through each layer of the device and connected together. This is done with scattering matrices [47].

$$\begin{bmatrix} \mathbf{c}'_1 \\ \mathbf{c}'_2 \end{bmatrix} = \begin{bmatrix} \mathbf{S}_{11} & \mathbf{S}_{12} \\ \mathbf{S}_{21} & \mathbf{S}_{22} \end{bmatrix} \begin{bmatrix} \mathbf{c}'_1 \\ \mathbf{c}'_2 \end{bmatrix} \quad (1.4.29)$$

A scattering matrix is a matrix that is used to show the relationship of the reflection, and transmission of fields through a device. The scattering matrix is made up of four elements  $S_{11}$ ,  $S_{12}$ ,  $S_{21}$  and  $S_{22}$ . These elements are all related to one other and completely describe the scattering within.

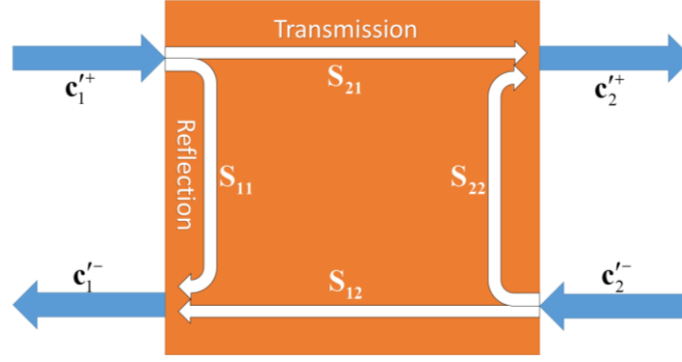


Figure 2.7: Scattering matrix showing transmission and reflection of a incidence wave.

It can be seen in Figure 2.7 that the  $S_{21}$  parameter corresponds to transmission and the  $S_{11}$  to reflection. This is consistent to the notation outlined in Ref. [47]. It is interesting to note that the nomenclature for scattering matrices is usually different for computational electromagnetics than it is for the experimental. In computational electromagnetics literature, the  $S_{11}$  refers to the transmission while the  $S_{21}$  is the reflection. There is no reason for this other than someone did it once and everyone just went along with it. For clarity, the scattering matrices used within this work will go with the experimental notation as outlined in Ref. [49]. With this information, the scattering matrices for the MOL method layers will be derived.

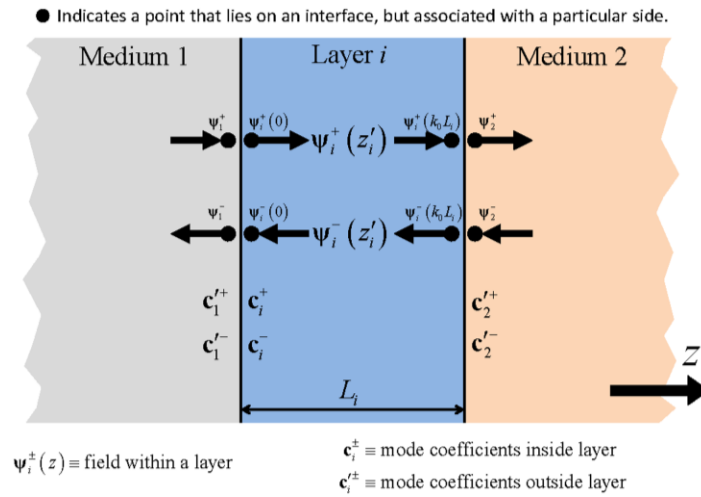


Figure 2.8: Scattering matrix showing the  $i$  layer. [36]

Figure 2.8 shows the relation of the fields between the different layers and how a scattering matrix can be applied to combine them together. This starts by generalizing the solution shown in Eq. (1.4.28) for the  $i^{\text{th}}$  layer.

$$\Psi_i(z'_i) = \begin{bmatrix} \mathbf{E}_{x,i}(z'_i) \\ \mathbf{E}_{y,i}(z'_i) \\ \tilde{\mathbf{H}}_{x,i}(z'_i) \\ \tilde{\mathbf{H}}_{y,i}(z'_i) \end{bmatrix} = \begin{bmatrix} \mathbf{W}_i & \mathbf{W}_i \\ -\mathbf{V}_i & \mathbf{V}_i \end{bmatrix} \begin{bmatrix} e^{-\lambda_i z'_i} & 0 \\ 0 & e^{\lambda_i z'_i} \end{bmatrix} \begin{bmatrix} \mathbf{c}_i^+ \\ \mathbf{c}_i^- \end{bmatrix} \quad (1.4.30)$$

From here the boundary conditions from the first interface are added to Eq. (1.4.30).

$$\Psi_1 = \Psi_i(0) \\ \begin{bmatrix} \mathbf{W}_1 & \mathbf{W}_1 \\ -\mathbf{V}_1 & \mathbf{V}_1 \end{bmatrix} \begin{bmatrix} \mathbf{c}_1^+ \\ \mathbf{c}_1^- \end{bmatrix} = \begin{bmatrix} \mathbf{W}_i & \mathbf{W}_i \\ -\mathbf{V}_i & \mathbf{V}_i \end{bmatrix} \begin{bmatrix} \mathbf{c}_i^+ \\ \mathbf{c}_i^- \end{bmatrix} \quad (1.4.31)$$

Note that in Eq. (1.4.31) the diagonal matrix describing the propagation and phase have been canceled out. This is because at this interface the distance that the wave has traveled is zero. When this value is inputted into the propagation matrix, the diagonal elements goes to one effectively making it an identity matrix. Next the boundary conditions for the second interface is added to Eq. (1.4.30).

$$\Psi_i(k_0 L_i) = \Psi_2 \\ \begin{bmatrix} \mathbf{W}_i & \mathbf{W}_i \\ -\mathbf{V}_i & \mathbf{V}_i \end{bmatrix} \begin{bmatrix} e^{-\lambda_i k_0 L_i} & 0 \\ 0 & e^{\lambda_i k_0 L_i} \end{bmatrix} \begin{bmatrix} \mathbf{c}_i^+ \\ \mathbf{c}_i^- \end{bmatrix} = \begin{bmatrix} \mathbf{W}_2 & \mathbf{W}_2 \\ -\mathbf{V}_2 & \mathbf{V}_2 \end{bmatrix} \begin{bmatrix} \mathbf{c}_2^+ \\ \mathbf{c}_2^- \end{bmatrix} \quad (1.4.32)$$

In this equation the propagation matrix is back because at this time the wave has traveled  $L_i$  distance. This value needs to be normalized, as this value is analytically solved for and wasn't absorbed into the matrix derivative operators. A  $k_0$  is multiplied to it. The  $i$  boundaries conditions are now solved for.

$$\begin{bmatrix} \mathbf{c}_i^+ \\ \mathbf{c}_i^- \end{bmatrix} = \begin{bmatrix} \mathbf{W}_i & \mathbf{W}_i \\ -\mathbf{V}_i & \mathbf{V}_i \end{bmatrix}^{-1} \begin{bmatrix} \mathbf{W}_1 & \mathbf{W}_1 \\ -\mathbf{V}_1 & \mathbf{V}_1 \end{bmatrix} \begin{bmatrix} \mathbf{c}_1^+ \\ \mathbf{c}_1^- \end{bmatrix} \quad (1.4.33)$$

$$\begin{bmatrix} \mathbf{c}_i^+ \\ \mathbf{c}_i^- \end{bmatrix} = \begin{bmatrix} e^{\lambda_i k_0 L} & 0 \\ 0 & e^{-\lambda_i k_0 L} \end{bmatrix} \begin{bmatrix} \mathbf{W}_i & \mathbf{W}_i \\ -\mathbf{V}_i & \mathbf{V}_i \end{bmatrix}^{-1} \begin{bmatrix} \mathbf{W}_2 & \mathbf{W}_2 \\ -\mathbf{V}_2 & \mathbf{V}_2 \end{bmatrix} \begin{bmatrix} \mathbf{c}_2^+ \\ \mathbf{c}_2^- \end{bmatrix} \quad (1.4.34)$$

At this point it can be seen through inspection of Eqs. (1.4.33) and (1.4.34) that they have terms in common. These terms are generalized and combined. This derivation can be seen in Appendix A5.

$$\begin{bmatrix} \mathbf{W}_i & \mathbf{W}_i \\ -\mathbf{V}_i & \mathbf{V}_i \end{bmatrix}^{-1} \begin{bmatrix} \mathbf{W}_j & \mathbf{W}_j \\ -\mathbf{V}_j & \mathbf{V}_j \end{bmatrix} = \frac{1}{2} \begin{bmatrix} \mathbf{A}_{ij} & \mathbf{B}_{ij} \\ \mathbf{B}_{ij} & \mathbf{A}_{ij} \end{bmatrix} \quad \begin{aligned} \mathbf{A}_{ij} &= \mathbf{W}_i^{-1} \mathbf{W}_j + \mathbf{V}_i^{-1} \mathbf{V}_j \\ \mathbf{B}_{ij} &= \mathbf{W}_i^{-1} \mathbf{W}_j - \mathbf{V}_i^{-1} \mathbf{V}_j \end{aligned} \quad (1.4.35)$$

$$\begin{bmatrix} e^{\lambda_i k_0 L_i} & \mathbf{0} \\ \mathbf{0} & e^{-\lambda_i k_0 L_i} \end{bmatrix} = \begin{bmatrix} \mathbf{X}_i^{-1} & \mathbf{0} \\ \mathbf{0} & \mathbf{X}_i \end{bmatrix} \quad \begin{aligned} \mathbf{X}_i &= e^{-\lambda_i k_0 L_i} \\ \mathbf{X}_i^{-1} &= e^{\lambda_i k_0 L_i} \end{aligned}$$

These generalized terms are now substituted into Eq. (1.4.33) and (1.4.34).

$$\begin{bmatrix} \mathbf{c}_i^+ \\ \mathbf{c}_i^- \end{bmatrix} = \frac{1}{2} \begin{bmatrix} \mathbf{A}_{i1} & \mathbf{B}_{i1} \\ \mathbf{B}_{i1} & \mathbf{A}_{i1} \end{bmatrix} \begin{bmatrix} \mathbf{c}_1^+ \\ \mathbf{c}_1^- \end{bmatrix} \quad \begin{aligned} \mathbf{A}_{i1} &= \mathbf{W}_i^{-1} \mathbf{W}_1 + \mathbf{V}_i^{-1} \mathbf{V}_1 \\ \mathbf{B}_{i1} &= \mathbf{W}_i^{-1} \mathbf{W}_1 - \mathbf{V}_i^{-1} \mathbf{V}_1 \end{aligned} \quad (1.4.36)$$

$$\begin{bmatrix} \mathbf{c}_i^+ \\ \mathbf{c}_i^- \end{bmatrix} = \frac{1}{2} \begin{bmatrix} \mathbf{X}_i^{-1} & \mathbf{0} \\ \mathbf{0} & \mathbf{X}_i \end{bmatrix} \begin{bmatrix} \mathbf{A}_{i2} & \mathbf{B}_{i2} \\ \mathbf{B}_{i2} & \mathbf{A}_{i2} \end{bmatrix} \begin{bmatrix} \mathbf{c}_2^+ \\ \mathbf{c}_2^- \end{bmatrix} \quad \begin{aligned} \mathbf{A}_{i2} &= \mathbf{W}_i^{-1} \mathbf{W}_2 + \mathbf{V}_i^{-1} \mathbf{V}_2 \\ \mathbf{B}_{i2} &= \mathbf{W}_i^{-1} \mathbf{W}_2 - \mathbf{V}_i^{-1} \mathbf{V}_2 \end{aligned} \quad (1.4.37)$$

From here, Eq. (1.4.36) is substituted into Eq. (1.4.37) to derive the scattering through the  $i$  layer from boundary one to two.

$$\frac{1}{2} \begin{bmatrix} \mathbf{A}_{i1} & \mathbf{B}_{i1} \\ \mathbf{B}_{i1} & \mathbf{A}_{i1} \end{bmatrix} \begin{bmatrix} \mathbf{c}_1^+ \\ \mathbf{c}_1^- \end{bmatrix} = \frac{1}{2} \begin{bmatrix} \mathbf{X}_i^{-1} & \mathbf{0} \\ \mathbf{0} & \mathbf{X}_i \end{bmatrix} \begin{bmatrix} \mathbf{A}_{i2} & \mathbf{B}_{i2} \\ \mathbf{B}_{i2} & \mathbf{A}_{i2} \end{bmatrix} \begin{bmatrix} \mathbf{c}_2^+ \\ \mathbf{c}_2^- \end{bmatrix} \quad (1.4.38)$$

The terms  $\mathbf{c}_1^-$ , and  $\mathbf{c}_2^+$ , are then individually solved for from Eq. (1.4.38). This is done in a very specific way as to make this method numerically stable. The final derivation must not have any inverse  $\mathbf{X}_i$  components in the solutions as this is a known cause of this method becoming unstable and numerically exploding [48]. The derivation of these terms can be seen in Appendix A5.

$$\begin{aligned} \mathbf{c}_1^{\leftarrow} = & \left( \mathbf{A}_{i1} - \mathbf{X}_i \mathbf{B}_{i2} \mathbf{A}_{i2}^{-1} \mathbf{X}_i \mathbf{B}_{i1} \right)^{-1} \left( \mathbf{X}_i \mathbf{B}_{i2} \mathbf{A}_{i2}^{-1} \mathbf{X}_i \mathbf{A}_{i1} - \mathbf{B}_{i1} \right) \mathbf{c}_1^{\rightarrow} + \dots \\ & \left( \mathbf{A}_{i1} - \mathbf{X}_i \mathbf{B}_{i2} \mathbf{A}_{i2}^{-1} \mathbf{X}_i \mathbf{B}_{i1} \right)^{-1} \mathbf{X}_i \left( \mathbf{A}_{i2} - \mathbf{B}_{i2} \mathbf{A}_{i2}^{-1} \mathbf{B}_{i2} \right) \mathbf{c}_2^{\leftarrow} \end{aligned} \quad (1.4.39)$$

$$\begin{aligned} \mathbf{c}_2^{\rightarrow} = & \left( \mathbf{A}_{i2} - \mathbf{X}_i \mathbf{B}_{i1} \mathbf{A}_{i1}^{-1} \mathbf{X}_i \mathbf{B}_{i2} \right)^{-1} \mathbf{X}_i \left( \mathbf{A}_{i1} - \mathbf{B}_{i1} \mathbf{A}_{i1}^{-1} \mathbf{B}_{i1} \right) \mathbf{c}_1^{\rightarrow} - \dots \\ & \left( \mathbf{A}_{i2} - \mathbf{X}_i \mathbf{B}_{i1} \mathbf{A}_{i1}^{-1} \mathbf{X}_i \mathbf{B}_{i2} \right)^{-1} \left( \mathbf{B}_{i2} + \mathbf{X}_i \mathbf{B}_{i1} \mathbf{A}_{i1}^{-1} \mathbf{X}_i \mathbf{A}_{i2} \right) \mathbf{c}_2^{\leftarrow} \end{aligned}$$

Eq. (1.4.39) is now put into the standard scattering matrix form.

$$\begin{aligned} \begin{bmatrix} \mathbf{c}_1^{\leftarrow} \\ \mathbf{c}_2^{\rightarrow} \end{bmatrix} &= \begin{bmatrix} \mathbf{S}_{11}^i & \mathbf{S}_{12}^i \\ \mathbf{S}_{21}^i & \mathbf{S}_{22}^i \end{bmatrix} \begin{bmatrix} \mathbf{c}_1^{\rightarrow} \\ \mathbf{c}_2^{\leftarrow} \end{bmatrix} \\ \mathbf{S}_{11}^i &= \left( \mathbf{A}_{i1} - \mathbf{X}_i \mathbf{B}_{i2} \mathbf{A}_{i2}^{-1} \mathbf{X}_i \mathbf{B}_{i1} \right)^{-1} \left( \mathbf{X}_i \mathbf{B}_{i2} \mathbf{A}_{i2}^{-1} \mathbf{X}_i \mathbf{A}_{i1} - \mathbf{B}_{i1} \right) \\ \mathbf{S}_{12}^i &= \left( \mathbf{A}_{i1} - \mathbf{X}_i \mathbf{B}_{i2} \mathbf{A}_{i2}^{-1} \mathbf{X}_i \mathbf{B}_{i1} \right)^{-1} \mathbf{X}_i \left( \mathbf{A}_{i2} - \mathbf{B}_{i2} \mathbf{A}_{i2}^{-1} \mathbf{B}_{i2} \right) \\ \mathbf{S}_{21}^i &= \left( \mathbf{A}_{i2} - \mathbf{X}_i \mathbf{B}_{i1} \mathbf{A}_{i1}^{-1} \mathbf{X}_i \mathbf{B}_{i2} \right)^{-1} \mathbf{X}_i \left( \mathbf{A}_{i1} - \mathbf{B}_{i1} \mathbf{A}_{i1}^{-1} \mathbf{B}_{i1} \right) \\ \mathbf{S}_{22}^i &= \left( \mathbf{A}_{i2} - \mathbf{X}_i \mathbf{B}_{i1} \mathbf{A}_{i1}^{-1} \mathbf{X}_i \mathbf{B}_{i2} \right)^{-1} \left( \mathbf{B}_{i2} + \mathbf{X}_i \mathbf{B}_{i1} \mathbf{A}_{i1}^{-1} \mathbf{X}_i \mathbf{A}_{i2} \right) \end{aligned} \quad (1.4.40)$$

The scattering matrices derived thus far would be perfectly adequate to implement the MOL method, but a better derivation exists. In Ref. [49], the author introduces a new way to implement the scattering matrix method building on the traditional derivation described in this work. In this derivation, a gap of air with zero thickness is placed on either side of the  $i^{\text{th}}$  boundary. This has the effect of making the derivation of the scattering matrix symmetric, minimizes the amount of calculations needed by half and reduces the amount of memory needed to store the numbers. The scattering matrix parameters are rederived incorporating this air gap.

$$\begin{bmatrix} \mathbf{c}_1^- \\ \mathbf{c}_2^+ \end{bmatrix} = \begin{bmatrix} \mathbf{S}_{11}^i & \mathbf{S}_{12}^i \\ \mathbf{S}_{21}^i & \mathbf{S}_{22}^i \end{bmatrix} \begin{bmatrix} \mathbf{c}_1^+ \\ \mathbf{c}_2^- \end{bmatrix}$$

$$\begin{aligned} \mathbf{S}_{11}^i &= (\mathbf{A}_i - \mathbf{X}_i \mathbf{B}_i \mathbf{A}_i^{-1} \mathbf{X}_i \mathbf{B}_i)^{-1} (\mathbf{X}_i \mathbf{B}_i \mathbf{A}_i^{-1} \mathbf{X}_i \mathbf{A}_i - \mathbf{B}_i) & \mathbf{A}_{i1} &= \mathbf{W}_i^{-1} \mathbf{W}_0 + \mathbf{V}_i^{-1} \mathbf{V}_0 \\ \mathbf{S}_{12}^i &= (\mathbf{A}_i - \mathbf{X}_i \mathbf{B}_i \mathbf{A}_i^{-1} \mathbf{X}_i \mathbf{B}_i)^{-1} \mathbf{X}_i (\mathbf{A}_i - \mathbf{B}_i \mathbf{A}_i^{-1} \mathbf{B}_i) & \mathbf{B}_{i1} &= \mathbf{W}_i^{-1} \mathbf{W}_0 - \mathbf{V}_i^{-1} \mathbf{V}_0 \\ \mathbf{S}_{21}^i &= \mathbf{S}_{12}^i \\ \mathbf{S}_{22}^i &= \mathbf{S}_{11}^i \end{aligned}$$

(1.4.41)

In this formulation  $\mathbf{W}_0$  and  $\mathbf{V}_0$  are the original values calculated with the material in them being free-space. Because we implemented the scattering matrix this way, two additional boundaries need to be added. These boundaries need to be added to the reflection and transmitted sides and are derived with the assumption in that there is only one boundary. The reflection side boundary is derived as

$$\begin{aligned} \mathbf{S}_{11}^{\text{ref}} &= -\mathbf{A}_{i1}^{-1} \mathbf{B}_{i1} \\ \mathbf{S}_{12}^{\text{ref}} &= 2\mathbf{A}_{i1}^{-1} & \mathbf{A}_{i1} &= \mathbf{W}_0^{-1} \mathbf{W}_{\text{ref}} + \mathbf{V}_0^{-1} \mathbf{V}_{\text{ref}} \\ \mathbf{S}_{21}^{\text{ref}} &= \frac{1}{2} (\mathbf{A}_{i1} - \mathbf{B}_{i1} \mathbf{A}_{i1}^{-1} \mathbf{B}_{i1}) & \mathbf{B}_{i1} &= \mathbf{W}_0^{-1} \mathbf{W}_{\text{ref}} - \mathbf{V}_0^{-1} \mathbf{V}_{\text{ref}} \\ \mathbf{S}_{22}^{\text{ref}} &= \mathbf{B}_{i1} \mathbf{A}_{i1}^{-1} \end{aligned} \quad (1.4.42)$$

where  $\mathbf{W}_{\text{ref}}$  and  $\mathbf{V}_{\text{ref}}$  are calculated with the material that the reflection side is made of. The transmission side boundary is derived as

$$\begin{aligned} \mathbf{S}_{11}^{\text{tm}} &= \mathbf{B}_{i2} \mathbf{A}_{i2}^{-1} \\ \mathbf{S}_{12}^{\text{tm}} &= \frac{1}{2} (\mathbf{A}_{i2} - \mathbf{B}_{i2} \mathbf{A}_{i2}^{-1} \mathbf{B}_{i2}) & \mathbf{A}_{i2} &= \mathbf{W}_0^{-1} \mathbf{W}_{\text{tm}} + \mathbf{V}_0^{-1} \mathbf{V}_{\text{tm}} \\ \mathbf{S}_{21}^{\text{tm}} &= 2\mathbf{A}_{i2}^{-1} & \mathbf{B}_{i2} &= \mathbf{W}_0^{-1} \mathbf{W}_{\text{tm}} - \mathbf{V}_0^{-1} \mathbf{V}_{\text{tm}} \\ \mathbf{S}_{22}^{\text{tm}} &= -\mathbf{A}_{i2}^{-1} \mathbf{B}_{i2} \end{aligned} \quad (1.4.43)$$

where  $\mathbf{W}_{\text{tm}}$  and  $\mathbf{V}_{\text{tm}}$  are calculated with the material that the transmission side is made of.

At this point in the formulation all the components are in place. All that remains is implementing a source and propagating said source through all the layers, connecting and

combining all the scattering matrices together along the way. When connecting and combining the scattering matrices together, a simple multiplication does not work. These matrices need to be connected and combined through an the Redheffer's star product [50] and [51]. Redheffer's star product is defined as the following:

$$\mathbf{S} = \mathbf{S}_a \otimes \mathbf{S}_b \quad \mathbf{S}_a = \begin{bmatrix} \mathbf{a}_{11} & \mathbf{a}_{12} \\ \mathbf{a}_{21} & \mathbf{a}_{22} \end{bmatrix} \quad \mathbf{S}_b = \begin{bmatrix} \mathbf{b}_{11} & \mathbf{b}_{12} \\ \mathbf{b}_{21} & \mathbf{b}_{22} \end{bmatrix} \quad (1.4.44)$$

where

$$\begin{aligned} \mathbf{S} &= \begin{bmatrix} \mathbf{S}_{11} & \mathbf{S}_{12} \\ \mathbf{S}_{21} & \mathbf{S}_{22} \end{bmatrix} \\ \mathbf{S}_{11} &= \mathbf{a}_{11} + \mathbf{a}_{12} (\mathbf{I} - \mathbf{b}_{11} \mathbf{a}_{22})^{-1} \mathbf{b}_{11} \mathbf{a}_{21} \\ \mathbf{S}_{12} &= \mathbf{a}_{12} (\mathbf{I} - \mathbf{b}_{11} \mathbf{a}_{22})^{-1} \mathbf{b}_{12} \\ \mathbf{S}_{21} &= \mathbf{b}_{21} (\mathbf{I} - \mathbf{a}_{22} \mathbf{b}_{11})^{-1} \mathbf{a}_{21} \\ \mathbf{S}_{22} &= \mathbf{b}_{22} + \mathbf{b}_{21} (\mathbf{I} - \mathbf{a}_{22} \mathbf{b}_{11})^{-1} \mathbf{a}_{22} \mathbf{b}_{12} \end{aligned} \quad (1.4.45)$$

A complete derivation of the Redheffer's star product can be viewed in Appendix A6. The scattering matrices are combined in order using this method with the reflected and transmitted regions, calculating one global scattering matrix as seen in Figure 2.9.

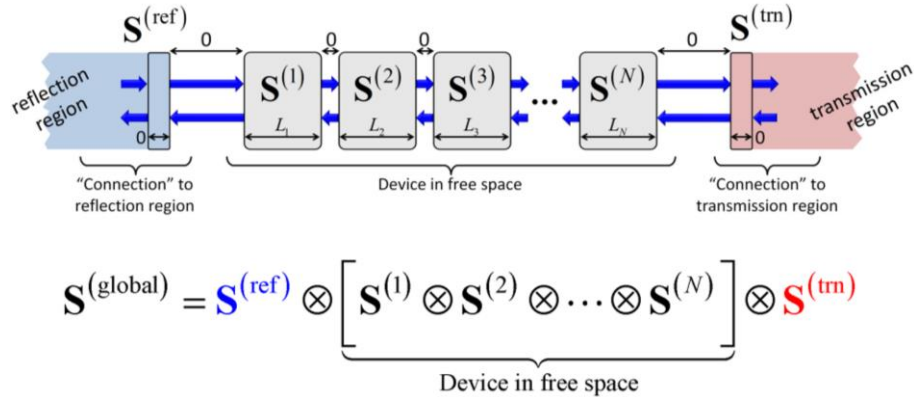


Figure 2.9: Illustration of the calculation of the global scattering matrix combining all the layers.[49]

All that remains is to calculate the transmitted and reflected powers. This is accomplished by first defining the equation for the incident field. Since the assumption of the infinite material reflection layer was added to the problem, its materials are used in the derivation

$$\begin{aligned} E_{\text{inc}}^x &= e^{-j(k_x^{\text{inc}} x)} & k_x^{\text{inc}} &= k_0 \sqrt{\epsilon_{\text{ref}} \mu_{\text{ref}}} \sin \theta \sin \phi \\ E_{\text{inc}}^y &= e^{-j(k_y^{\text{inc}} y)} & k_y^{\text{inc}} &= k_0 \sqrt{\epsilon_{\text{ref}} \mu_{\text{ref}}} \cos \theta \sin \phi \\ E_{\text{inc}}^z &= e^{-j(k_z^{\text{inc}} z)} & k_z^{\text{inc}} &= k_0 \sqrt{\epsilon_{\text{ref}} \mu_{\text{ref}}} \cos \theta \end{aligned} \quad (1.4.46)$$

From here, these incident reflected and transmitted field values are related to the global scattering matrix through the mode coefficients.

$$\begin{bmatrix} \mathbf{c}_{\text{ref}} \\ \mathbf{c}_{\text{trn}} \end{bmatrix} = \begin{bmatrix} \mathbf{S}_{11}^{(\text{global})} & \mathbf{S}_{12}^{(\text{global})} \\ \mathbf{S}_{21}^{(\text{global})} & \mathbf{S}_{22}^{(\text{global})} \end{bmatrix} \begin{bmatrix} \mathbf{c}_{\text{inc}} \\ 0 \end{bmatrix} \quad \mathbf{c}_{\text{inc}} = \mathbf{W}_{\text{ref}}^{-1} \begin{bmatrix} E_{\text{inc}}^x \\ E_{\text{inc}}^y \end{bmatrix} \quad (1.4.47)$$

Simplifying this equation yields:

$$\begin{aligned} \mathbf{c}_{\text{ref}} &= \mathbf{S}_{11}^{(\text{global})} \mathbf{c}_{\text{inc}} \\ \mathbf{c}_{\text{trn}} &= \mathbf{S}_{21}^{(\text{global})} \mathbf{c}_{\text{inc}} \end{aligned} \quad (1.4.48)$$

Using the definition of the scattering matrix it is known that

$$\begin{aligned} \begin{bmatrix} E_x^{\text{ref}} \\ E_y^{\text{ref}} \end{bmatrix} &= \mathbf{W}_{\text{ref}} \mathbf{S}_{11}^{(\text{global})} \mathbf{W}_{\text{ref}}^{-1} \begin{bmatrix} E_x^{\text{inc}} \\ E_y^{\text{inc}} \end{bmatrix} \\ \begin{bmatrix} E_x^{\text{trn}} \\ E_y^{\text{trn}} \end{bmatrix} &= \mathbf{W}_{\text{trn}} \mathbf{S}_{21}^{(\text{global})} \mathbf{W}_{\text{ref}}^{-1} \begin{bmatrix} E_x^{\text{inc}} \\ E_y^{\text{inc}} \end{bmatrix} \end{aligned} \quad (1.4.49)$$

A FFT is now applied to the calculated reflected and transmitted fields. This calculates the complex amplitudes of all the spatial harmonics within these region.

$$\begin{aligned} S_x^{\text{ref}}(m) &= \text{FFT} \{ E_x^{\text{ref}}(x) \} \\ S_y^{\text{ref}}(n) &= \text{FFT} \{ E_y^{\text{ref}}(y) \} \\ S_x^{\text{trn}}(m) &= \text{FFT} \{ E_x^{\text{trn}}(x) \} \\ S_y^{\text{trn}}(n) &= \text{FFT} \{ E_y^{\text{trn}}(y) \} \end{aligned} \quad (1.4.50)$$

Next the  $\vec{k}$  vectors of the spatial harmonics must be expanded and quantified to be able to calculate the longitudinal field components.

$$\begin{aligned} k_{x,m} &= k_x^{\text{inc}} - \frac{2\pi m}{\Lambda_x} & m = \dots, -2, -1, 0, 1, 2, \dots \\ k_{y,n} &= k_y^{\text{inc}} - \frac{2\pi n}{\Lambda_y} & n = \dots, -2, -1, 0, 1, 2, \dots \end{aligned} \quad (1.4.51)$$

These terms are used to calculate the longitudinal  $\vec{k}$  vectors in the reflected and transmitted region.

$$\begin{aligned} k_{z,m,n}^{\text{ref}} &= \sqrt{k_0^2 \sqrt{\epsilon_{\text{ref}} \mu_{\text{ref}}} - k_{x,m}^2 - k_{y,n}^2} \\ k_{z,m,n}^{\text{tm}} &= \sqrt{k_0^2 \sqrt{\epsilon_{\text{tm}} \mu_{\text{tm}}} - k_{x,m}^2 - k_{y,n}^2} \end{aligned} \quad (1.4.52)$$

Using the divergence equation, the values obtained in Eq. (1.4.52) are used to calculate the longitudinal field component for the reflected and transmitted regions. The derivation of the longitudinal field component can be viewed in Appendix A7.

$$\begin{aligned} S_z^{\text{ref}} &= \frac{-k_{x,m} S_x^{\text{ref}} - k_{y,n} S_y^{\text{ref}}}{k_z^{\text{ref}}} \\ S_z^{\text{tm}} &= \frac{-k_{x,m} S_x^{\text{tm}} - k_{y,n} S_y^{\text{tm}}}{k_z^{\text{tm}}} \end{aligned} \quad (1.4.53)$$

The plane-wave component fields for the reflected and transmitted regions are combined using Pythagoras's theorem [52].

$$\begin{aligned} |S_{\text{ref}}|^2 &= |S_x^{\text{ref}}|^2 + |S_y^{\text{ref}}|^2 + |S_z^{\text{ref}}|^2 \\ |S_{\text{tm}}|^2 &= |S_x^{\text{tm}}|^2 + |S_y^{\text{tm}}|^2 + |S_z^{\text{tm}}|^2 \end{aligned} \quad (1.4.54)$$

The total power reflected and transmitted through the device is now calculated.

$$\begin{aligned}
REF &= \sum_{i=1}^m \sum_{j=1}^n \operatorname{Re} \left[ \frac{k_{z,m,n}^{\text{ref}}(i,j)}{k_z^{\text{inc}}} \right] \cdot |S_{\text{ref}}(i,j)|^2 \\
TRN &= \sum_{i=1}^m \sum_{j=1}^n \operatorname{Re} \left[ \frac{\mu_{\text{inc}} k_{z,m,n}^{\text{trn}}(i,j)}{\mu_{\text{trn}} k_z^{\text{inc}}} \right] \cdot |S_{\text{trn}}(i,j)|^2
\end{aligned} \tag{1.4.55}$$

The MOL method is a very powerful tool for the design of metallic FSSs and other periodic devices. It provides a fully rigorous solution to Maxwell's equation and its semi-analytical formulation makes it a very fast fully 3D model that doesn't take as much computation power as other methods. Though powerful, it does have its drawbacks. One of these drawbacks is that it scales very poorly in the transverse directions. This makes simulations of devices with very fine features slow. Another drawback is that field visualizations are very cumbersome to implement. This problem is made more apparent when compared to ease of field visualizations with the FDFD and FDTD methods. The last drawback is that it isn't formulated to model non-periodic devices. The formulation can be rederived to account for non-periodicity, but this adds complexity and there are better methods out there, like FDTD, for the analysis of large non-periodic devices. Through these problems though, this is an excellent method for the study and design of metallic slot and element FSSs.

### 2.3 Rigorous Coupled-Wave Analysis

Like its brother MOL, rigorous coupled-wave analysis (RCWA) is a fully 3D semi-analytical modeling technique used to simulate the electromagnetic interaction and response of different materials and complex devices in the frequency domain [48] and [53]. RCWA provides a fully rigorous solution to Maxwell's equations. This method is extremely fast for modeling all-dielectric structures, and unconditionally stable while providing accurate results. This is the de facto method for the design and analysis of all-dielectric FSSs using GMR.

RCWA works exactly the same as MOL except when discretizing the  $x$  and  $y$  variables. To discretize these variables, Maxwell's equations are transformed to be in Fourier space and then solved. Fourier space was chosen for this method because most of the fields inside dielectrics take on the form of plane-waves and can be approximated very accurately with a finite number of plane-

wave components, spatial harmonics. This is because in general, dielectrics interact less with the fields and most devices are assumed to be operating in the far-field. This leads to a plane-wave shape and composition inside the dielectrics. Expanding into this basis allows for very efficient and fast solutions to be calculated.

It can be seen in Figure 2.10 that in this method an incident plane-wave excites a propagating mode that is approximated with a finite number of spatial harmonics in the first dielectric layer. This mode is then analytically propagated in the  $z$  direction where it meets the second interface. At this interface the power in the mode is shuffled and a new mode is excited and approximated with spatial harmonics. These two modes are connected and combined with scattering matrices, the same as MOL. This process is repeated through all the layers generating a global scattering matrix which describes the overall response of the device.

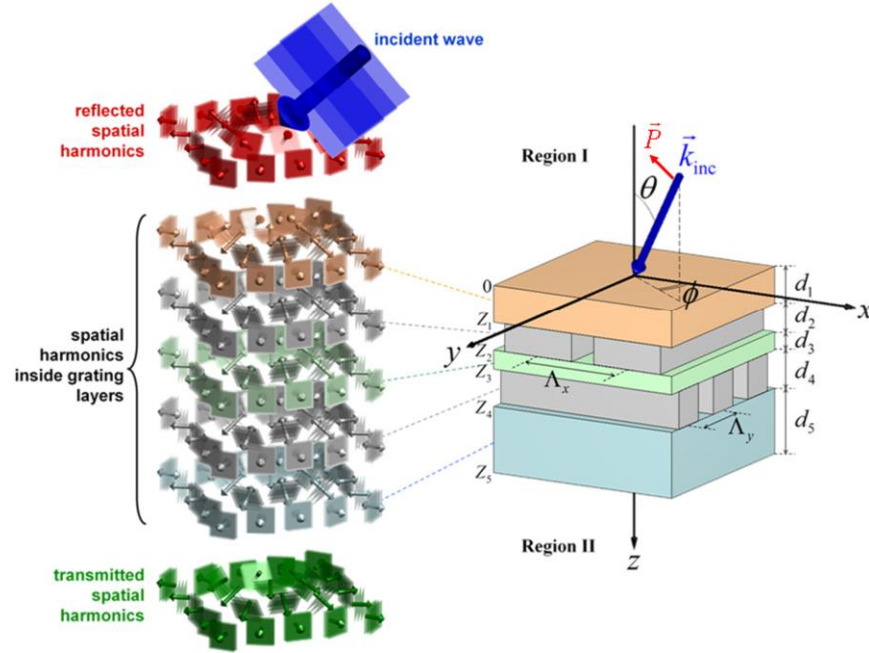


Figure 2.10: Illustration of the RCWA method showing the spatial harmonics generated from an incident wave inside dielectric layers. [36]

This method starts with Maxwell's curl equations normalized with an isotropic material assumption and expanded.

$$\begin{aligned}
\frac{\partial \vec{E}_z}{\partial y} - \frac{\partial \vec{E}_y}{\partial z} &= k_0 \mu_r \tilde{H}_x \\
\frac{\partial \vec{E}_x}{\partial z} - \frac{\partial \vec{E}_z}{\partial x} &= k_0 \mu_r \tilde{H}_y \\
\frac{\partial \vec{E}_y}{\partial x} - \frac{\partial \vec{E}_x}{\partial y} &= k_0 \mu_r \tilde{H}_z
\end{aligned} \tag{1.5.1}$$

$$\begin{aligned}
\frac{\partial \tilde{H}_z}{\partial y} - \frac{\partial \tilde{H}_y}{\partial z} &= k_0 \varepsilon_r \vec{E}_x \\
\frac{\partial \tilde{H}_x}{\partial z} - \frac{\partial \tilde{H}_z}{\partial x} &= k_0 \varepsilon_r \vec{E}_y \\
\frac{\partial \tilde{H}_y}{\partial x} - \frac{\partial \tilde{H}_x}{\partial y} &= k_0 \varepsilon_r \vec{E}_z
\end{aligned} \tag{1.5.2}$$

As they are now, these equations are in real space. To implement this method, these equations need to be transformed into Fourier space. First, a Fourier expansion of the materials in the  $x$ - $y$  plane is applied.

$$\begin{aligned}
\varepsilon_r(x, y) &= \sum_{m=-\infty}^{\infty} \sum_{n=-\infty}^{\infty} a_{m,n} e^{j\left(\frac{2\pi mx}{\Lambda_x} + \frac{2\pi ny}{\Lambda_y}\right)} \\
a_{m,n} &= \frac{1}{\Lambda_x \Lambda_y} \int_{-\Lambda_x/2}^{\Lambda_x/2} \int_{-\Lambda_y/2}^{\Lambda_y/2} \varepsilon_r(x, y) e^{j\left(\frac{2\pi mx}{\Lambda_x} + \frac{2\pi ny}{\Lambda_y}\right)} dx dy \\
\mu_r(x, y) &= \sum_{m=-\infty}^{\infty} \sum_{n=-\infty}^{\infty} b_{m,n} e^{j\left(\frac{2\pi mx}{\Lambda_x} + \frac{2\pi ny}{\Lambda_y}\right)} \\
b_{m,n} &= \frac{1}{\Lambda_x \Lambda_y} \int_{-\Lambda_x/2}^{\Lambda_x/2} \int_{-\Lambda_y/2}^{\Lambda_y/2} \mu_r(x, y) e^{j\left(\frac{2\pi mx}{\Lambda_x} + \frac{2\pi ny}{\Lambda_y}\right)} dx dy
\end{aligned} \tag{1.5.3}$$

Next a Fourier expansion is applied to the fields.

$$\begin{aligned}
E_x(x, y, z) &= \sum_{m=-\infty}^{\infty} \sum_{n=-\infty}^{\infty} S_{x,m,n}(z) \cdot e^{-j(k_{x,m}x + k_{y,n}y)} \\
E_y(x, y, z) &= \sum_{m=-\infty}^{\infty} \sum_{n=-\infty}^{\infty} S_{y,m,n}(z) \cdot e^{-j(k_{x,m}x + k_{y,n}y)} \quad k_{x,m} = k_{x,inc} - \frac{2\pi m}{\Lambda_x} \\
E_z(x, y, z) &= \sum_{m=-\infty}^{\infty} \sum_{n=-\infty}^{\infty} S_{z,m,n}(z) \cdot e^{-j(k_{x,m}x + k_{y,n}y)} \quad m = -\infty, \dots, -2, -1, 0, 1, 2, \dots, \infty
\end{aligned} \tag{1.5.4}$$

$$\begin{aligned}
\tilde{H}_x(x, y, z) &= \sum_{m=-\infty}^{\infty} \sum_{n=-\infty}^{\infty} U_{x,m,n}(z) \cdot e^{-j(k_{x,m}x + k_{y,n}y)} \quad k_{y,n} = k_{y,inc} - \frac{2\pi n}{\Lambda_y} \\
\tilde{H}_y(x, y, z) &= \sum_{m=-\infty}^{\infty} \sum_{n=-\infty}^{\infty} U_{y,m,n}(z) \cdot e^{-j(k_{x,m}x + k_{y,n}y)} \quad n = -\infty, \dots, -2, -1, 0, 1, 2, \dots, \infty \\
\tilde{H}_z(x, y, z) &= \sum_{m=-\infty}^{\infty} \sum_{n=-\infty}^{\infty} U_{z,m,n}(z) \cdot e^{-j(k_{x,m}x + k_{y,n}y)}
\end{aligned}$$

Eqs. (1.5.3) and (1.5.4) are substituted into Eqs. (1.5.1) and (1.5.2). After this the partial derivatives are taken of each of the terms except for the  $\frac{\partial}{\partial z}$  terms. This term is left to be solved

analytically like the MOL method detailed in Section 2.2. Like the MOL method, this partial derivative becomes a regular derivative because it is the only un-discretized variable left. This leads to the following terms.

$$\begin{aligned}
-jk_{y,m}U_{z,m,n}(z) - \frac{dU_{y,m,n}(z)}{dz} &= k_0 \sum_{q=-\infty}^{\infty} \sum_{r=-\infty}^{\infty} a_{m-q,n-r} S_{x,q,r}(z) \\
\frac{dU_{x,m,n}(z)}{dz} + jk_{x,m}U_{z,m,n}(z) &= k_0 \sum_{q=-\infty}^{\infty} \sum_{r=-\infty}^{\infty} a_{m-q,n-r} S_{y,q,r}(z) \\
-jk_{x,m}U_{y,m,n}(z) + jk_{y,m}U_{x,m,n}(z) &= k_0 \sum_{q=-\infty}^{\infty} \sum_{r=-\infty}^{\infty} a_{m-q,n-r} S_{z,q,r}(z)
\end{aligned} \tag{1.5.5}$$

$$\begin{aligned}
-jk_{y,m}U_{z,m,n}(z) - \frac{dS_{y,m,n}(z)}{dz} &= k_0 \sum_{q=-\infty}^{\infty} \sum_{r=-\infty}^{\infty} a_{m-q,n-r} U_{x,q,r}(z) \\
\frac{dS_{x,m,n}(z)}{dz} + jk_{x,m}S_{z,m,n}(z) &= k_0 \sum_{q=-\infty}^{\infty} \sum_{r=-\infty}^{\infty} a_{m-q,n-r} U_{y,q,r}(z) \\
-jk_{x,m}S_{y,m,n}(z) + jk_{y,m}S_{x,m,n}(z) &= k_0 \sum_{q=-\infty}^{\infty} \sum_{r=-\infty}^{\infty} a_{m-q,n-r} U_{z,q,r}(z)
\end{aligned} \tag{1.5.6}$$

From here these equations can be normalized. This normalization is absorbed into the  $\tilde{k}$  wave vectors in these equations.

$$\tilde{k}_x = \frac{k_x}{k_0} \quad \tilde{k}_y = \frac{k_y}{k_0} \quad \tilde{k}_z = \frac{k_z}{k_0} \quad (1.5.7)$$

Applying this normalization yields:

$$\begin{aligned} -j\tilde{k}_{y,m}U_{z,m,n}(\tilde{z}) - \frac{dU_{y,m,n}(\tilde{z})}{d\tilde{z}} &= \sum_{q=-\infty}^{\infty} \sum_{r=-\infty}^{\infty} a_{m-q,n-r} S_{x,q,r}(\tilde{z}) \\ \frac{dU_{x,m,n}(\tilde{z})}{d\tilde{z}} + j\tilde{k}_{x,m}U_{z,m,n}(\tilde{z}) &= \sum_{q=-\infty}^{\infty} \sum_{r=-\infty}^{\infty} a_{m-q,n-r} S_{y,q,r}(\tilde{z}) \end{aligned} \quad (1.5.8)$$

$$\begin{aligned} -j\tilde{k}_{x,m}U_{y,m,n}(\tilde{z}) + j\tilde{k}_{y,m}U_{x,m,n}(\tilde{z}) &= \sum_{q=-\infty}^{\infty} \sum_{r=-\infty}^{\infty} a_{m-q,n-r} S_{z,q,r}(\tilde{z}) \\ -j\tilde{k}_{y,m}U_{z,m,n}(\tilde{z}) - \frac{dS_{y,m,n}(\tilde{z})}{d\tilde{z}} &= \sum_{q=-\infty}^{\infty} \sum_{r=-\infty}^{\infty} a_{m-q,n-r} U_{x,q,r}(\tilde{z}) \\ \frac{dS_{x,m,n}(\tilde{z})}{d\tilde{z}} + j\tilde{k}_{x,m}S_{z,m,n}(\tilde{z}) &= \sum_{q=-\infty}^{\infty} \sum_{r=-\infty}^{\infty} a_{m-q,n-r} U_{y,q,r}(\tilde{z}) \\ -j\tilde{k}_{x,m}S_{y,m,n}(\tilde{z}) + j\tilde{k}_{y,m}S_{x,m,n}(\tilde{z}) &= \sum_{q=-\infty}^{\infty} \sum_{r=-\infty}^{\infty} a_{m-q,n-r} U_{z,q,r}(\tilde{z}) \end{aligned} \quad (1.5.9)$$

By careful inspection it can be seen that these equations need to be written for each spatial harmonic used in each layer. To accomplish this, each of the terms in these equations are put into matrix form. Examples of these matrix forms are given below.

$$\begin{aligned} \mathbf{K}_x &= \begin{bmatrix} \tilde{k}_{x,1,1} & 0 & 0 \\ 0 & \ddots & 0 \\ 0 & 0 & \tilde{k}_{x,M,N} \end{bmatrix} & \mathbf{K}_y &= \begin{bmatrix} \tilde{k}_{y,1,1} & 0 & 0 \\ 0 & \ddots & 0 \\ 0 & 0 & \tilde{k}_{y,M,N} \end{bmatrix} \\ \mathbf{K}_z &= \begin{bmatrix} \tilde{k}_{z,1,1} & 0 & 0 \\ 0 & \ddots & 0 \\ 0 & 0 & \tilde{k}_{z,M,N} \end{bmatrix} \end{aligned} \quad (1.5.10)$$

$$\mathbf{u}_x = \begin{bmatrix} U_{x,1,1} \\ U_{x,1,2} \\ \vdots \\ U_{x,M,N} \end{bmatrix} \quad \mathbf{u}_y = \begin{bmatrix} U_{y,1,1} \\ U_{y,1,2} \\ \vdots \\ U_{y,M,N} \end{bmatrix} \quad \mathbf{u}_z = \begin{bmatrix} U_{z,1,1} \\ U_{z,1,2} \\ \vdots \\ U_{z,M,N} \end{bmatrix} \quad (1.5.11)$$

$$\mathbf{s}_x = \begin{bmatrix} S_{x,1,1} \\ S_{x,1,2} \\ \vdots \\ S_{x,M,N} \end{bmatrix} \quad \mathbf{s}_y = \begin{bmatrix} S_{y,1,1} \\ S_{y,1,2} \\ \vdots \\ S_{y,M,N} \end{bmatrix} \quad \mathbf{s}_z = \begin{bmatrix} S_{z,1,1} \\ S_{z,1,2} \\ \vdots \\ S_{z,M,N} \end{bmatrix}$$

It is also seen that the double summations on the left hand side of the Eqs. (1.5.10) and (1.5.11) take on the form of a Cauchy product which can be defined as a discrete convolution [54]. A discrete convolution is a linear operation that can be made into a matrix operator, much like the derivative operators in Section 2.1. The derivation for the convolution matrices is given in Ref. [25]. This convolution operator is absorbed into the material matrices. This can be seen in the following equations.

$$\begin{aligned} \sum_{q=-\infty}^{\infty} \sum_{r=-\infty}^{\infty} a_{m-q,n-r} S_{x,q,r}(\tilde{z}) &\rightarrow \epsilon_r^{m,n} * S_{x,m,n} \rightarrow \epsilon_r \mathbf{s}_x \\ \sum_{q=-\infty}^{\infty} \sum_{r=-\infty}^{\infty} a_{m-q,n-r} S_{y,q,r}(\tilde{z}) &\rightarrow \epsilon_r^{m,n} * S_{y,m,n} \rightarrow \epsilon_r \mathbf{s}_y \\ \sum_{q=-\infty}^{\infty} \sum_{r=-\infty}^{\infty} a_{m-q,n-r} S_{z,q,r}(\tilde{z}) &\rightarrow \epsilon_r^{m,n} * S_{z,m,n} \rightarrow \epsilon_r \mathbf{s}_z \end{aligned} \quad (1.5.12)$$

$$\begin{aligned} \sum_{q=-\infty}^{\infty} \sum_{r=-\infty}^{\infty} b_{m-q,n-r} U_{x,q,r}(\tilde{z}) &\rightarrow \mu_r^{m,n} * U_{x,m,n} \rightarrow \mu_r \mathbf{u}_x \\ \sum_{q=-\infty}^{\infty} \sum_{r=-\infty}^{\infty} b_{m-q,n-r} U_{y,q,r}(\tilde{z}) &\rightarrow \mu_r^{m,n} * U_{y,m,n} \rightarrow \mu_r \mathbf{u}_y \\ \sum_{q=-\infty}^{\infty} \sum_{r=-\infty}^{\infty} b_{m-q,n-r} U_{z,q,r}(\tilde{z}) &\rightarrow \mu_r^{m,n} * U_{z,m,n} \rightarrow \mu_r \mathbf{u}_z \end{aligned} \quad (1.5.13)$$

Eqs (1.5.10) - (1.5.13) are substituted into Eqs. (1.5.8) and (1.5.9) generalizing it for all the spatial harmonics in the layer.

$$\begin{aligned}
-j\mathbf{K}_y \mathbf{u}_z - \frac{d}{d\tilde{z}} \mathbf{u}_y &= \boldsymbol{\varepsilon}_r \mathbf{s}_x \\
\frac{d}{d\tilde{z}} \mathbf{u}_x + j\mathbf{K}_x \mathbf{u}_z &= \boldsymbol{\varepsilon}_r \mathbf{s}_y
\end{aligned} \tag{1.5.14}$$

$$\mathbf{K}_x \mathbf{u}_y - \mathbf{K}_y \mathbf{u}_x = j\boldsymbol{\varepsilon}_r \mathbf{s}_z$$

$$\begin{aligned}
-j\mathbf{K}_y \mathbf{s}_z - \frac{d}{d\tilde{z}} \mathbf{s}_y &= \boldsymbol{\mu}_r \mathbf{u}_x \\
\frac{d}{d\tilde{z}} \mathbf{s}_x + j\mathbf{K}_x \mathbf{s}_z &= \boldsymbol{\mu}_r \mathbf{u}_y \\
\mathbf{K}_x \mathbf{s}_y - \mathbf{K}_y \mathbf{s}_x &= j\boldsymbol{\mu}_r \mathbf{u}_z
\end{aligned} \tag{1.5.15}$$

Using the MOL method outlined in Section 2.2, Eqs. (1.5.14) and (1.5.15) are written in block matrix form with the longitudinal components.

$$\begin{aligned}
\frac{d}{d\tilde{z}} \begin{bmatrix} \mathbf{s}_x \\ \mathbf{s}_y \end{bmatrix} &= \mathbf{P} \begin{bmatrix} \mathbf{u}_x \\ \mathbf{u}_y \end{bmatrix} \\
\mathbf{P} &= \begin{bmatrix} \mathbf{K}_x \boldsymbol{\varepsilon}_r^{-1} \mathbf{K}_y & \boldsymbol{\mu}_r - \mathbf{K}_x \boldsymbol{\varepsilon}_r^{-1} \mathbf{K}_x \\ \mathbf{K}_y \boldsymbol{\varepsilon}_r^{-1} \mathbf{K}_x - \boldsymbol{\mu}_r & -\mathbf{K}_y \boldsymbol{\varepsilon}_r^{-1} \mathbf{K}_x \end{bmatrix}
\end{aligned} \tag{1.5.16}$$

$$\begin{aligned}
\frac{d}{d\tilde{z}} \begin{bmatrix} \mathbf{u}_x \\ \mathbf{u}_y \end{bmatrix} &= \mathbf{Q} \begin{bmatrix} \mathbf{s}_x \\ \mathbf{s}_y \end{bmatrix} \\
\mathbf{Q} &= \begin{bmatrix} \mathbf{K}_x \boldsymbol{\mu}_r^{-1} \mathbf{K}_y & \boldsymbol{\varepsilon}_r - \mathbf{K}_x \boldsymbol{\mu}_r^{-1} \mathbf{K}_x \\ \mathbf{K}_y \boldsymbol{\mu}_r^{-1} \mathbf{K}_x - \boldsymbol{\varepsilon}_r & -\mathbf{K}_y \boldsymbol{\mu}_r^{-1} \mathbf{K}_x \end{bmatrix}
\end{aligned} \tag{1.5.17}$$

From here we can derive a wave equation exactly like the wave equation Section 2.2 leading to the following:

$$\frac{d^2}{d\tilde{z}^2} \begin{bmatrix} \mathbf{s}_x \\ \mathbf{s}_y \end{bmatrix} = \mathbf{PQ} \frac{d}{d\tilde{z}} \begin{bmatrix} \mathbf{s}_x \\ \mathbf{s}_y \end{bmatrix} \tag{1.5.18}$$

At this point, the exact same steps described in Eqs. (1.4.18) - (1.4.55) are followed to calculate the total power reflected and transmitted through the device. The only change is Eq. (1.4.50) is omitted since the fields are already in Fourier space.

The RCWA method is a very powerful tool for designing and analyzing all-dielectric FSSs. It provides a fully rigorous solution to Maxwell's equation and its semi-analytical formulation makes it a very fast fully 3D model that doesn't take as much computation power as other methods. Though powerful, it does have its drawbacks. One of these drawbacks is that it scales very poorly in the transverse directions. This makes simulations of devices with very fine features slow. Drawback number two is that this method becomes very slow for devices with high dielectric contrasts. This is due to its formulation in Fourier space and Gibbs phenomenon [55]. Gibbs phenomenon is due to the finite number of spatial harmonics used in the formulation. Another drawback is that field visualizations are very cumbersome to implement. This problem is made more apparent when compared to ease of field visualizations with the FDFD and FDTD methods. The last drawback this method has is that it isn't formulated to model non-periodic devices. The formulation can be rederived to account for non-periodicity, but this adds complexity and there are better methods out there, FDTD, for the analysis of large non-periodic devices.

## Chapter 3: Numerical Optimization Techniques

In this chapter two different numerical optimization techniques are formulated and described. These optimization techniques are very powerful tools for the design of FSSs. The techniques described are stochastic search algorithms that allow the search of vast multi-dimensional solution spaces effectively and efficiently. This allows for the development of novel devices that have complex geometries and customized spectra for whatever application is needed.

The optimization techniques discussed in this chapter suffer from the problem that all heuristic search algorithms face, the problem of getting stuck on a local best solution. At the end of the formulation of each optimization algorithm, techniques are given to minimize this problem.

### 3.1 Introduction to FSS optimization

Before a heuristic optimization method can be formulated and described, the concept of optimization for FSSs must be explained. For most FSSs, the reflectance, transmittance, fractional bandwidth, and field-of-view of the device are the most important metrics of operation. This is especially true for all-dielectric FSSs, as their fractional bandwidth is very small. These are the values that generally need to be maximized or minimized depending on application. How these values relate to one another determine how “good” a device is. This “good” value must be quantified to a single number that tells how well the device is working to expected parameters. This quantifying of the “good” value is called the merit function, also known as the fitness function, of the device [56]. These merit functions are what allow the optimization to know when the design has achieved its performance metric and to stop. When formulating an optimization for FSSs, one must consider what is wanted out of the optimization and design a merit function that will calculate this.

Another aspect to be aware of when formulating an optimization is the size of the solution space. When designing these FSSs, they can have many different variables of adjustment because the physics behind their operation primarily relies on geometry. Period size, different shapes, substrate thickness, and different materials are just an example of the different things that can be

simultaneously optimized. When running an optimization, each variable of adjustment adds a dimension to the solution space.

The solution space is composed of all the devices that the variables of adjustment allow to exist. A simple example of this has been created to illustrate these concepts.

In this example an all-dielectric FSS with two variables of adjustment will be used. The variables are the height of the grating,  $d$ , and the width of the grating,  $f$ . These two variables produces a simple 2D solution space. Within this solution space are all the devices that make up the variable grating height and width.

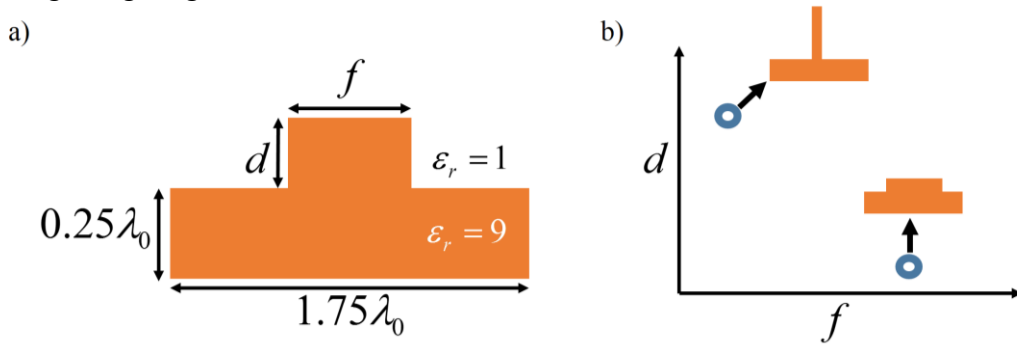


Figure 3.1: Example all-dielectric FSS with two variables of adjustment and solution space. a) shows the device with a variables grating height and width. b) shows the 2D solution space made from the adjustment variables.

Since this device has such simple geometry and only two variables of adjustment, a brute force optimization can be done by performing full parameter sweeps of the two variables of adjustment. Once this is complete, the device with the required parameters can be extracted by formulating a simple merit function.

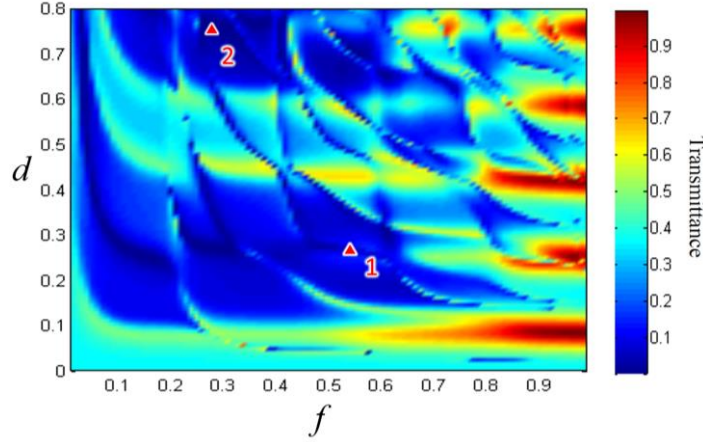


Figure 3.2: Solution space of example all-dielectric FSS. The 1<sup>st</sup> triangle shows the point in the solution space that has smallest transmittance value, while the 2<sup>nd</sup> triangle shows a adjusted merit function to include more resilience from manufacturing defects.

The merit function in this example will be the smallest amount of transmittance possible. In this case the merit function equals the minimum transmittance. This is point 1 in Figure 3.2.

$$M(f, d) = \min(TRN) \quad (1.5.19)$$

This point, while it has the smallest transmittance, might not actually be the best device. If this device was being made for very high frequency, manufacturing defects and inconsistencies become more relevant due to the smaller features. The spot that is currently calculated has a very small window of error that it can tolerate without drastically changing the spectra. The merit function needs to be adjusted to find a spot with more leeway in the dimensions while still providing the best reduction in transmittance it can.

$$M(f, d) = |\min(TRN) \Delta f \Delta d| \quad (1.5.20)$$

Applying this merit function to the solution space finds point 2 in Figure 3.2. At point 2 it can be seen that the device has a broader suppression minima. This allows the device to be more resilient to manufacturing defects.

This in essence is the entire point of developing these optimization algorithms for FSSs. To find the best design in the solution space that is specified by the merit function. It can be seen

how when more complexity, more variables of adjustment, are added to the optimization, it would become unpractical to perform a brute force full parameter sweep. This is especially true for devices with large complex geometries that have long simulation times. For these types of methods, heuristic algorithms need to be employed and the solution space just searched and not fully solved.

### 3.2 Particle swarm optimization

Particle swarm optimization (PSO) is an iterative optimization algorithm that uses the movement and intelligence of swarms to search a given solution space [56]. In this type of optimization, a swarm of particles are dispersed stochastically throughout the solution space. Each particle is a device that is simulated and has its own random velocity and direction associated with it.

An example of these randomly placed particles in a 2D solution space can be seen in Figure 3.3. In this figure it can be seen that each particle has an associated vector component attached to it.

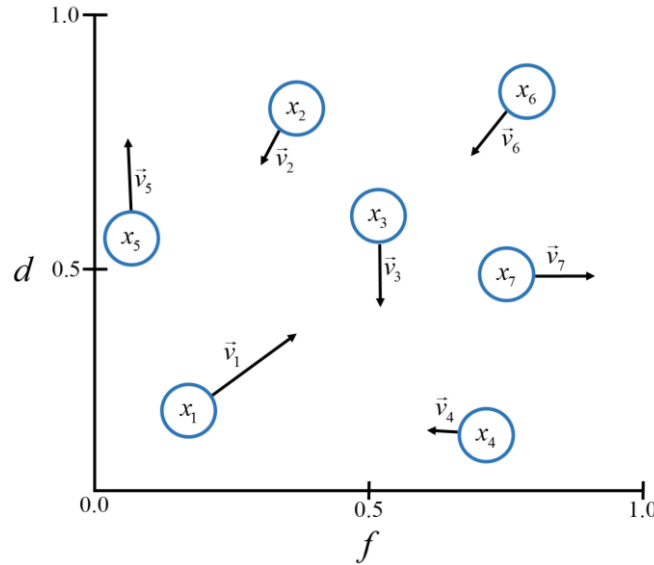


Figure 3.3: PSO particles randomly placed in a 2D solution space. Each particle has its own direction and velocity associated to it.

After simulating each device, a merit function is applied to each spectra to determine how well the spectra of the device matches the spectra required. The merit function values are then

compared and the best one, the global best, is selected. The position of the global best particle is then shared amongst all the other particles. With this information, they change their direction vectors and start moving toward the best particle over the next iterations. As they are moving toward the best particle they scan the solution space along the way. If a new global best position is discovered, this particle becomes the global best and all the other particles change their direction vectors and start heading toward this new point, scanning along the way. This particle swarming behavior is controlled using the particle swarm velocity update equation [36]. This equation is updated every iteration and changes the direction that the particles are moving.

$$v_{i+1}^k = \underbrace{wv_i^k}_{\text{inertia term}} + \underbrace{cr_1^k(p_i - x_i^k)}_{\text{cognitive term}} + \underbrace{sr_2^k(p_g - x_i^k)}_{\text{social term}} \quad (1.6.1)$$

In this equation, the  $v_i^k$  variable is the velocity of the  $i^{\text{th}}$  particle of the  $k^{\text{th}}$  iteration, the  $x_i^k$  variable is the position of the  $i^{\text{th}}$  particle of the  $k^{\text{th}}$  iteration, the  $p_i$  variable is the position of the best solution seen by the  $i^{\text{th}}$  particle and the  $p_g$  variable is the position of the global best solution. There are three other terms that operate on these variables that control the behavior of the particles.

The first term that controls the particle's behavior is the inertia term. This term controls how fast a particle can change direction. The  $w$  in the inertia term can be adjusted to force the particles to scan more of the solution space. The smaller the coefficient  $w$  is, the sharper that the particle can turn, while a larger  $w$  coefficient will make the particle take a wider, sweeping turns. Figure 3.4 shows the behavior of the particle when the inertia term is adjusted. In portion a) of Figure 3.4 the path of a particle with a small inertia coefficient can be seen. This leads to sharp curve and abrupt change in direction toward the global best. The second portion of Figure 3.3., b), shows the effect of a large inertia coefficient. The large inertia coefficient lead to a larger turn radius, scanning more of the solution space along the way.

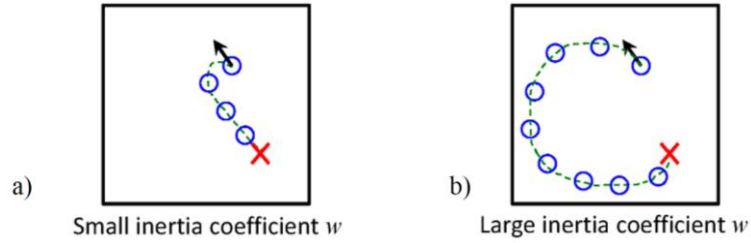


Figure 3.4: Illustration of the inertia term. a) shows the behavior of the particle with a small  $w$  coefficient. b) shows the behavior of the particle with a large  $w$  coefficient.

The second term of the velocity equation is the cognitive term. This term controls how willing the particle is to move toward the global best, or to go back to the best solution it has personally found. There is a random number coefficient,  $r_1^k$ , associated with this term. This random number coefficient forces the particle to meander instead of going in a straight line. In figure 3.5 the different effects are shown of scaling the random number coefficient and the cognitive coefficient have on the particle. The a) portion of Figure 3.5 shows that when both the random number and cognitive coefficient are small the particle moves away from the global best slowly and in odd directions. In the b) portion of Figure 3.5 the random number coefficient is larger than the cognitive. This leads to a much more irregular pattern of movement away from the global best. Portion c) of Figure 3.5 shows the behavior of the particle with a cognitive coefficient larger than the random number. The particle in this situation moves in a almost straight line away from the global best. The final portion, d), of Figure 3.5 shows what happens when both the random number and cognitive coefficient are large. The particle tends to slightly meander while heading in a direction away from the global best.

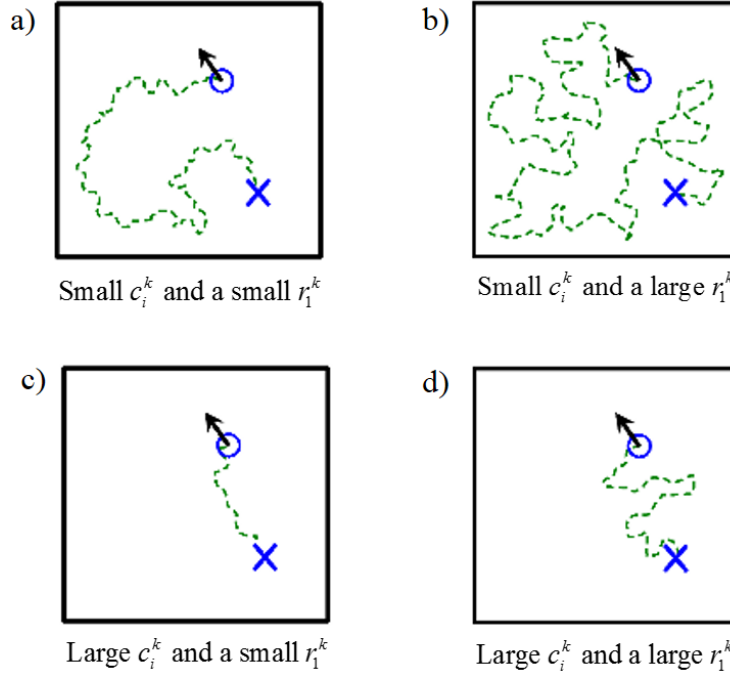


Figure 3.5: Illustration of the cognitive term. This figure shows the behavior of the particle when the different coefficients are scaled differently.

When designing a PSO, it is important to remember that each particle can have its own cognitive term associated with it. This allows for certain particles to continue to scout around the solution space while the rest of the swarm homes in on a design. Doing this can help find better global best design to go to if all the particles get stuck on a local solution.

The final term in the PSO velocity update equation is the social term. This term controls the tendency of the particles to go toward the global best. Like the cognitive term, this term has a random number coefficient,  $r_2^k$ , associated with it. This random number coefficient like the cognitive term controls how much the particle meanders toward the global best.

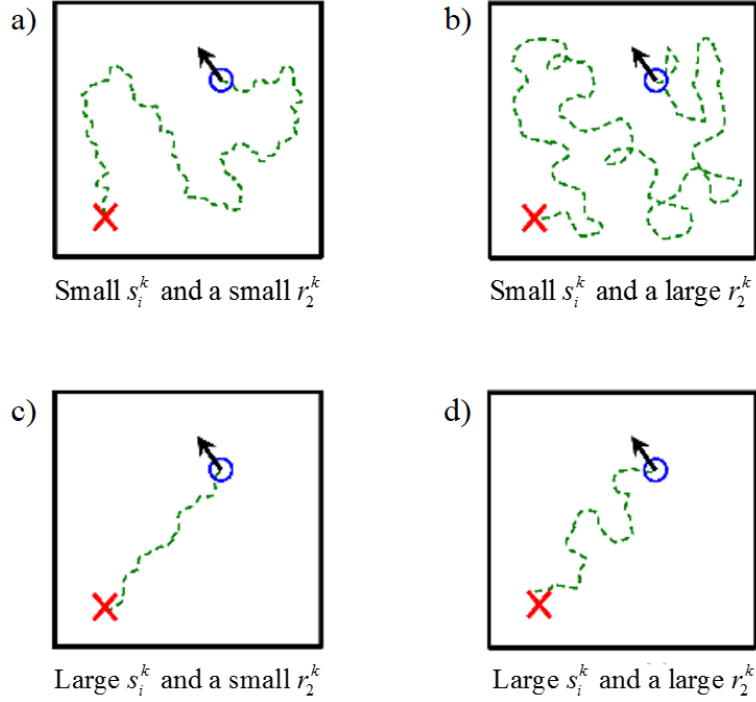


Figure 3.6: Illustration of the social term. This figure shows the behavior of the particle when the different social coefficients are scaled differently.

The random number coefficient forces the particle to meander instead of going in a straight line. In figure 3.6 the different effects are shown of scaling the random number coefficient and the social coefficient have on the particle. The a) portion of Figure 3.6 shows that when both the random number and social coefficient are small the particle moves toward the global best slowly and in odd directions. In the b) portion of Figure 3.6 the random number coefficient is larger than the social. This leads to a much more irregular pattern of movement toward the global best. Portion c) of Figure 3.6 shows the behavior of the particle with a social coefficient is larger than the random number. The particle in this situation moves in a almost straight line toward the global best. The final portion, d), of Figure 3.6 shows what happens when both the random number and social coefficient are large. The particle tends to slightly meander while heading in a direction toward the global best.

Using the velocity update equation described every iteration of the particles movement provides the swarming nature. These swarming particles search the solution space, finding the

best solution. As with any heuristic algorithm, the risk of getting stuck in a local best is a very real possibility.

To minimize this risk, certain particles can have adjusted social and cognitive terms. This would allow said particles to roam the solution space searching, while the rest of the swarm homes in on a solution. These particles can even be made to be put in “communities” and “tribes” with different values of the coefficients and computations taken into account [57]. Many, many studies have been devoted PSO intelligence and behavior [58]. For the devices developed in this work, a very simple adaption of these ideas was used.

PSO is a very powerful optimization algorithm that is very good for searching large solution spaces, that one doesn't know what form they take. It is this author's opinion that this optimization algorithm is best implemented for optimization of variables with continuous number sets, as in the cases of designing the geometry of FSSs. For optimizations with a more binary nature there is a better algorithm to be used which is discussed next.

### **3.3 Genetic algorithm optimization**

A genetic algorithm optimization (GAO) is a heuristic optimization algorithm that scans the solution space using evolutionary theory [55]-[56]. In this type of optimization for FSSs, each design is known as a “phenotype”. Inside this phenotype, resides the “chromosomes” which are the variables of adjustment that are being stochastically generated to create the different phenotypes in the solution space. Each phenotype is simulated and the merit function is calculated from the resulting frequency and FOV sweeps. The merit function, also known as the fitness function, is a single number that quantifies how “good” a candidate design is. This can be challenging, especially when there are multiple constraints of varying relative importance dictating the quality of the design. The merit function formulation and analysis for this optimization is the same as was used in Ref. **Error! Reference source not found.** Using the merit function values generated, the best two phenotypes, the “mother” and “father”, are selected. These phenotypes are

then “bred” together and “children” phenotypes are spawned. The formula used to spawn the children takes on the following form:

$$\mathbf{C}_i^g = \mathbf{F}_i \cdot \mathbf{D}^g + (1 - \mathbf{F}_i) \mathbf{M}^g \quad (1.6.2)$$

In Eq. (1.6.2)  $\mathbf{C}_i^g$  refers the  $i^{\text{th}}$  child of the  $g^{\text{th}}$  generation,  $\mathbf{D}^g$  is the father phenotype of the  $g^{\text{th}}$  generation, and  $\mathbf{M}^g$  is the mother phenotype of this same generation. The  $\mathbf{F}_i$  term in this equation is what controls the manipulation of the chromosomes. It operates on the mother and father phenotypes to generate children phenotypes. In this work the  $\mathbf{F}_i$  term is a randomly generated array the same size as the phenotypes. This term is generated for each individual child, providing each child with a different  $\mathbf{F}_i$  operation. Doing this ensures each child is spawned differently. This allows more of the solution space to be explored and provides the necessary variance to keep evolving new designs to avoid being stuck at a local best solution.

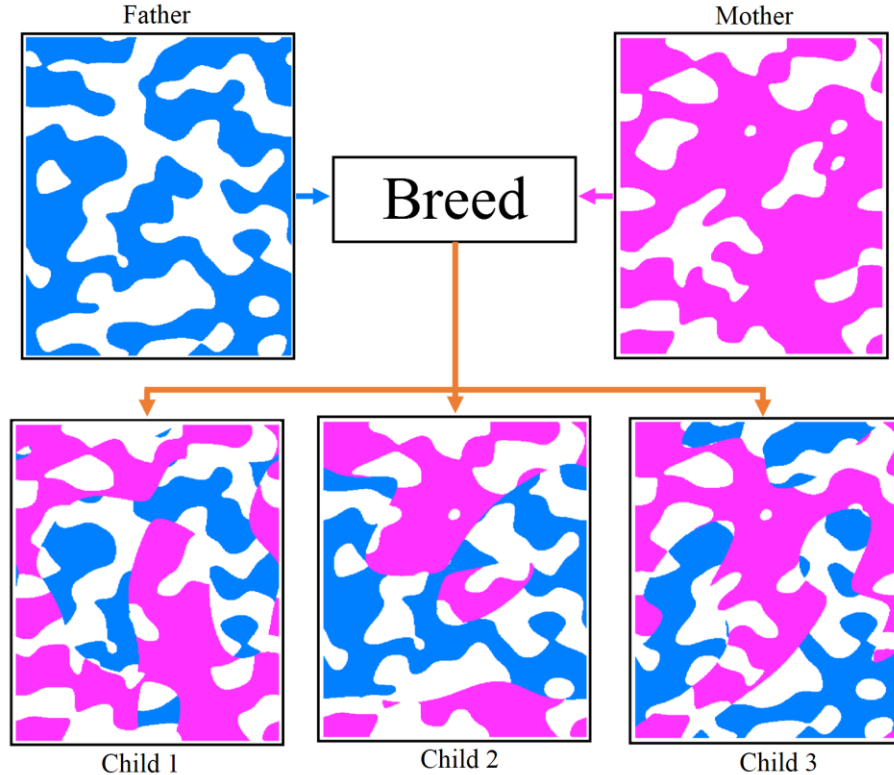


Figure 3.7: Illustration of the GAO method. In this figure the breeding between two phenotypes using the described breeding function can be seen. In this example the two phenotypes produced three children with varying amounts of variance.

The children generated this way have aspects of both the father and mother phenotype with added variance. An example of this can be seen in Figure 3.7. By varying the amount of variance in the breeding function can help with the problems that arise from getting stuck at a local best solution. This is a problem that arises in all stochastic optimization algorithms. It occurs when the optimization converges on a local best solution and no longer scans the solution space. While this problem can't be 100% avoided, certain techniques can be employed to minimize the chance this problem occurs. One of these techniques is to build in enough randomness into the optimization that even if it gets stuck, it will continue to explore new designs and scan other regions of the solution space. Another, technique used in this optimization to combat the local best problem was the introduction of “illegitimate children” phenotypes. By introducing the illegitimate children into the optimization allows “mutations” to be introduced. Mutations are chromosomes that the neither the mother nor the father have. These mutations ensure that the design will keep evolving. The illegitimate child phenotype is a child generated with a random phenotype bred to one of the parents. Figure 3.8 shows this.

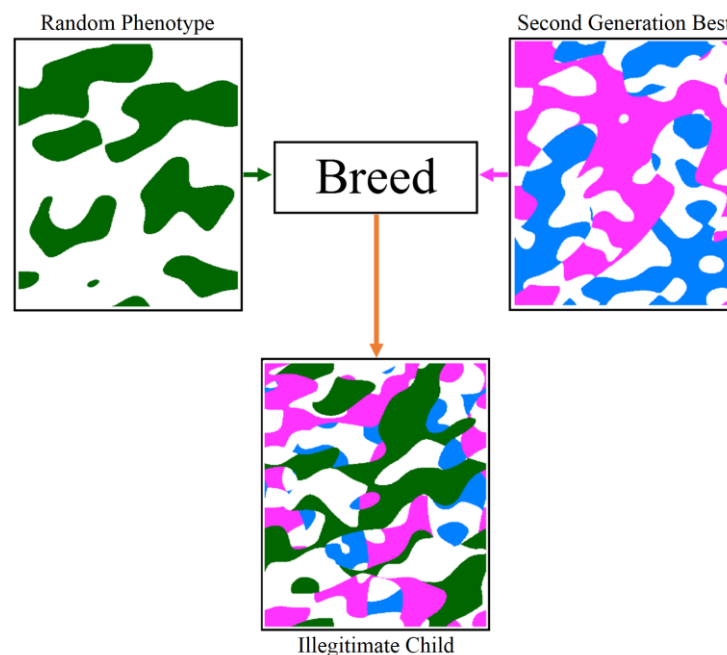


Figure 3.8: Illegitimate child phenotype generation.

The GAO method is a very powerful stochastic optimization technique that works very well for binary type problems as can be seen in Figure 3.7. This method like PSO has been studied extensively [61]. Whole communities can be created in the solution space and then interbred stochastically searching more of the solution space. For the devices developed in this work, a very simple adaption of these ideas was used with only one family. This method runs into the same problem as all of the other stochastic optimization techniques, in getting stuck in local best. This problem can be helped by introducing fresh phenotypes and mutations into the overall families being generated.

The heuristic optimization methods described within this work, are very useful in the development of FSSs. They provide a way to search the given solution spaces effectively and efficiently. These methods run into the same problem as all stochastic search methods do. That is the problem of getting stuck in a local best. The only way to absolutely know if the answer is the best solution is to perform a complete parameter sweep on all the variables of adjustment. In some cases the solution spaces for these devices are so big, this would take centuries of computation time. There are different techniques to help overcome this problem but one is never sure of absolute global best. Since the optimization techniques in this work are being developed to solve engineering problems, as long as the problem is solved it doesn't matter if it is the global best of the entire solution space.

Another aspect to these heuristic algorithms that needs to be addressed is that a stop condition must be implemented. This stop condition is implemented by checking the delta between the current spectra and the spectra that is wanted. If this delta is sufficiently low, the program is stopped. This is done so the program stops running instead of simulating the same device over and over again, wasting computing power.

## **Chapter 4: All-Dielectric FSS with Exiguous Periods**

All-dielectric frequency selective surfaces (FSSs) can serve as an alternative to their metallic counterparts when they must operate at very high power, loss must be minimized, or when the surface itself must be low observable. When metals are avoided, there is a weaker interaction with electromagnetic waves and it becomes more difficult to achieve strong suppression in the stop band while also realizing compact size, wide field-of-view or broadband operation. One attractive approach utilizes guided-mode resonance (GMR) as the filtering mechanism, but this phenomenon exhibits several drawbacks that must be overcome for practical application at radio frequencies. One of the major drawback for the device is the number of periods needed for this type of FSS to work effectively.

In this chapter, a method is developed to dramatically reduce the number of periods needed for this device work effectively. This device was optimized, manufactured and tested, proving the validity of the method described.

### **4.1 Device introduction**

The all-dielectric FSS described in this work is the combination of two simple devices; a grating and a slab waveguide that are electromagnetically coupled through a phenomenon known as guided-mode resonance (GMR) [20]-[22]. This simple combination makes the device highly compact and easy to build. When precise phase matching conditions are met, an external wave incident on the device is diffracted by the grating and partially coupled into guided-modes within the slab. As long as the guided-modes overlap the grating, they slowly leak from the slab over some distance due to reciprocity. The outcoupled wave interferes with the applied wave to produce an overall frequency response. These all-dielectric FSSs can produce very strong suppression using just a single subwavelength dielectric layer with low dielectric contrast.

These all-dielectric FSSs are almost always designed assuming that the grating is infinitely periodic. Due to the physics of guided-mode resonance, devices must often be hundreds of grating

periods long to approach the performance of the infinitely periodic structure [27]. At radio frequencies, this often leads to prohibitively large devices that are dozens of meters in length.

The work in this chapter describes a procedure to overcome this size limitation. It was used to design a simple narrowband all-dielectric FSS operating at 1.5 GHz that would normally require over 200 grating periods to operate. The device was designed to operate at normal incidence and with the electric field polarized parallel to the grating grooves. Using the technique described in this chapter, the all-dielectric FSS provided strong suppression in the stop band using just seven grating periods. This represents a nearly 30x reduction in size. It is important to note that the device presented here is narrow band and has a narrow FOV. The bandwidth and FOV can be dramatically extended through more sophisticated grating designs [62] and **Error! eference source not found.**, but these topics will not be discussed here.

## 4.2 Baseline device design

Work began by choosing a frequency and material system. A frequency of 1.5 GHz was chosen because it was a sufficiently low frequency to demonstrate the concept while keeping the physical dimensions of the device reasonable for easy manufacturing and handling in an anechoic chamber.

High density polyethylene (HDPE) was chosen as the dielectric material because it is inexpensive, easily machined, and has a low loss tangent. The dielectric constant was specified by the vender to be  $2.35 \pm 10\%$ . Despite this uncertainty, the design was performed using 2.35 as the dielectric constant.

Given the frequency and material system, a simple three step procedure was used to design a monolithic all-dielectric FSS using GMR. This was considered to be the baseline design because it was designed as an infinitely periodic device. The procedure is illustrated in Figure 4.1.

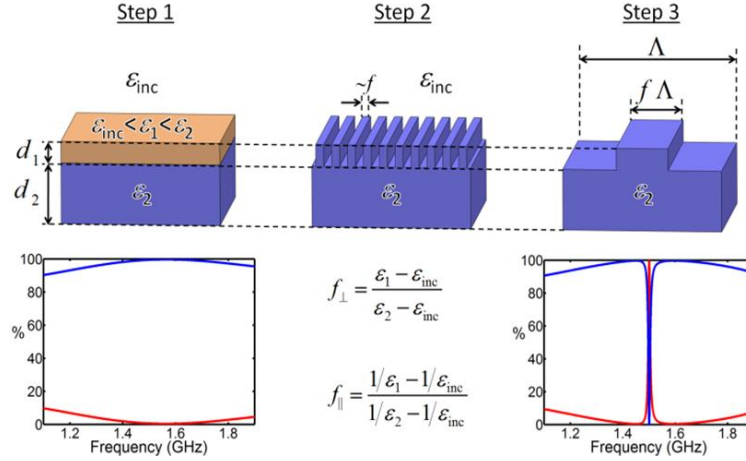


Figure 4.1: Three step design procedure for an infinitely periodic all-dielectric FSS

The first step was to design a two layer structure that provided a low background reflection across the band of interest. Here, each layer was assumed to be homogeneous. To eventually design an all-dielectric FSS that was to be monolithic, the dielectric constant in the top layer  $\epsilon_1$  was constrained to fall between the dielectric constant of the surrounding material (air) and the dielectric constant of the HDPE,  $1.0 < \epsilon_1 < 2.35$ . A transfer matrix method [63] was used to model transmission through the two layer dielectric stack. A least squares optimization method [39] was then implemented in MATLAB to determine the values of  $\epsilon_1$ ,  $d_1$ , and  $d_2$  that minimized the background reflection for a wave at normal incidence. These were found to be  $\epsilon_1 = 1.1$ ,  $d_1 = 1.999$  cm,  $d_2 = 5.588$  cm.

The second step was to realize  $\epsilon_1$  in the top layer using a grating with the correct duty cycle. This was accomplished using effective medium theory [64] that relates the duty cycle  $f$  of the grating to the effective dielectric constant for a normally incident wave. For one-dimensional gratings, two polarizations are possible so there are separate equations for calculating the duty cycle necessary to realize the needed effective dielectric constant. These are summarized in Eqs. (2.2.1) and (2.2.2).

$$\epsilon_1 = f_{\perp} \epsilon_2 + (1 - f_{\perp}) \epsilon_{\text{inc}} \quad (2.2.1)$$

$$\frac{1}{\varepsilon_1} = \frac{f_{\parallel}}{\varepsilon_2} + \frac{1-f_1}{\varepsilon_{\text{inc}}} \quad (2.2.2)$$

The design described here had the electric field polarized parallel to the grooves so Eq. (2.2.1) was used.  $f_{\perp}$  was calculated to be 32.6%.

The third step was to adjust the grating period until a guided-mode resonance was placed at the desired frequency. To aid in this step, an initial guess at the grating period can be taken from Figure 1.6 as  $\Lambda = 0.8\lambda_0$ . Rigorous coupled-wave analysis [53] was used to tune the grating period until the resonance fell exactly on 1.5 GHz. This was found to be  $\Lambda = 15.34$  cm. The final design, along with the simulated transmittance and reflectance, is provided in Figure 4.2.

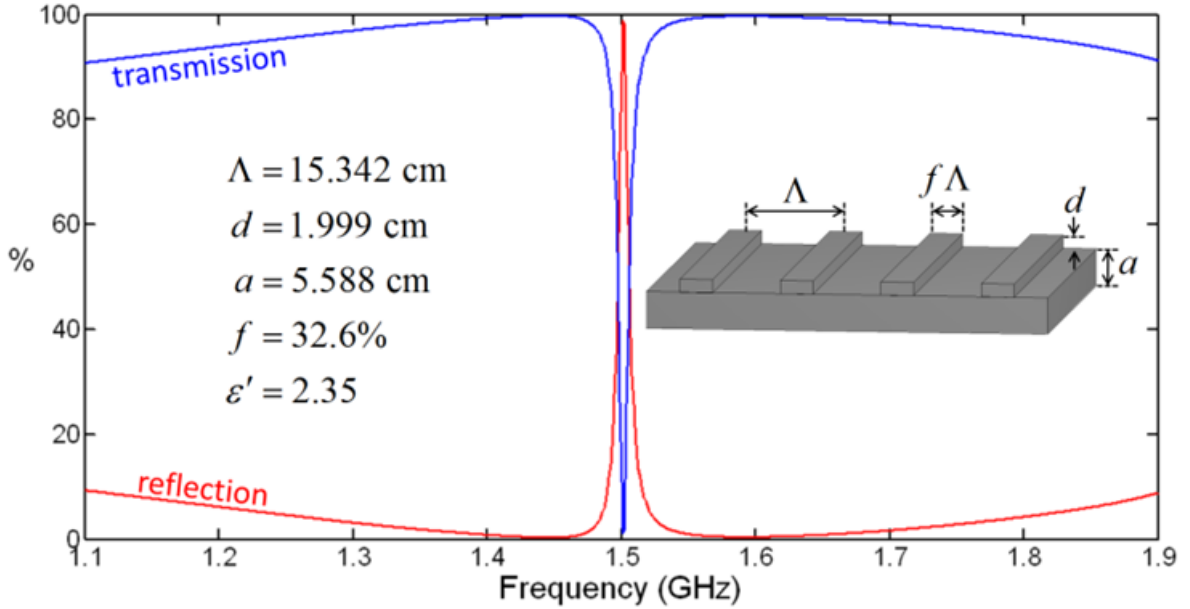


Figure 4.2: Baseline all-dielectric FSS design and its simulated performance.

#### 4.3 Effect of finite length

No physical device can be made infinitely periodic. Real devices must be constructed using only a finite number of grating periods. For low contrast all-dielectric FSSs, it often takes hundreds of grating periods for a guided-mode to leak from the slab waveguide. Similarly, an applied wave must overlap hundreds of grating periods to excite a sufficiently strong guided-mode so as to produce a strong resonance condition. This means that for a real device to approach the

performance of the infinitely periodic device, it must be composed of hundreds of grating periods [27].

To quantify this, a series of simulations was performed using the finite-difference frequency-domain (FDFD) method [20]. These simulations started with the baseline all-dielectric FSS and simulated finite length devices with an increasing number of grating periods. The results are provided in Figure 4.3. From this data, it can be observed that real devices will exhibit increased ripple with weakened and broadened resonance relative to the infinitely periodic device. For the baseline all-dielectric FSS, it can be concluded that at least 200 periods are needed for a sufficiently strong frequency response.

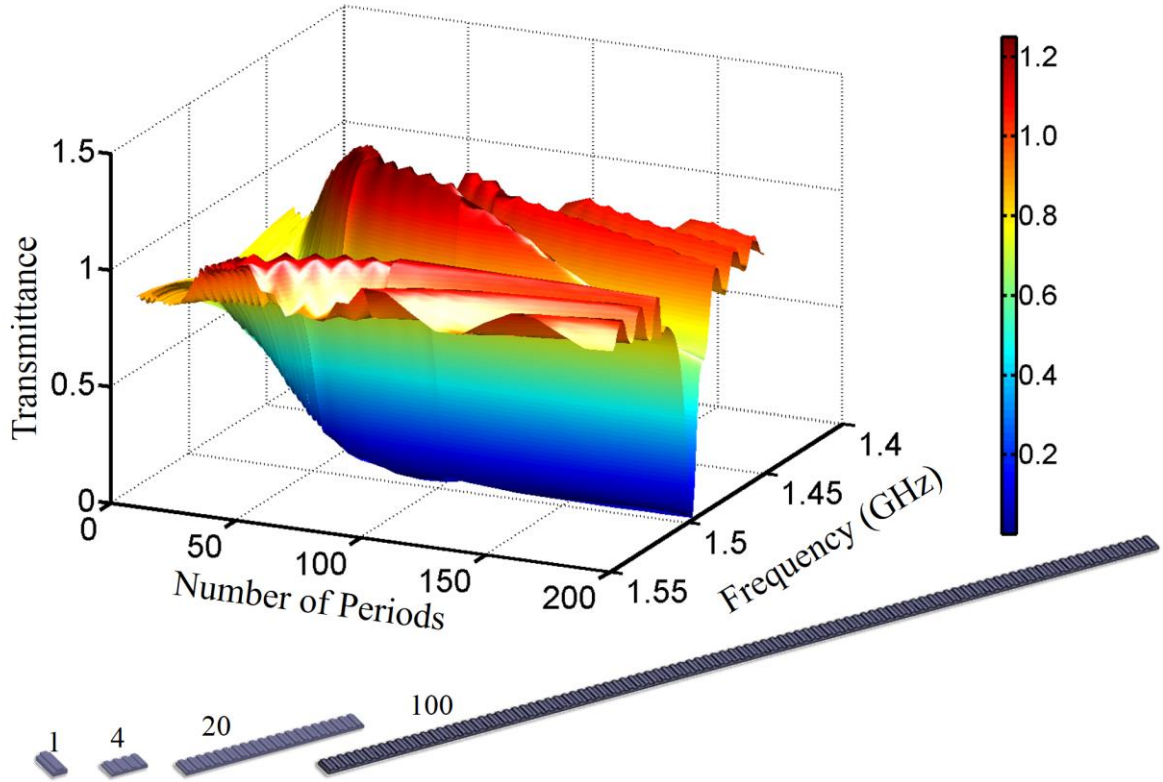


Figure 4.3: Response of a all-dielectric FSS with varying number of periods.

#### 4.4 Design approach

To date, almost all implementations of all-dielectric FSSs have been at optical frequencies where accommodating a large number of grating periods is not a problem. At radio frequencies, however, this results in prohibitively large devices. Two hundred periods of the baseline FSS is over 30 m in length. Clearly, for practical implementation at radio frequencies a solution to this is needed. In fact, it was necessary to find a method capable of producing a strong frequency response using an all-dielectric FSS with just five to ten periods.

Some preliminary investigations focused on using anti-reflective terminations at the end of the slab. Ultimately this did not work because a sufficiently strong guided-mode was never excited. This is a necessary condition that ensures the out-coupled waves have sufficient amplitude to completely interfere with the applied wave. The technique that was ultimately successful was terminating the slab waveguide with reflective ends.

With reflective ends, the device effectively “unfolds” into an infinitely periodic device. At the start, it was hypothesized that the round trip phase of the guided-mode in the slab should be an integer multiple of  $2\pi$  to prevent the mode from interfering with itself and scattering out of the slab. To match this condition to the designed resonant frequency, spacer regions were added to the ends of the slab that could be adjusted in length. The conceptual construction of the device is illustrated in Figure 4.4.

To study this device and produce a design, a double parameter sweep was performed showing transmittance as a function of frequency and spacer length. The results are shown in Figure 4.5. It was initially anticipated that the device response would be erratic when the spacers were not tuned to the resonant frequency of the baseline GMR. It was surprising to observe a reasonably strong resonance for all spacer lengths. This means that a device’s performance will be robust to errors incurred in the spacer length due to fabrication.

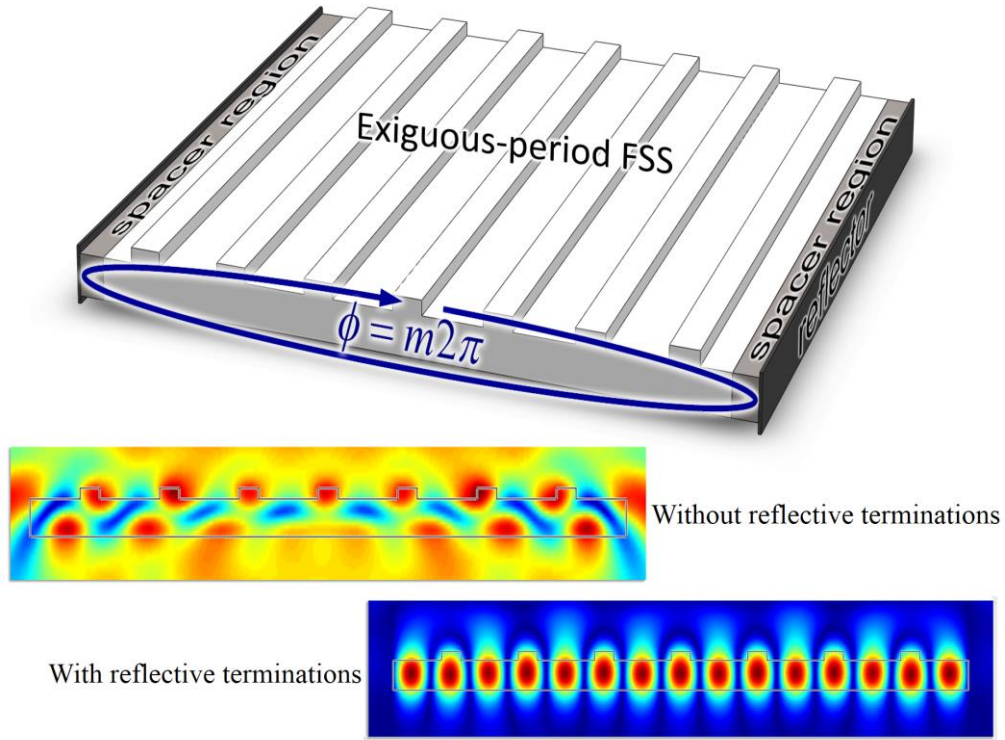


Figure 4.4: Construction and operational principal of a exiguous-period all-dielectric FSS.

The strongest suppression was observed at the point where the spacers were tuned to the same frequency as the baseline GMR confirming the original hypothesis, but the response away from these values was still very useful. Based on this analysis, the optimum length for the spacer regions was found to be

4.3 cm.

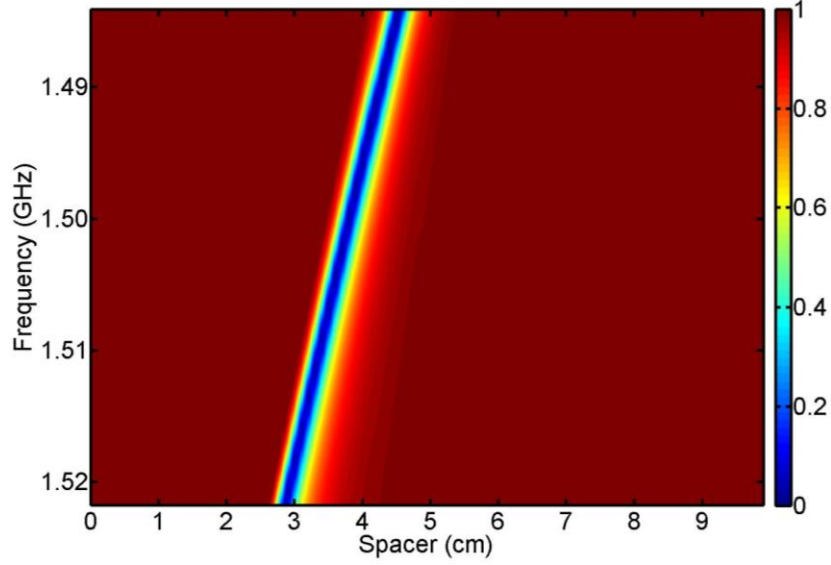


Figure 4.5: Double parameter sweep for a 7 period all-dielectric FSS.

From the data in Figure 4.5, it was discovered that the position of the resonance could actually be tuned through the length of the spacer regions. Devices with fewer periods provided the widest tuning range. Devices with more periods were less tunable and also exhibited multiple resonances corresponding to multiple resonant modes oscillating in the slab.

While not conveyed by this data, an approximately 3 dB improvement in suppression on resonance was observed for every grating period added to the FSS.

#### 4.5 Experimental Results

The final design of the device is shown in Figure 4.6. It had the same geometry as the baseline all-dielectric FSS, but included seven grating periods and two spacer regions on either end that were 4.3 cm in length. Two support frames were crafted in order to orient the all-dielectric FSS in a position allowing a vertically polarized field pattern to be parallel to the grooves in the all-dielectric FSS.

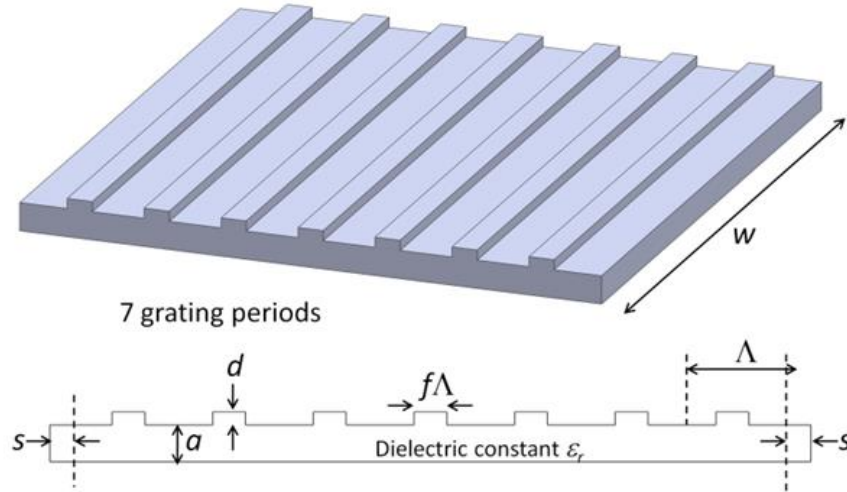


Figure 4.6: Final design of 7 period all-dielectric FSS

The first support frame consisted of two sides made of MDF sandwiched between sheet metal siding. The sheet metal siding was employed as the reflector panels.



Figure 4.7: All-dielectric FSS with mounted reflectors inside a anechoic chamber.

The second support frame contained no metal side walls. The GMR was inserted inside the support frame and placed on a table inside an anechoic chamber 30 inches in front of the receiver antenna as displayed in Figure 4.7.

The measurement setup consisted of two linearly polarized 15 dB gain horn antennas that operated across the 1.2 to 1.7 GHz band. These horns were oriented in the TM polarized orientation.

The transmitting horn antenna was connected to Port 1 of an Agilent 8720 Vector Network Analyzer (VNA) while the receiver horn antenna was connected to Port 2. The VNA was controlled via ORBIT software allowing the entire measurement to be computer controlled.

The anechoic chamber system was carefully calibrated prior to the insertion of the FSS in order to eliminate the effects of the table and the antenna support structures. The measurements were made over a frequency band of 1.4 to 1.6 GHz. The measured transmission results are provided in Figure 4.8.

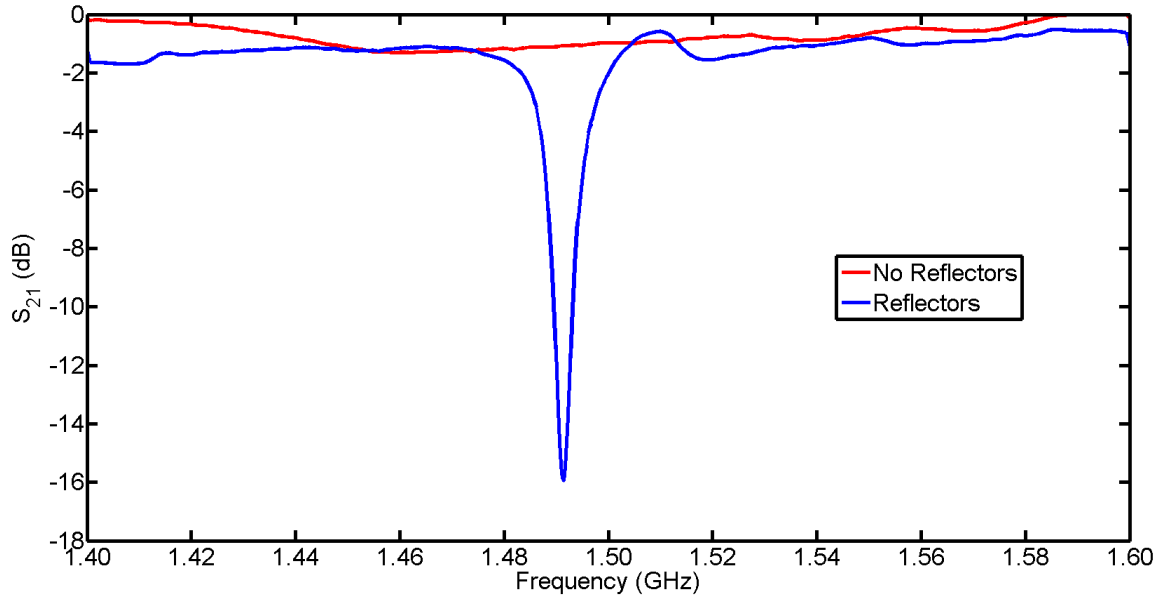


Figure 4.8: Measured transmittance with and without reflectors of the all-dielectric FSS.

As can be noted in the Figure 4.8, when the metal walls were present, a strong resonance occurred at 1.491 GHz. This resonance showed a suppression of -16.5 dB. However, when the metal walls were removed, no resonance was observed. This is very consistent with the simulated results discussed previously.

Figure 4.9 depicts the measured response along with the simulated response. From the figure it can be noted that the measured response shows a resonance at a slightly higher frequency in comparison to the simulated response. This frequency shift was attributed to fabrication error.

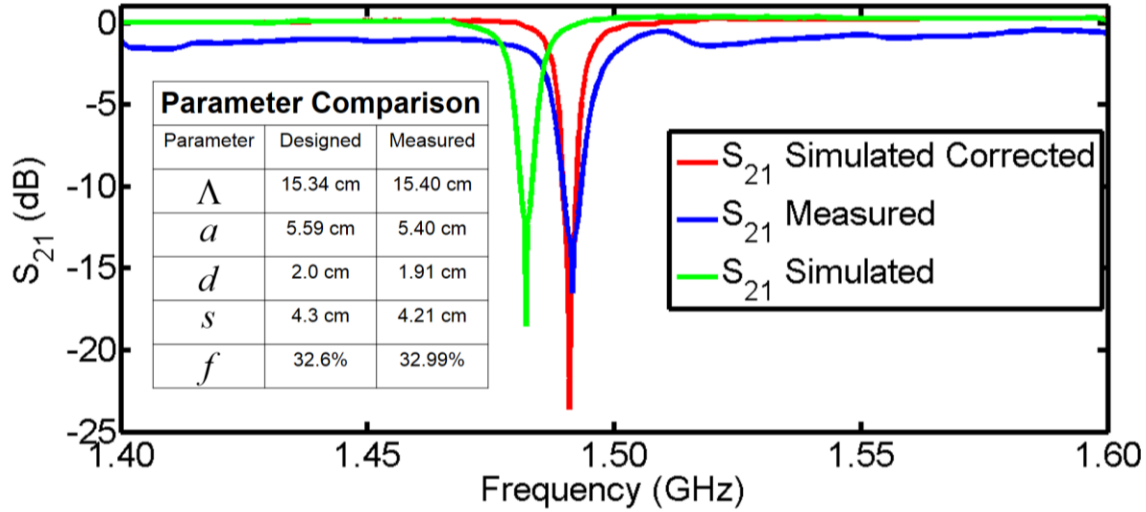


Figure 4.9 Measured transmittance and simulated spectra.

A FDFD model was developed and simulated with the measured dimensions of the manufactured FSS to quantify the change in the resonance frequency. This produced a spectra that matched the spectra of the experiment except that the model's spectra was less broad. The less broad spectra was accounted to the loss tangent not being implemented in the simulation material parameters. . By not including the loss tangent in this simulation, the simulated response maintained a 3 dB bandwidth of roughly 7 MHz. The measured device exhibited a 3dB bandwidth of roughly 12 MHz.

#### 4.6 Device conclusion

In conclusion, this work has shown that all-dielectric FSSs are an attractive alternative to metallic FSSs if the challenges with the number of periods needed can be overcome. They can provide a strong frequency response using just a simple dielectric structure. Typical all-dielectric FSSs, however, are required to be hundreds of wavelengths long to operate, but this is not practical at radio frequencies where the wavelength can be large. This chapter described a technique where

a seven period all-dielectric FSS was designed and tested and the performance approached that of the infinitely periodic device. The technique involved incorporating spacer regions and reflective terminations on the ends of the device. This work has led to a exiguous period device that solves this problem. The device described still uses metals and is a composite device. A better solution was sought to design devices that can survive extreme environments.

## Chapter 5: All-Dielectric FSS for HPM

In this chapter, an all-dielectric frequency selective surface was developed for high power microwaves. By avoiding the use of metals, arcing at field concentration points and heating in the conductors was avoided. To do this in a compact form factor while still producing a strong frequency response, the design was based on guided-mode resonance (GMR). To make this approach viable for radio and microwave frequencies, three major challenges were overcome. First, conventional GMR devices have less than 1% fractional bandwidth and this device extended this to 16%. Second, conventional GMR devices have a field-of-view less than  $1^\circ$  and this device extended this to over  $40^\circ$ . Third, conventional GMR devices must be composed of hundreds of periods to operate, but this device operated very well with only eight. The design in this chapter survived field power levels exceeding  $1.0 \text{ GW/m}^2$ .

### 5.1 Device introduction

Frequency selective surfaces (FSSs) are devices designed to block or pass certain frequencies [4]. They are typically flat and composed of metallic grids to produce the frequency response. Metallic grids, however, are problematic at very high power. Arcing occurs at field concentration points and heating occurs due to ohmic losses experienced by strong currents in the conductors [11] and [14]. In Ref [14], Li et al employed a miniaturized-element FSS to reduce the amplitude of the local electric field and tested their device at a peak power of 25 kW. Their FSS was cleverly composed of alternating layers of dielectric and metal grids so as to separate the capacitive and inductive layers. In this work an all-dielectric approach was adopted that was monolithic and completely avoided the use of metals. This device was successfully tested at a peak power of  $1.7 \text{ GW/m}^2$ . The monolithic construction makes it more robust to vibration, internal stresses arising from temperature cycling, and many other problems that arise from composite materials.

Dielectrics, however, exhibit a much weaker interaction with the field than do metals. Design options are more limited and it is very difficult to produce a strong frequency response in a compact form factor. To be compact, this device was based on the phenomenon of guided-mode resonance [20]. This phenomenon has been studied extensively at optical frequencies, but is still very immature at radio and microwave frequencies. Three major problems arise that must be overcome to make all-dielectric FSSs viable at radio and microwave frequencies. First, their bandwidth is prohibitively narrow, with a fractional bandwidth (FBW) typically less than 1%. Second, the field-of-view (FOV) is extremely narrow, often much less than  $1^\circ$ . Third, conventional all-dielectric FSSs must be composed of many hundreds of periods, [23] and [27], making the overall size unfeasible. In the work following, a compact all-dielectric FSS for high power microwaves was developed that overcomes all of these challenges and is polarization insensitive at normal incidence.

## **5.2 Design approach**

As it was discussed in Chapter 4, it is known that the coupling between an external wave and the guided-mode in an all-dielectric FSS is usually weak and hundreds of periods are necessary in order to establish a sufficiently strong resonance. Furthermore, the sensitivity of the phase matching condition causes the resonance to occur over very narrow frequency bands and over a very limited FOV. In recent work, Bragg grating reflectors were used at the edges of a GMR device to let it operate with less than 20 periods [65]. The area of the Bragg grating regions, however, was almost seven times larger than the GMR region itself making it infeasible to implement at microwave frequencies. In other work, compact metal reflectors were placed at the edges of a seven-period all-dielectric FSS to effectively “unfold” it into a device of infinite extent [23]. This approach, however, does not avoid the use of metal making it less desirable for applications at high power. Other recent work focused on broadband GMR devices using multiple overlapping resonances [62], but these devices still suffer from a small FOV and are polarization sensitive. To solve all of these problems in a simple compact device, a deep grating design in a

moderately high dielectric constant material,  $\epsilon_r = 10$  was adopted. A crossed grating was chosen so that the FSS would be less sensitive to polarization due to the  $90^\circ$  rotational symmetry.

### 5.3 PSO implementation

Particle swarm optimization (PSO) [56] was used to optimize the pattern and geometry of the grating over many continuous degrees of freedom. A critical aspect of any optimization is the merit function, MF. This is a single number that quantifies how “good” a candidate design is. This can be challenging, especially when there are multiple constraints of varying relative importance. The design in this work was optimized for minimum transmittance over maximum fractional bandwidth (FBW) and maximum FOV. To calculate the merit function for a candidate design, the frequency response of the device was first simulated using rigorous coupled-wave analysis [49] and [53]. This method was chosen because it is extremely fast and efficient for dielectric devices, allowing more iterations to be performed. Given the transmittance through the device on a dB scale, the largest possible rectangle that fit within a valley of the spectral response was found. This concept is illustrated in Figure 5.1.

$$\text{FBW} = \frac{\Delta f}{f_c} = 2 \frac{f_2 - f_1}{f_2 + f_1} \quad (2.3.1)$$

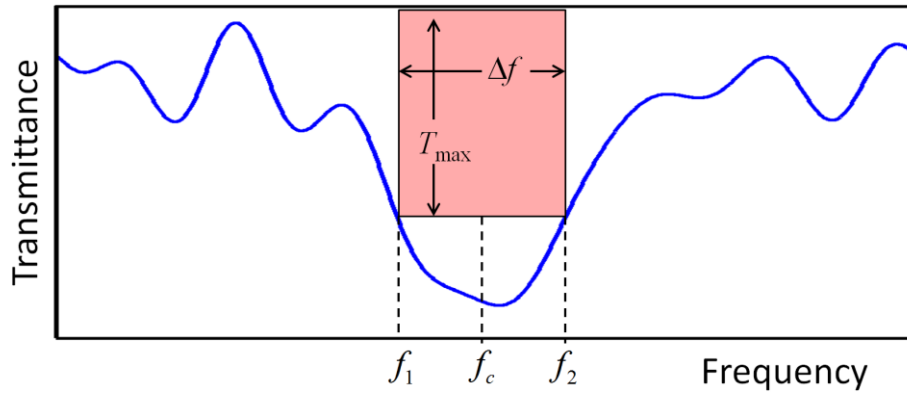


Figure 5.1: Illustration of finding the maximum bandwidth and transmittance.

The width of this rectangle,  $\Delta f$ , was interpreted as the bandwidth of the device, from which the FBW was calculated. This formula is shown in Eq. (2.3.1). The height of the rectangle was interpreted as the maximum transmittance,  $T_{\max}$ , of the device over that bandwidth.

In a similar manner, the transmittance as a function of angle of incidence at the center frequency  $f_c$  was calculated. The FOV was assessed by first simulating the device over a span of elevation angles with the azimuthal angle set to  $0^\circ$  and then simulating the same elevation angles but with the azimuthal set to  $45^\circ$ . To account for the response to all possible polarizations in a numerically efficient manner, the source in the simulations was made to be circularly polarized (CP). In this manner, optimizing for CP automatically optimized the device for both TE and TM polarizations. The FOV was defined as the span of elevation angles over which the transmittance remained greater than or equal to  $T_{\max}$  determined previously. The overall merit function is given in Eq. (2.3.2). On a decibel scale,  $T_{\max}$  is negative, so the absolute value in this calculation was taken to simplify the processing of the merit function evaluation.

$$|MF| = T_{\max} \cdot FBW \cdot FOV \quad (2.3.2)$$

#### 5.4 Finite length analysis

Studying the array effects of these doubly periodic all-dielectric FSSs is beyond the current computational capabilities available for this work. In order to investigate the effect of a finite number of periods, a ruled grating designed using the above PSO technique with a TM plane wave source was studied. The assumption for this study was that the number of periods needed for a ruled grating to excite a sufficiently strong guided-mode would be roughly the same for a crossed grating. The device developed from this optimization can be seen in Figure 5.2

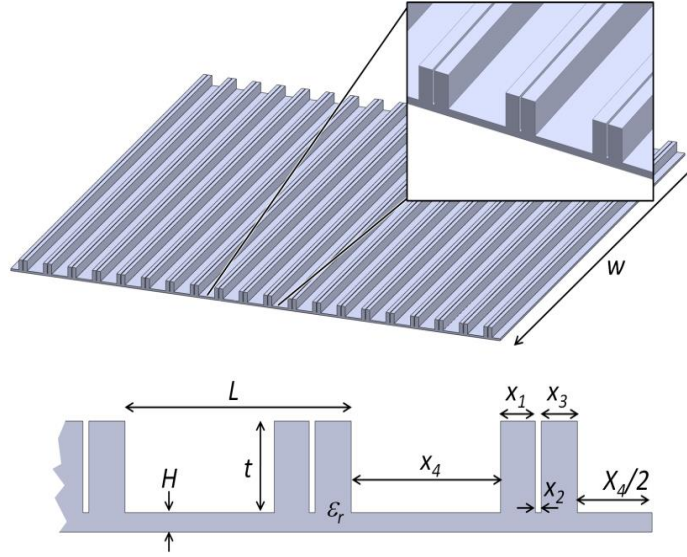


Figure 5.2: PSO designed ruled grating all-dielectric FSS. The dimensions from the optimization are:  $X_1 = 0.6388$  mm,  $X_2 = 3.6227$  mm,  $X_3 = 5.9314$  mm,  $X_4 = 2.1743$  mm,  $h = 10.4395$  mm,  $t = 1.3505$  mm and  $\epsilon_r = 10$ .

Once the ruled grating design was completed, a parametric sweep of the number of periods needed for a strong response was performed. This sweep was simulated using finite-difference frequency-domain (FDFD). In this simulation one unit cell was added each iteration and a frequency sweep was performed on it. From this frequency sweep the total power transmitted was calculated and recorded for each frequency point. It can be seen in Figure 5.3 that the device started to behave approximately like the infinite case with only 5 periods.

Several trends were observed during the optimization work. First, the thickness of the substrate under the grating always tended toward zero. The substrate does not contribute to diffraction or coupling so it was surmised this trend arose to maximize the coupling strength between the applied wave and the guided-mode. Second, the dimensions of the slots and fins always tended toward extreme values. It was surmised this was due to the optimization simultaneously tailoring the diffraction of the applied wave and dispersion of the guided-mode. Since these devices are leaky waveguides, the reciprocity theorem, [26], tells us that if stronger

mode coupling is achieved, then energy must out-couple over fewer periods. When this is achieved, it is possible excite a guided-mode using fewer periods.

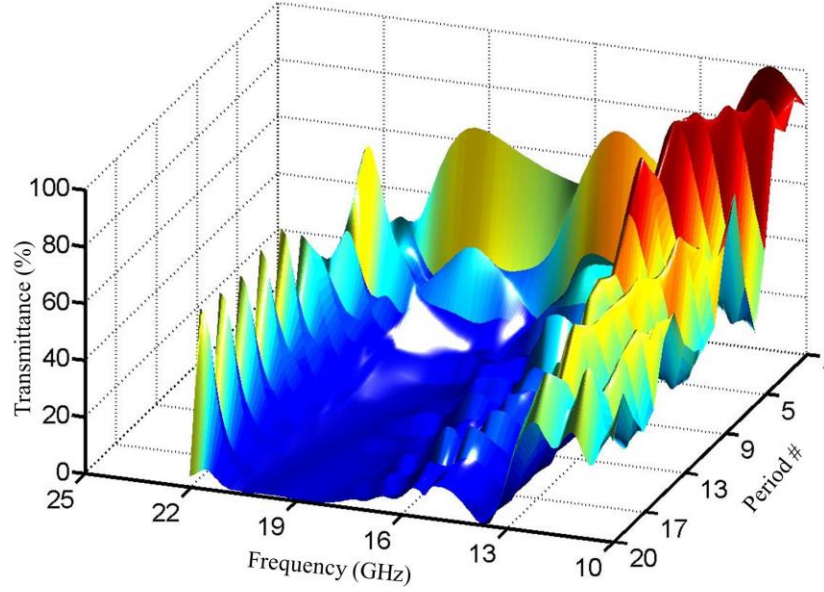


Figure 5.3: Ruled grating spectral response at TE polarization showing the effect of number of periods. The device was swept from 1 to 20 periods. Convergence was achieved around 5 periods.

The physical dimensions were constrained to values that were robust and feasible to manufacture. This design approach was called a “hyper-grating” because it exhibited abnormally strong coupling between external waves and the guided-modes.

### 5.5 Optimized Crossed Grating FSS

Based on all of this, a crossed grating all-dielectric FSS was designed and optimized using the above technique. The FSS design inputted into the PSO was a square array of concentric squares with varying wall and slot thicknesses. The inner square had a thick wall while the outer square dividing the unit cells had a thin wall. As with the ruled grating optimizations, similar extreme dimensions for the crossed hyper-gratings was observed. The experimental results of this device suggest that the assumption of equivalent number of periods is correct. In Figure 5.4, the crossed grating all-dielectric FSS after the optimization is shown.

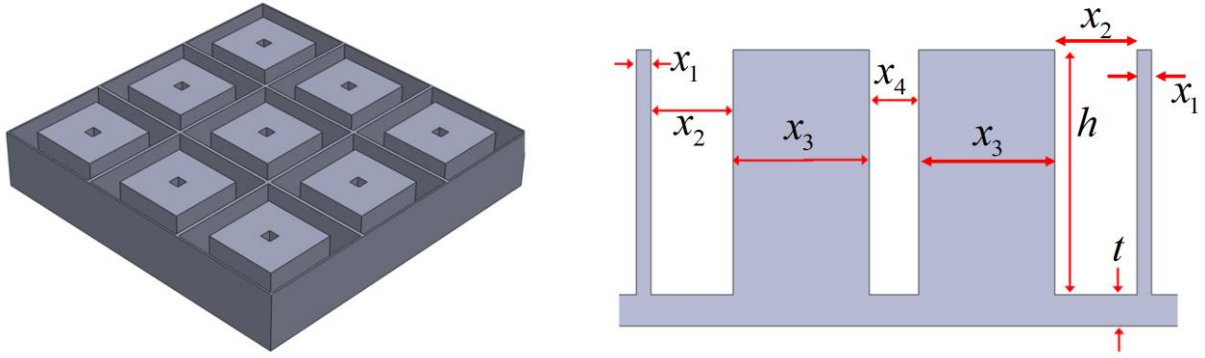


Figure 5.4: PSO designed crossed grating all-dielectric frequency selective surface. The dimensions from the optimization are:  $x_1 = 0.6388$  mm,  $x_2 = 3.6227$  mm,  $x_3 = 5.9314$  mm,  $x_4 = 2.1743$  mm,  $h = 10.4395$  mm,  $t = 1.3505$  mm, and  $\epsilon_r = 10$ .

In Figure 5.5, the simulated response of the device can be seen. The TE and TM modes were independently simulated at normal incidence to show that they indeed have the same response as the CP wave optimization. This design was predicted to provide over 20 dB of suppression over a fractional bandwidth of 14%.

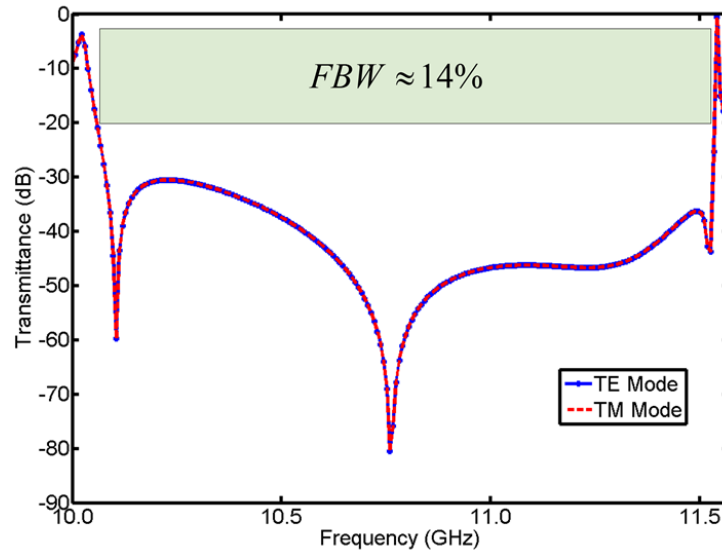


Figure 5.5: Transmittance of all-dielectric FSS showing both TE and TM modes at normal angle of incidence. This device has a fractional bandwidth (FBW) of approximately 14%.

To study the effect angle of incidence has on this device, the simulations were run again, except this time the elevation angles were swept from  $0^\circ$  to  $15^\circ$ , keeping the azimuthal angle fixed at  $0^\circ$ . Then, the azimuthal angle was fixed at  $45^\circ$  and the elevation angle swept again. This was done for both the TE and TM polarizations. As can be seen in Figure 5.6, this device provided a FOV of approximately  $23^\circ$ .

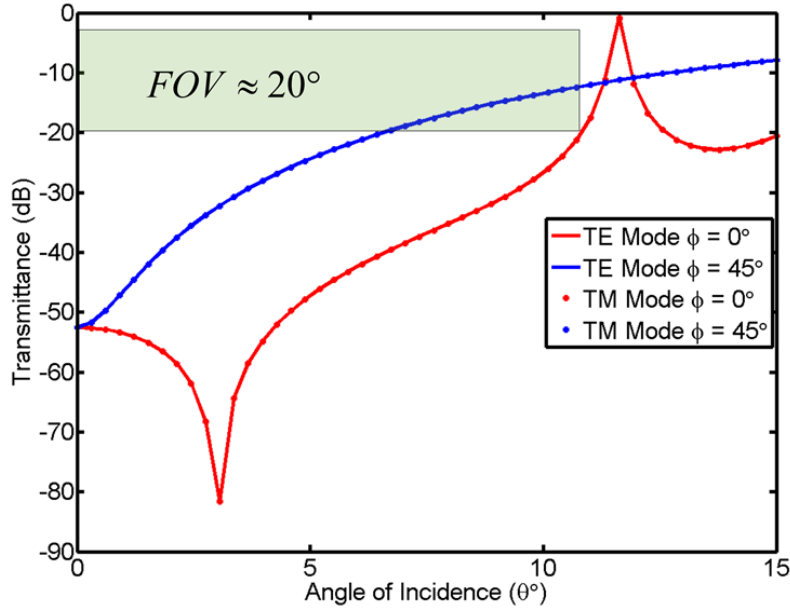


Figure 5.6: Field-of-view response for a center resonant frequency of 10.6 GHz showing both the TE and TM modes. This showed a FOV of approximately  $23^\circ$

## 5.6 Experimental Results

A prototype all-dielectric FSS was machined from a monolithic slab of Laird ECCOSTOCK HiK composite with a nominal dielectric constant of 10.0. A numerically controlled mill was programmed to machine an array of  $8 \times 8$  unit cells according to the design shown in Figure 5.4. During the machining process, the material chosen for this device was found to be very difficult to cut and drill. This led to the manufactured device not being perfectly symmetric. In addition, the dimensions of the walls and slots varied over the aperture of the device. These defects in the manufacturing are believed to be the cause of the asymmetric polarization response in the measurement that was observed.

The all-dielectric FSS was experimentally tested in the University of Texas at El Paso EM Lab's anechoic test facility to verify the simulated results. It was placed onto a Styrofoam platform and illuminated by a standard gain horn antenna operating within the X-band (8.0 GHz – 12.0 GHz). An Agilent N5245 PNA-X Vector Network Analyzer in conjunction with an Agilent 83006A Microwave System Amplifier was used to measure the transmittance  $S_{21}$  through the device. The illuminating horn was placed 71 inches away from the FSS to better approximate a plane wave.

This distance was chosen at where the spectra converged and no longer changed with further placement of the antenna. A similar receiving antenna was placed 12 inches behind the device to detect the transmitted power. This distance and position was chosen to ensure that the receiving horn was within the “shadow zone” of the device, but far enough way that it did not interfere with the operation of the FSS. A photograph of the device in the experimental setup is shown in Figure 5.7.

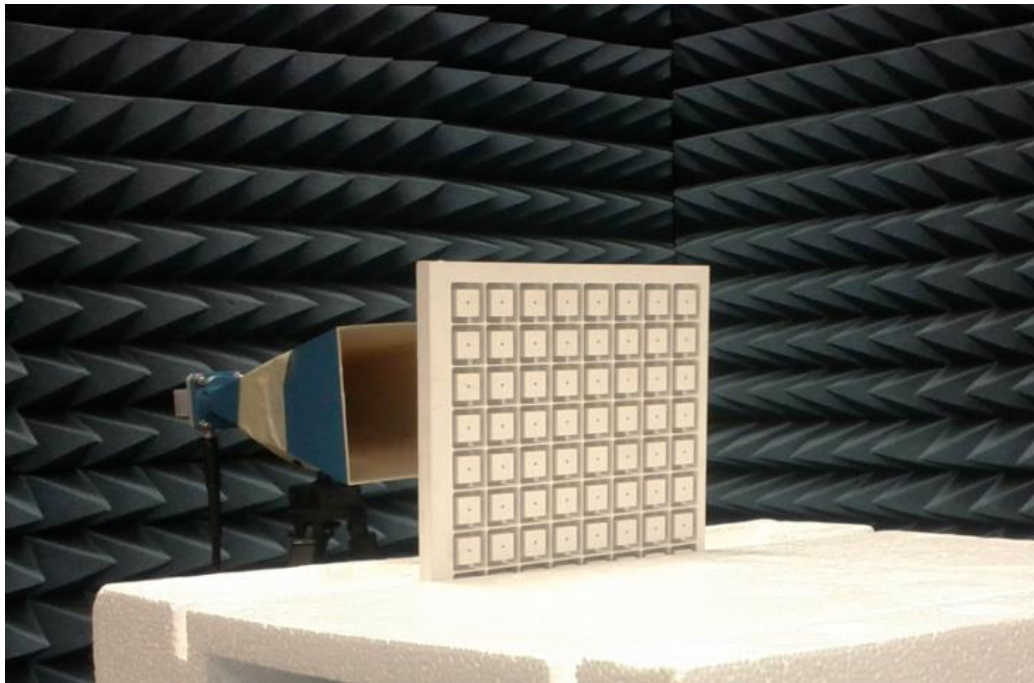


Figure 5.7: All-dielectric FSS under test.

The device was illuminated with a TE polarized beam from the transmitting horn. After the transmittance was measured and recorded, the device was rotated  $90^\circ$  to test the TM polarization response. The resulting spectra can be seen in Figure 5.8.

The TE polarization spectrum closely matched the simulated data and exceeded the performance of the simulation. The TM polarization spectrum had a similar response but with a slightly different shape. This discrepancy was attributed to the deformations of the unit cells created during the manufacturing of the device. The device was found to be quite robust to these structural deformations.

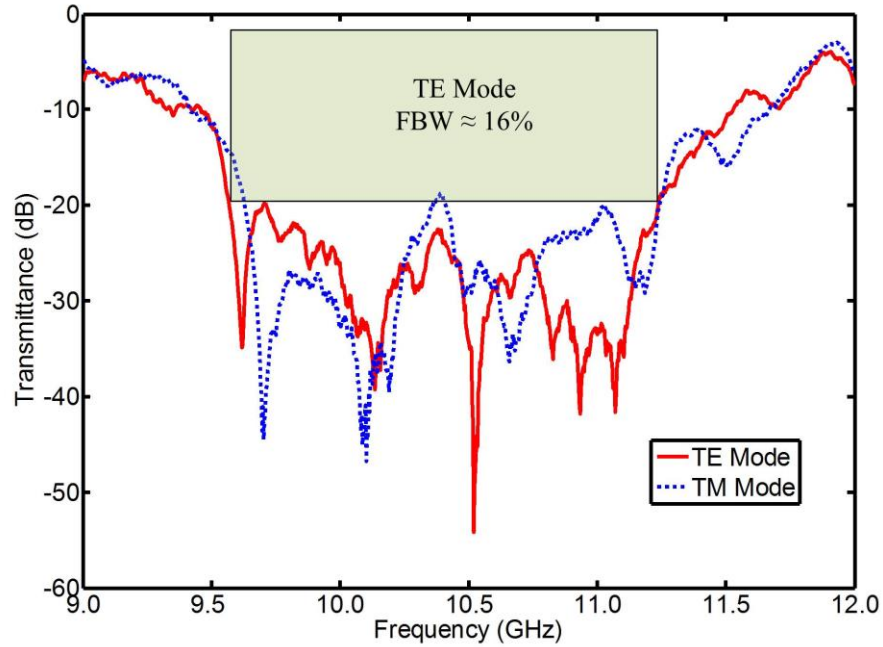


Figure 5.8: Experimental spectral response of the all-dielectric FSS being illuminated by a TE and TM polarized plane wave. In this polarization, the device showed a fractional bandwidth of 16% for the TE mode.

To assess the FOV, the device was measured eight different times while rotating it in increments of  $5^\circ$  from the normal each time. The measured results for transmittance and FOV are provided in Figure 5.9. The FOV for TM polarization for this device was characterized in the same manner as the FOV for TE. This sweep yielded a slightly different characteristic of the TM polarized response.

For the TE polarization, a resonant shift of around 0.4 GHz between the simulated and measured frequency response was observed. This was attributed to the dielectric constant of the material being slightly higher than 10.0. A difference of less than  $\Delta\epsilon = 0.8$  can account for this offset. The dielectric constant of a different batch of the same material was measured to be 10.5. A much larger FOV than the simulation predicted was also observed. This has been a consistent occurrence with finite period devices. They are designed as an infinitely periodic array, yet they are operated and tested as a finite array with very few periods. This difference was attributed to the device being a finite array.

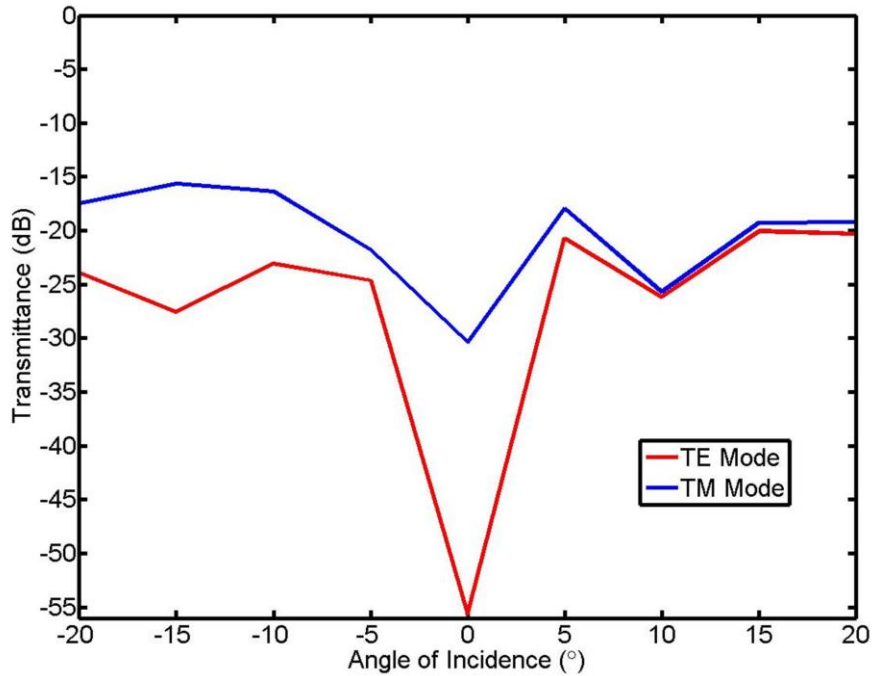


Figure 5.9: Field-of-view sweep of the all dielectric FSS being illuminated with a TE polarized plane wave at center frequency of 10.5 GHz. The device was rotated 90° and swept again for the TM polarization.

After the low power testing was complete, the device was tested at high power at the White Sands Missile Range (WSMR) Survivability Vulnerability Assessment Directorate (SVAD) High Power Microwave Test Site using their Narrowband Threat Simulator B (NBTS-B). To evaluate the FSS in the worst case, it was tested at its resonant frequency, 10.5 GHz. The device was mounted onto a Teflon test fixture 1.9 m away from the transmitting antenna. An absorbing foam

boundary was placed around the device to suppress diffraction around the edges. The device was then illuminated at this distance with a 3.1 ns high-power microwave pulse with a peak power density of  $1.7\text{GW}/\text{m}^2$ . The device filtered the pulse adequately and no plasma, arcing, or visible damage was detected. A suppression of -24.5 dB was measured through the FSS at high power, consistent with the simulations and measurements at low power. The test was repeated multiple times and the FSS performed consistently with no damage or arcing. Data from the pulse through the device is provided in Figure 5.10.

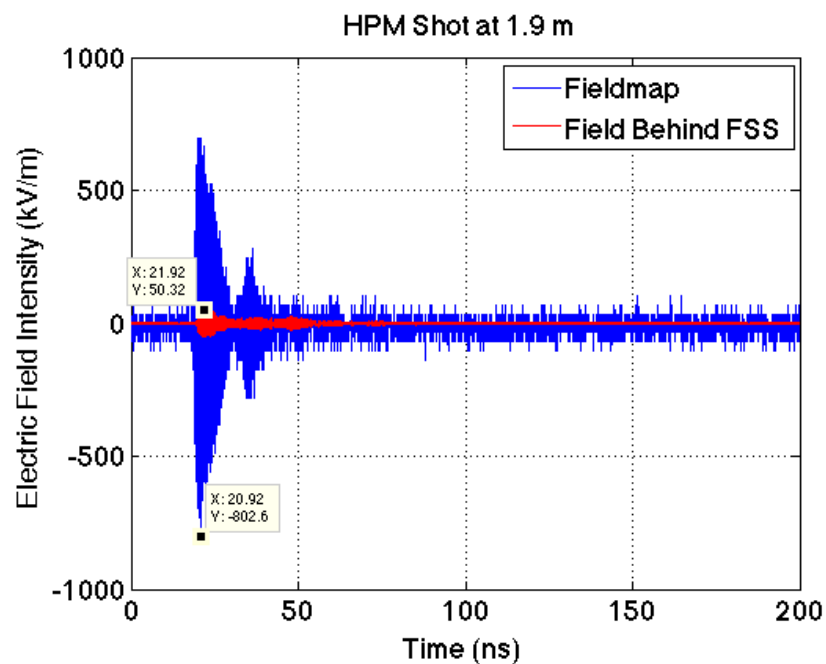


Figure 5.10: Time domain response of the all-dielectric FSS illuminated with a TE polarized HPM pulse at 1.9m. To put the frequency right in the middle of the stop band, the source was tuned to 10.5 GHz.

## 5.7 Device conclusion

For high power microwaves, the use of resonant metallic elements in frequency selective surfaces can be problematic. In this chapter, an all-dielectric frequency selective surface that avoided all use of metals was presented. It provided greater than 20 dB of suppression over a 16% fractional bandwidth and over  $40^\circ$  field-of-view. This device is also unique in that it is a monolithic

slab of dielectric that is robust to temperature cycling and vibration. Theoretically, and in simulation, this device was polarization insensitive at normal wave incidence. Though, due to inaccuracies and asymmetric unit cells caused by the machining process, the device showed two different polarization responses experimentally. This technology may find a variety of applications in high power microwave systems including radomes, beam shaping, and more.

## Chapter 6: 3D Printed All-Dielectric FSS for HPM Applications

In this paper an all-dielectric frequency selective surface was developed using a novel technique involving fast Fourier transforms and genetic algorithms. This devices showed a stop-band fractional bandwidth of 50% and an impressive field-of-view on resonance of  $16^\circ$ . The FSS optimized was successfully 3D printed and the results were experimentally verified. This device was then tested in a high-power environment. The stop-band and pass-band were tested and the device performed with no damage. This is the first known 3D printed all-dielectric frequency selective surface.

### 6.1 Device introduction

This all-dielectric frequency selective surface works using a phenomenon known as guided-mode resonance (GMR). Guided-mode resonance occurs when an incident plane-wave is diffracted into a specific set of spatial harmonics that match a supported mode within a dielectric slab waveguide. Due to the grating, this dielectric slab waveguide is also a leaky waveguide. Over the aperture of the FSS, the power that was coupled into the waveguide is leaked out. The interference between the applied wave and leaked wave induced by this leaky waveguide causes a very strong frequency selectivity response as can be seen in Figure 1.4.

Traditionally, the GMR phenomenon is used most commonly at optical frequencies. When they are adapted for use in the radio and microwave frequency range, several challenges arise that must be overcome for them to be practical. The first challenge to this is the number of periods needed to obtain a strong frequency selectivity response. Traditional GMR devices require hundreds of periods to create a strong response, [23] and [27]. These GMR devices have very weak coupling. This has been solved for microwave frequencies with the implementation of the hyper-grating effect described in Ref **Error! Reference source not found.**. The hyper-grating effect states that if these devices are leaky waveguides, the reciprocity theorem tells us that if very rapid mode coupling is achieved, then energy must out-couple over fewer periods. When this is

achieved, it is possible excite a guided-mode using fewer periods. This strong mode coupling leads to a strong frequency selectivity response using a exiguous number of periods.

The second challenge is the bandwidth and FOV of these devices is prohibitively narrow, with a fractional bandwidth (FBW) typically less than 1% and FOV often much less than 1°. One solution to this problem was developed by Magnusson et al in Ref [62]. Their solution was to induce multiple diffracted orders into the guided-mode. When this is achieved multiple resonances are combined together, broadening the device's FBW. While this solution broadens the FBW, the FOV was not considered. This device provided approximately -20 dB of suppression across a 31.6% FBW while retaining a FOV value of only 2°.

The FSS described within this chapter simultaneously optimized the diffracted orders of the spatial harmonics and the dispersion of the guided-mode to drastically increase the FOV and FBW of this device implementing the hyper-grating effect to achieve a strong response with a exiguous number of periods.

## 6.2 Phenotype generation

A GAO was implemented in the design of this FSS. The formulas and techniques described in Chapter 3, section 3.3 was used to implement this optimization. For this optimization to be implemented a method needed to be developed to randomly generate the phenotypes. This generation needed to be somewhat controlled as to allow the ability to 3D print the device.

The phenotypes used in this optimization took on the form of a 2D data array made up of 32x51 pixels, or chromosomes. Each one of these chromosomes could have one of two properties, the dielectric resin used in stereolithography 3D printing, or a dielectric powder. The entire phenotype was surrounded by a dielectric wall designed to have a width of 0.5 mm. This was done to be able to optimize multiple periods using multiple dielectric powders if needed.

The dielectric constant of the stereolithography resin  $\epsilon_{SLA}$  was measured to be 2.58 in the X-band range frequencies while the dielectric constant range of the powders  $\epsilon_p^i$  was chosen to correspond with the range of low loss dielectric powders available from Laird Technologies. Two

additional chromosomes were then added to be optimized. These were the period height  $H$  and length  $L$ . The final phenotype form can be seen in Figure 6.1.

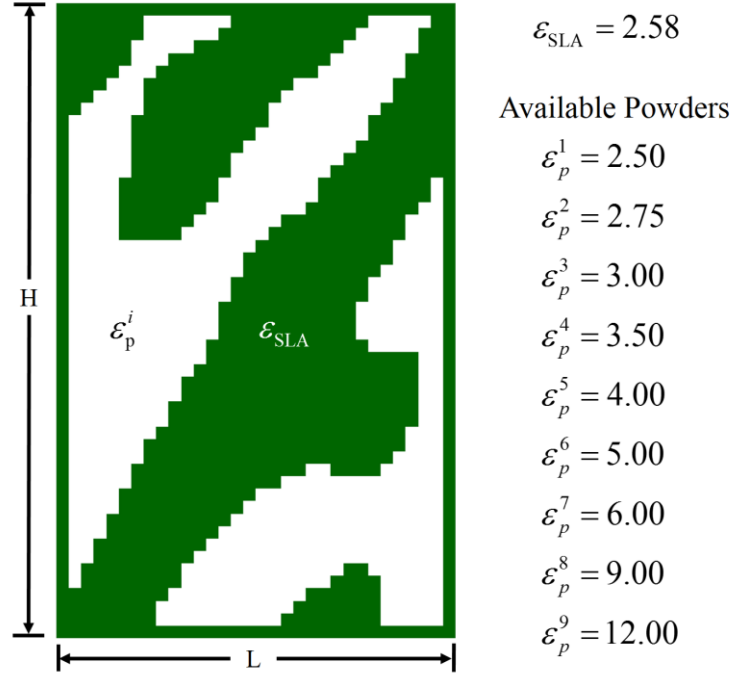


Figure 6.1: Example phenotype. In this figure is shown the dielectric constant of the stereolithography resin, and the dielectric constants of the available powders.

With the solution space initialized, a method was developed to generate random phenotypes to search this space. To generate the random geometries needed, all the chromosomes in the phenotype data array were initialized with random numbers ranging from -0.5 to 0.5. A two dimensional fast Fourier transform (FFT) was then applied to this array [67]-[69]. This is shown in Figure 6.2. Applying a FFT to this random number data array transforms the random numbers into the complex amplitudes of a unique set of spatial harmonics. The makeup of this spatial harmonic array is unique for the random number data array it was created from. This allows the same type of operation to be performed on all the different spatial harmonic arrays of the phenotypes and still be able to achieve randomness with the makeup of the random number array.

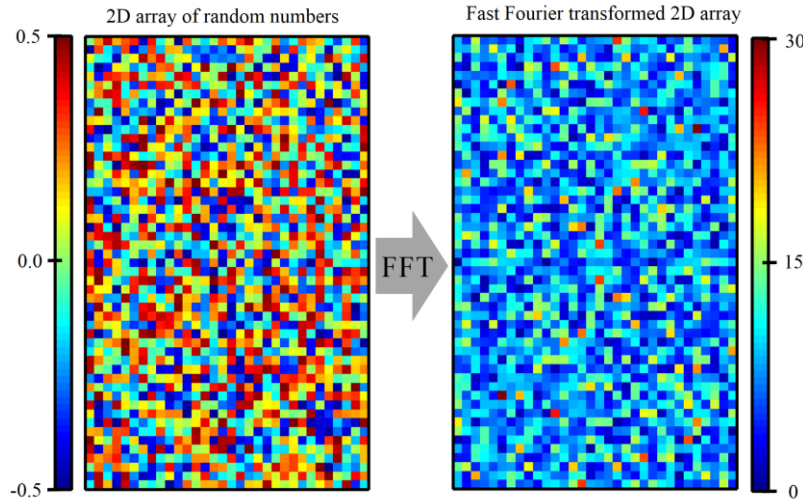


Figure 6.2: This figure shows the generated 2D data array of random numbers. A FFT is then applied to this array resulting in an array of unique spatial harmonics.

From here, the high-frequency noise is filtered out. This was done by keeping the spatial harmonics in a designated area around the center of array and setting the rest to zero. By controlling the size of the area around the center spatial harmonic gives some control to the generated shapes. When more high frequency spatial harmonics are kept, designs have more rapid variations of dielectric. If too few high frequency spatial harmonics are kept, all that is generated is a solid sheet of dielectric with slow variation.

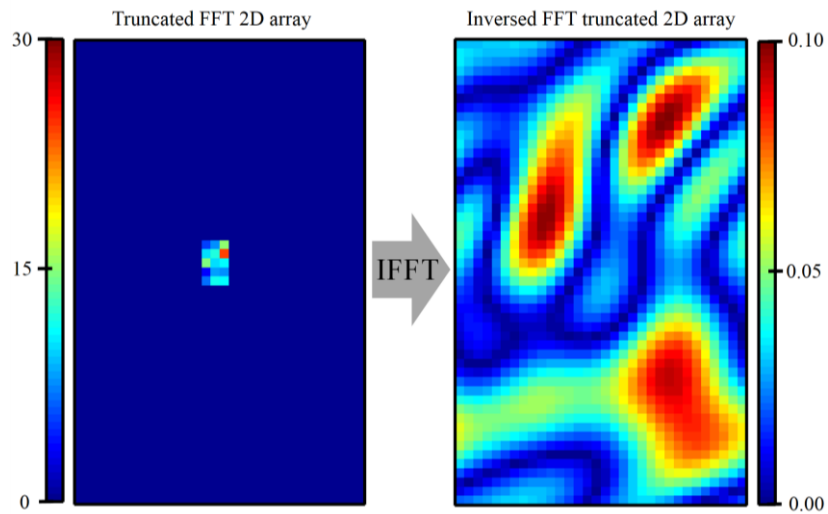


Figure 6.3: This figure shows the truncated FFT 2D data array. A inverse FFT is then performed on this array generating the second array.

An inverse FFT (IFFT) was then applied to the truncated FFT 2D data array. This produces the patterns and shapes that can be seen in Figure 6.3.

The IFFT data array was then normalized by subtracting the minimum number in the array and then dividing the entire array by the maximum number in the array. A threshold operation is then applied to these patterns. In this threshold operation a number is chosen between one and zero and anything above this value is kept while the rest is discarded. This tolerance number controls the final fill fraction of the phenotype.

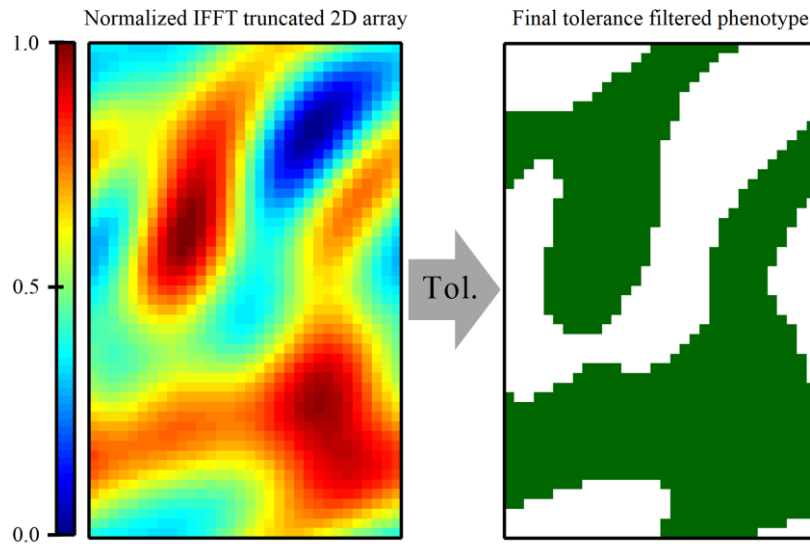


Figure 6.4: In this figure the normalized truncated IFFT 2D grid is shown with the tolerance filtered grid right next to it.

The final phenotype generated can be seen in Figure 6.4. From here, the width of the 0.5 mm walls in the unit cells were placed around the phenotype to prepare it for optimization.

This methodology of phenotype generation provides the necessary spatial complexity to simultaneously optimize the dispersion and diffraction of the GMR phenomenon to produce devices that have significant suppression over a wide-band and a wide FOV.

### 6.3: Device design

With the GAO formulated, and the phenotype generation handled, the optimization was initialized. This optimization was first designed to optimize two periods simultaneously. Next, 20 data arrays were randomly generated. These 20 data arrays were then combined to make 10 phenotypes. Each phenotype was assigned a random height,  $H$ , and random period length,  $\Lambda$ .

These phenotypes were then fed into a finite-difference frequency domain (FDFD) simulation. The device was scaled with the optimized  $\Lambda$  and  $H$  values and centered in the middle of the simulation grid. Spacer regions the size of one wavelength were placed on bottom and top of the device to allow for the existence of large evanescent fields. This simulation used a TE polarized plane wave as a source. Using this source, a convergence sweep at the center frequency was performed. This data was used to adjust the resolution of the simulation grid so that it had enough resolution to properly simulate the phenotype. From here, a frequency sweep was performed and the center frequency of the stop-band was calculated. This center frequency was used to sweep the FOV. The elevation angles of the FOV was swept from  $-30^\circ$  to  $30^\circ$  in the  $\theta$  direction while keeping the azimuthal angles in the  $\phi$  direction constant at  $0^\circ$ . The merit function values of the spectra and FOV sweep was found and combined in accordance with Ref. **Error! eference source not found.**

At this point, the two best phenotypes were chosen and breed together to produce 10 new phenotype children. After the first generation of breeding, 5 illegitimate phenotype children were introduced into the family bringing the total to 15 children per generation. This process was repeated until a suitable design was found.

The final iteration of the GAO produced the design in Figure 6.5. This design was then simulated with RCWA to verify the results from the FDFD optimization.

The spectra simulated from the two different methods had negligible differences. This design had a height,  $H = 15.22$  mm and  $\Lambda = 36.28$  mm. The dielectric constant of the powder chosen from the optimization had a value of  $\epsilon_p = 12.0$ .

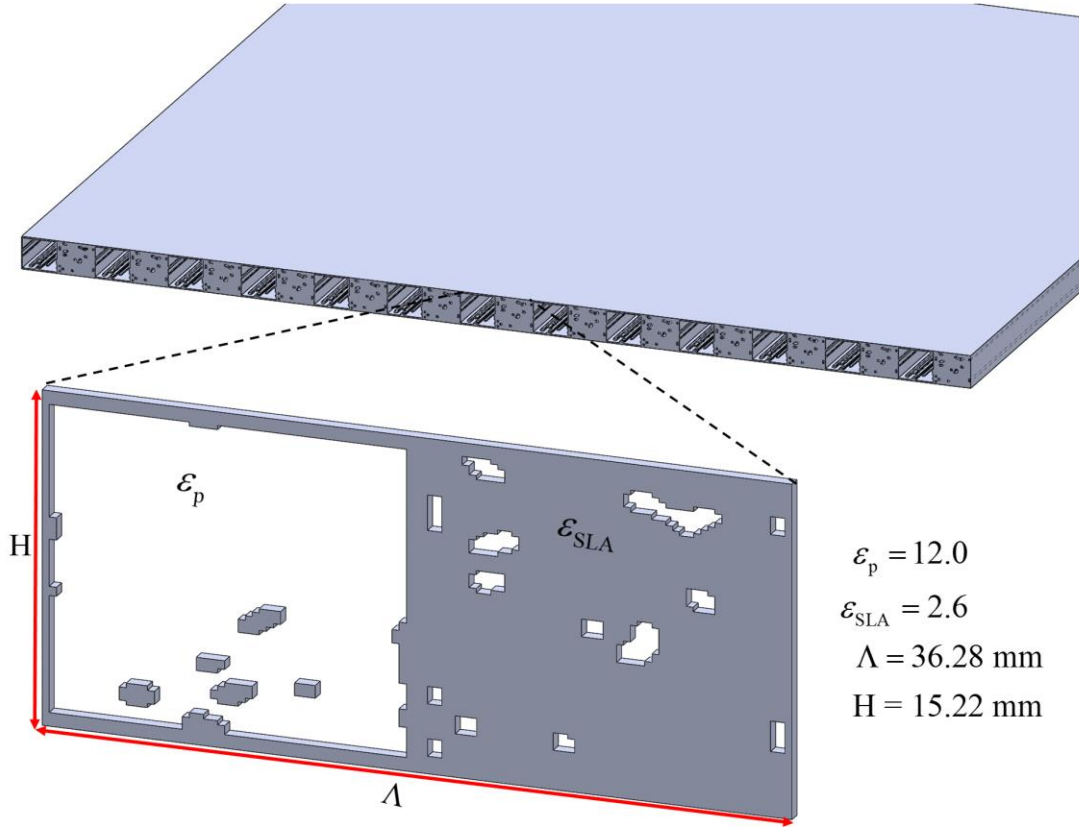


Figure 6.5: Final GAO optimized device

It should be noted in Figure 6.5, that the optimizations always converged to these types of designs with one unit cell almost all high dielectric powder and the other unit cell almost all low dielectric constant material creating a large macro grating. This was hypothesized to have happened because the GAO was optimizing the diffracted spatial harmonics to bring multiple diffracted modes together. These multiple diffracted modes had the effect of creating a hyper-grating as described in Ref. **Error! Reference source not found.** and combining multiple resonances together within the stop-band to broaden the FBW and FOV. The speckles within the macro grating were created from the optimization to adjust the dispersion of the guided-modes within the device to shape the multiple resonances to achieve the maximum FBW and FOV. This optimization had the effect of simultaneously optimizing the diffracted modes and guided-mode dispersion to create this wideband device.

The calculated transmittance for this device showed a remarkable 50% FBW at approximately -20 dB. This spectra can be seen in Figure 6.6. This device showed a 99% filtering of power transmittance across the entire C-band of frequencies. It should be noted that the narrow resonance spikes were not taken in to account in this calculation. Previous work has shown that these narrow resonances are a product of the device being infinitely periodic. These high order resonance are not excited when the device has a finite-number of periods. The merit function calculation used during the optimization was formulated to skip these extremely narrow resonances to account for this physical phenomenon.

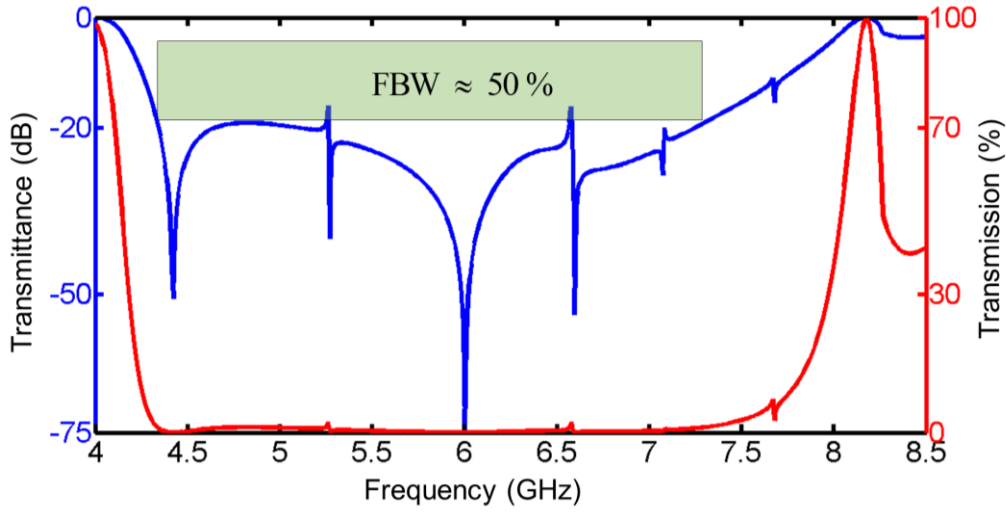


Figure 6.6: Transmittance spectra of the GAO optimized device showing the calculated FBW.

Figure 6.7 shows all the frequencies in the stop-band at different angle-of-incidences. In this figure the FOV sweep was scaled at -20 dB. This was done to illustrate the extent of the -20 dB FOV. The -20 dB FOV on resonance at 6.0 GHz was calculated to be approximately  $16^\circ$ . An interesting phenomenon can be seen in Figure 6.7. While the center resonance has a  $16^\circ$  FOV, off resonance, a channel opens up with a broader FOV, specifically around the 4.6 GHz frequency. This channel shows an amazing -20 dB FOV of approximately  $30^\circ$ . This is to be expected since both the FBW and FOV were optimized simultaneously.

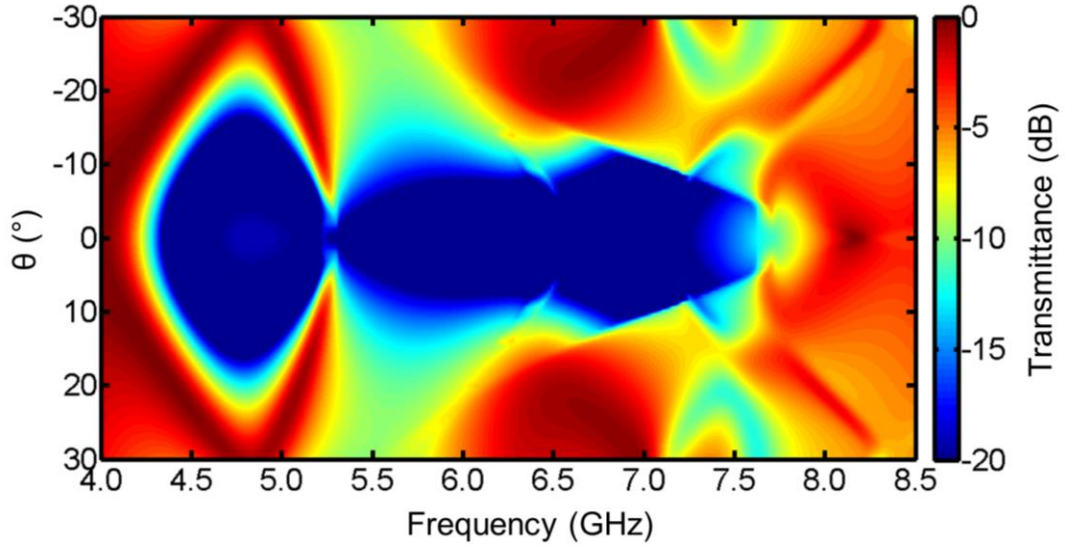


Figure 6.7: FOV sweep of the optimized FSS.

#### 6.4 Experimental results and manufacture

At this point the device was imported into SolidWorks. The imported device was scaled and the CAD drawing was exported to HFSS for design verification. The simulated results from HFSS were compared to the results obtained from RCWA. This can be seen in Figure 6.7.

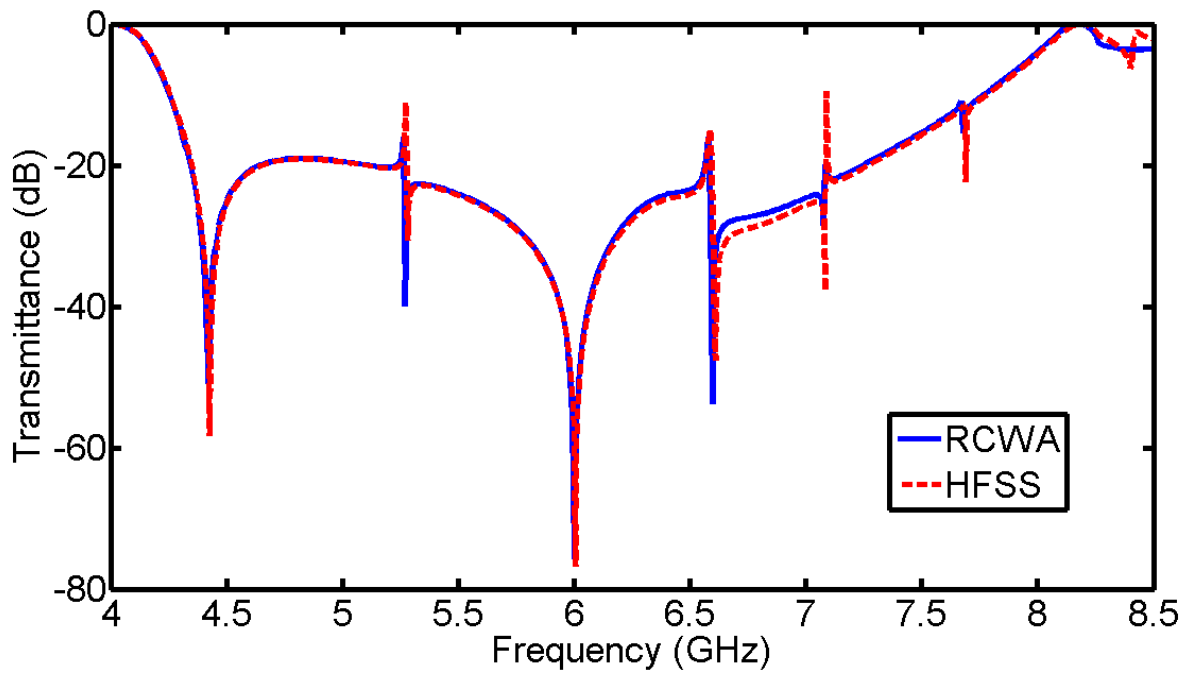


Figure 6.8. Transmittance spectra of GAO device compared with results obtained from HFSS

It should be noted that the simulation time for the device using HFSS took approximately 5 hours while the simulation time of the RCWA code was 3 minutes. This is one of the reasons custom software was used in the optimization of this device. HFSS would be unfeasible with the time it takes to complete one simulation.

From here, the device was arrayed in SolidWorks 10 times to create a 10 period array and extruded to length that made it a square panel. The final dimensions of the panel came out to be 36.41cm x 36.41 cm x 1.578 cm.

The 3D printing technology chosen to manufacture this FSS was stereolithography [70] and [71]. This was chosen in order to manufacture the small feature sizes in the device. This 3D printer works by using a ultraviolet laser and a vat of photosensitive polymer resin. The laser cures a very thin layer of the resin, then the working platform lowers a small amount. Once the resin has settled because of the movement of the platform, the laser cures another very thin layer. This process is repeated until the entire device has been manufactured.

The device CAD file was converted to a STL file format, and slicing was performed with a program called Lightyear. Slicing involves dividing the STL file into layers that the printer produces sequentially.

This sliced file is then inputted into the stereolithography 3D printer for manufacture. The printer used for this was a SLA 500 from 3D Systems. The photosensitive polymer resin used was WaterShed 11122. Figure 6.8 shows the completed FSS.

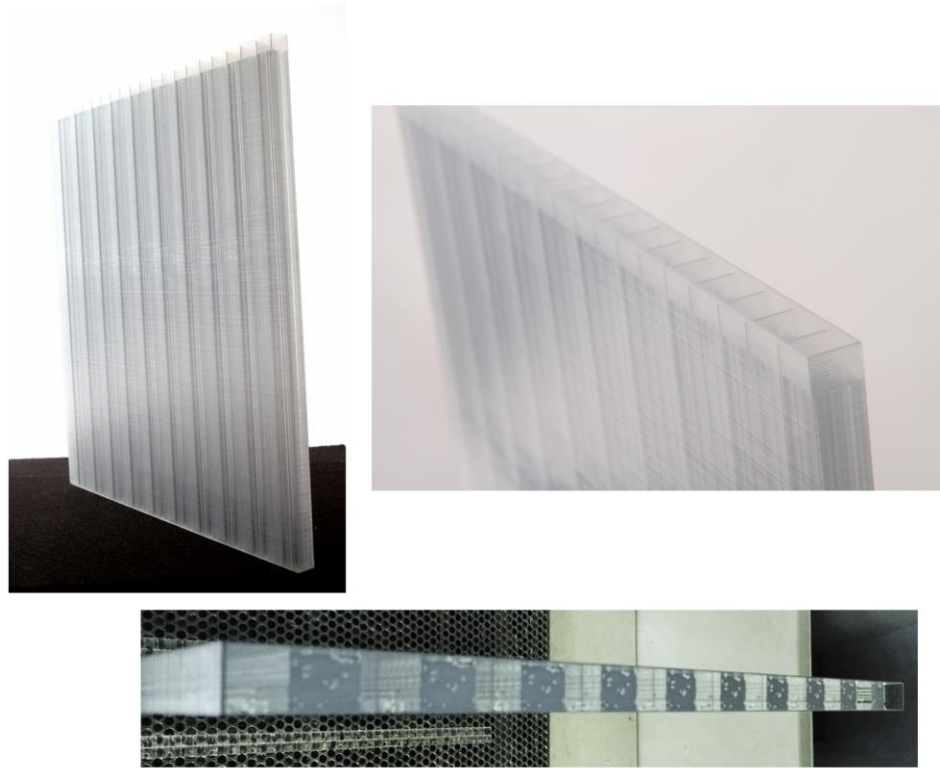


Figure 6.8: Completed 3D printed FSS

Once printed the FSS was packed with Eccostock HiK 12 powder manufactured by Laird. This powder has a approximate dielectric constant of 12 and particle sizes on the order of  $170 \mu\text{m}$ . This was done under a fume hood and the proper protective equipment suggested from the manufacturer was used. When designed in Solidworks, a extra vertical 10 mm section was added to the top of the unit cells and 1 mm thick walls were added separating the unit cells. This was done to be able to separate the powder in the individual unit cells during the packing process. These walls also allowed extra powder to be packed in the upper region of the device to allow the powder to settle and still cover the entire geometry of the unit cells.

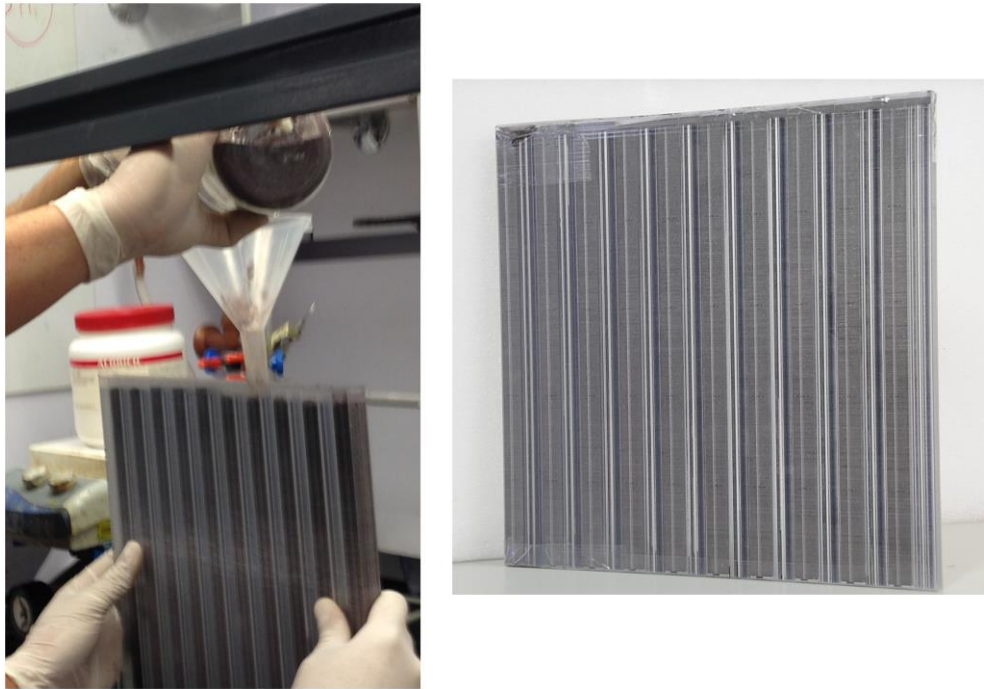


Figure 6.9: Powder packed 3D printed FSS

From here the FSS was taken to an anechoic test facility for low power testing. For low power testing the device was secured to a dielectric stand and two S-band (3.95 GHz – 5.85 GHz) horns were placed on either side of it. An Agilent N5245 PNA-X Vector Network Analyzer in conjunction with an Agilent 83006A Microwave System Amplifier was used to measure the transmittance through the device. The illuminating horn was placed 49 inches away from the FSS to better approximate a plane wave.

This distance was chosen at where the spectra converged and no longer changed with further placement of the antenna. A similar receiving antenna was placed 15 inches behind the device to detect the transmitted power. This distance and position was chosen to ensure that the receiving horn was within the “shadow zone” of the device, but far enough way that it did not interfere with the operation of the FSS. A photograph of the device in the experimental setup is shown in Figure 6.10. The device was then illuminated with a vertical polarized beam. Once this

data was recorded, the horns were replaced with two C-band (5.85 GHz – 8.2 GHz) horns and the resulting spectra was recorded.

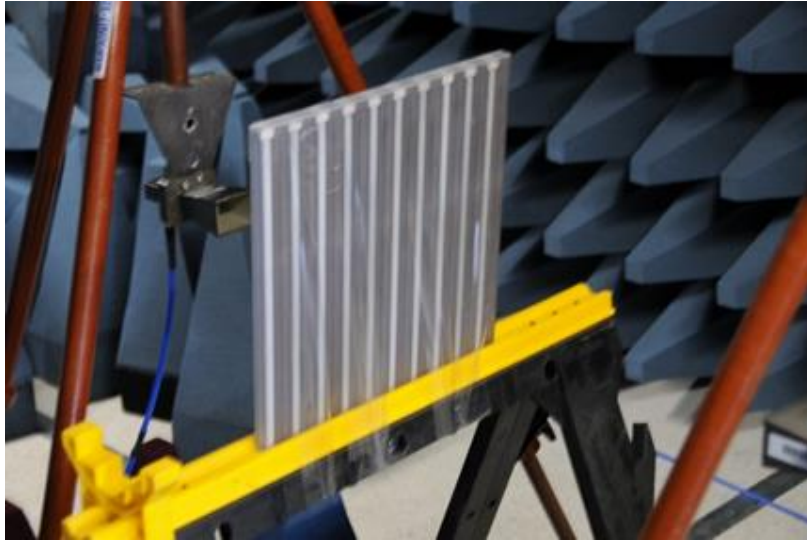


Figure 6.10: Experimental testing of 3D printed FSS.

The vertical polarization spectrum closely matched the simulated data and exceeded the performance of the simulation. There was some anomalies observed within the stop-band. These anomalies are due to the powder not completely filling the entire void of some of the smaller holes in the design. The experimental data showed a FBW of approximately 54%. This can be seen in Figure 6.11.

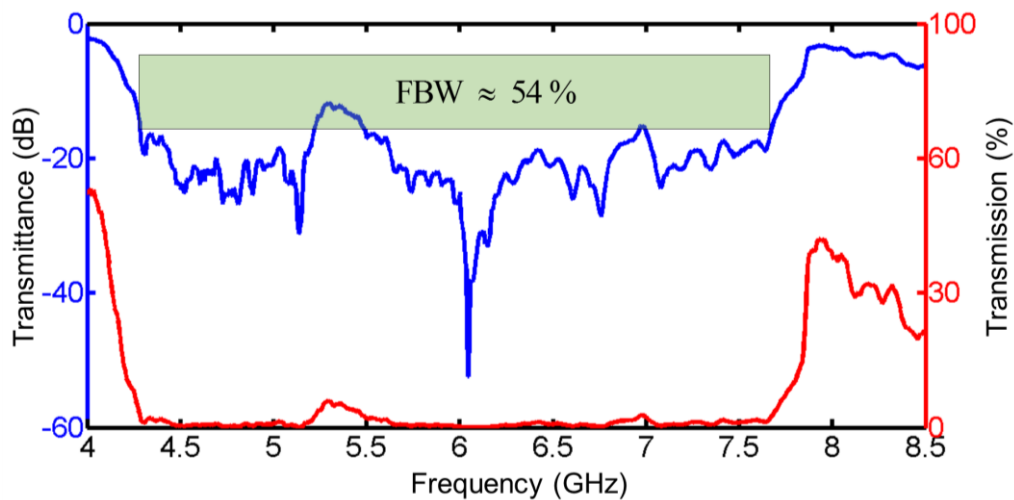


Figure 6.11: Experimental spectra of 3D printed FSS.

To assess the FOV, the device was measured on the resonance of 6.05 GHz seven different times while rotating the transmitting horn in increments of  $2^\circ$  from the normal each time. The measured results for transmittance and FOV are provided in Figure 6.12. While the FOV response of the device closely matched that of the simulation, the experimental results showed a more asymmetric response. This is due to the problems encountered with packing the device.

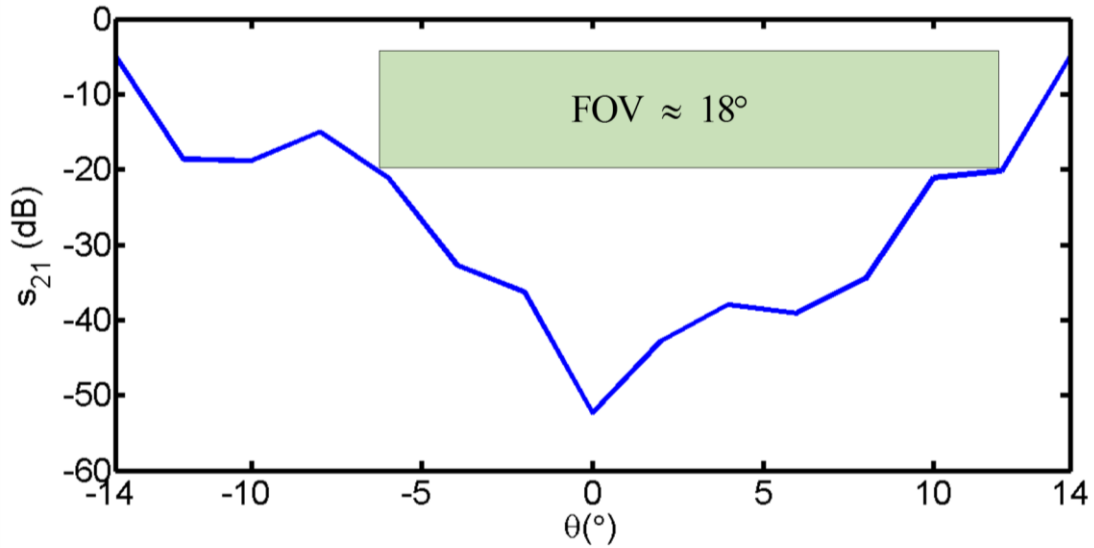


Figure 6.12: Experimental FOV sweep of 3D printed FSS.

It can be seen in Figure 6.11 that there are abnormally large protrusions in the stop band that are not in the simulation. These protrusions are caused from the inability to pack the powder correctly in some of the smaller holes in the design. The inability to pack the powder correctly is caused from two factors. The first is that some of the holes could not be completely cleaned of the photosensitive resin used in the 3D printing process. The second was particle size of the powder was too large compared to the size of the holes. The smallest of the holes had an opening of  $640\ \mu\text{m}$  while the powder particles had sizes approaching  $170\ \mu\text{m}$ . This had the effect of causing the particles to easily bind up during insertion creating partially filled voids and areas within the FSS. Examples of this can be seen in Figure 6.13.



Figure 6.13: Problems highlighted with powder packing

The small holes and features within the device are used to control the dispersion of the guided-mode. When these holes are adjusted or taken away, the multiple resonances within the stop-band change shape. This effect was explored further in simulation to approximate the effect that these poorly packed holes have on the performance of the device. Figure 6.14 shows the original simulation, the experimental results and the corrected simulation.

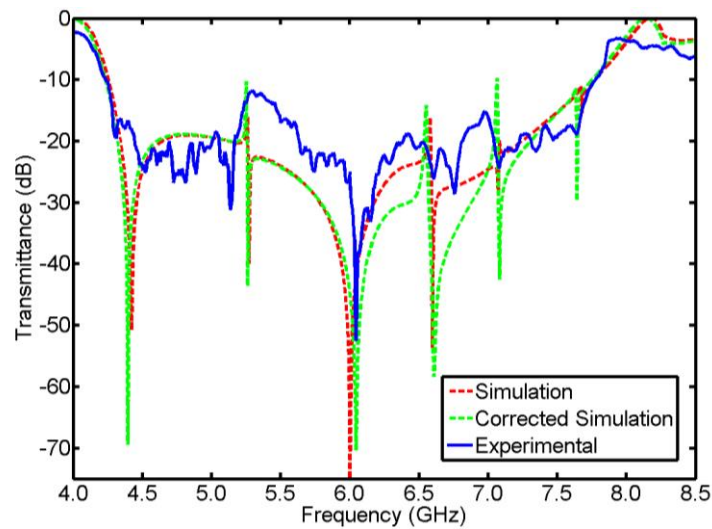


Figure 6.14: Simulation spectra, corrected simulation spectra and experimental spectra shown together to illustrate the dispersion control from the small voids within the design.

It can be seen in this figure that once some of the smaller holes are removed the multiple resonances change shape and shift. Taking this into account and the fact that the panel is a finite-period array, this leads to a shifted and slightly raised suppression spectra.

After the low power testing was complete, the device was tested at high power at the White Sands Missile Range (WSMR) Survivability Vulnerability Assessment Directorate (SVAD) High Power Microwave Test Site using their Narrowband Threat Simulator C (NBTS-C). The frequency chosen for this test was 453 MHz. This was chosen as it is a common frequency used in communication systems. The device was mounted onto a Teflon test fixture 1.0 m away from the transmitting antenna. An absorbing foam boundary was placed around the device to suppress diffraction around the edges. The device was then illuminated at this distance with a high-power microwave pulse with a peak power density of  $45.26 \text{ MW/m}^2$ . The device showed a minimal suppression of -0.1 dB of loss in the passband. This test was performed multiple times and no plasma, arcing, or visible damage was detected. No beam distortion was detected with the device in place.

## **6.5 Device conclusion**

For high power microwaves, the use of resonant metallic elements in frequency selective surfaces can be problematic. In this chapter, an all-dielectric frequency selective surface that avoided all use of metals was presented. It provided greater than 18 dB of suppression over a 54% fractional bandwidth and over  $18^\circ$  field-of-view. This device was tested at high-power and showed no damage in the passband. It adequately transmitted HPM pulses with power levels exceeding  $40 \text{ MW/m}^2$  in the passband with a very minimal loss, less than -0.1 dB, and no beam distortion. This device also has the distinction of being the first known 3D printed FSS. This technology may find a variety of applications in HPM systems including radomes, beam shaping, and more.

## **Chapter 7: Conclusion and Future Work**

In this chapter a summary is given of all the computational electromagnetic methods derived, optimization techniques described, and devices developed in this work.

### **7.1 Conclusion**

This work showed that for high-power microwaves and other extreme environments, the use of resonant metallic elements in frequency selective surfaces can be problematic. The solution developed to solve these problems was to use GMR phenomenon to create frequency selective surfaces that could survive these extreme environments.

To fully understand how these devices operate and to be able to develop them, three computational electromagnetic methods were derived and implemented. The first method to be derived was the FDFD method. This method was used to simulate the two-dimensional devices used in this work, and benchmark traditional GMR devices. The second method to be derived was the MOL method. This method was used in the study of traditional metallic FSSs and as a benchmark for the other methods. The final method implemented was RCWA. This method was used to develop a three-dimensional all-dielectric FSSs and also as a benchmark for the other methods.

Next two optimization algorithms were formulated. These methods were used to develop the all-dielectric FSSs in this work. The first method developed was the PSO algorithm. This algorithm was used to optimize a three-dimensional all-dielectric FSS. The second method was the GAO algorithm. This method was used to develop the first known 3D printed all-dielectric FSS.

Finally, three devices were developed using all the methods and techniques described above. These novel devices solved all the problems associated with all-dielectric FSSs.

The first all-dielectric FSS designed was a traditional GMR device that was modified to work with just seven periods. The methodology behind this device showed that if metallic reflectors were put on the ends of the device and a dielectric spacer region was added to tune the

phase to match that of the guided-mode within, a strong frequency response could be achieved. The all-dielectric FSS was manufactured, experimentally tested and showed a total transmittance suppression of -17 dB.

This all-dielectric FSS showed that a traditional GMR device could be made to work at microwave frequencies with a exiguous number of periods. While this device solved the number of periods problem, it still implemented metals and a composite design that would be problematic in extreme applications. A better solution was sought.

The second all-dielectric FSS took on the form of a symmetric crossed-grating design. The crossed grating was chosen to give this design polarization independence. This design used high-dielectric contrasts and deep gratings to achieve a hyper-grating effect. The hyper-grating effect allowed this device to operate very well with only 8x8 periods. A PSO algorithm was implemented with RCWA to simultaneously engineer the dispersion of the guided-mode and the diffraction the grating. This brought two resonances together and made the FSS broadband and less susceptible to changes in the FOV. The all-dielectric FSS was then manufactured and experimentally tested at low-power. This design showed a 16% FBW at -20 dB, and impressive 40° FOV. The FSS was then tested at high-power at White Sands Missile Range. This test showed that the FSS had a -24.5 dB transmittance suppression on resonance at 10.5 GHz. It survived in high-power environment at a power level of 1.7 GW/m<sup>2</sup> with no damage or detrimental effect to operation. The all-dielectric FSS designed still had a narrowband FBW when compared to it's metallic counterparts and what was in literature about GMR devices. A better design was sought.

The final design developed was a GAO ruled grating all-dielectric FSS. This FSS has the distinction of being the first known 3D printed all-dielectric FSS. A GAO was used to simultaneously engineer the dispersion of the guided-mode and the diffraction of the grating to create a wideband design with deep transmittance suppression and a very large FOV. The GAO all-dielectric FSS showed an impressive 50% FBW with a amazing FOV of 16°. This design also introduced a novel new way to generate devices to use in the GAO that take advantage of the capabilities offered from 3D printing. The FSS was 3D printed, packed with a high dielectric

constant powders and tested at low power. These test showed a FBW of 54% with a FOV of 18°. After the low power tests, the device was taken to White Sands Missile Range. Here it was subjected to high power environment at a max power level exceeding 40 MW/m<sup>2</sup> on the passband. This was done at 453 MHz at a power level of 45.26 MW/m<sup>2</sup>. This test showed very little beam distortion and a transmittance suppression of only -0.1 dB. This FSS far surpassed the previous devices and comes close to matching the performance of traditional metallic FSSs while still being extremely resilient to extreme environments and surviving in environments metallic FSSs cannot.

## 7.2 Future work

The devices developed in this work show that all-dielectric FSSs using GMR can be developed to perform just as well, and in cases exceed, the performance of their metallic counterparts. For this technology to become a viable alternative to metallic FSS, materials need to be developed that are better electromagnetically for 3D printing. As it stands now, the materials available for 3D printers are mostly very lossy and have low dielectric constants. This limits what devices can be printed. In chapter 6, the device was backfilled with a high dielectric constant powder because no printable high dielectric constant material exists. Once the materials catch up, it will be possible to take the concepts from the phenotype generation in chapter 6 and extend them to three dimensions. These super volumetrically complex devices have the potential to generate far greater FBW and suppression depths while still being monolithic devices.

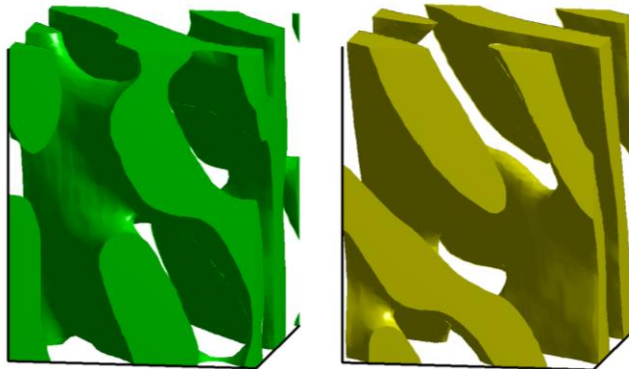


Figure 7.1: Examples of 3D generated phenotypes.

The FSSs in this work have all been designed and manufactured as planar devices. This is practical for laboratory settings, but for actual implementation, this might not be the case. The devices developed using GMR phenomenon have the potential to be spatially varied across a variety of geometries [72]. There has been recent progress in spatially variant metamaterials that would lend itself very well to be used in the spatially varying of FSSs [73]. Using this spatially variant tool would allow for these volumetrically complex devices be built into a conformal FSS. These conformal FSSs could be made to wrap around any shape without losing any performance.

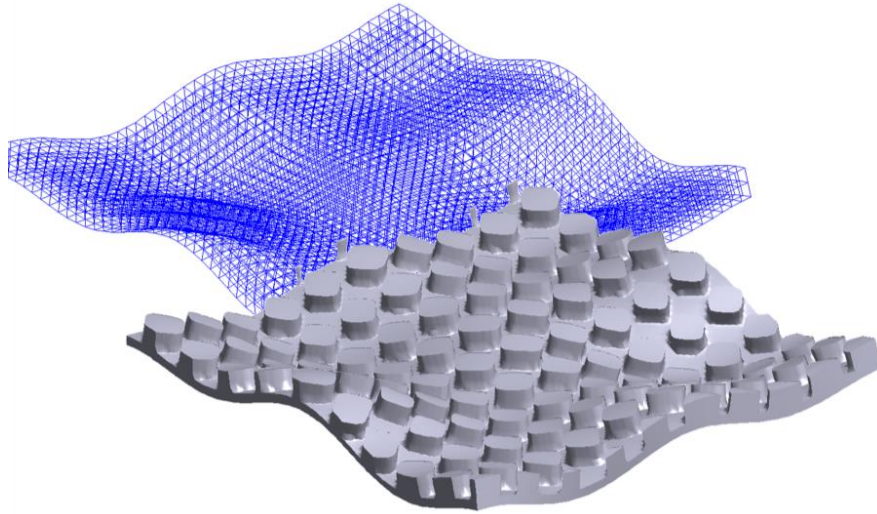


Figure 7.2: Example of a conformal 3D FSS.

The all-dielectric FSS for microwave frequencies is still a very immature technology. The work shown in this dissertation is just a very small sample of what these devices can be optimized to do. With advances in material science and 3D printing, these all-dielectric FSSs have the possibility to be integrated into far more technologies than they are currently being used for. This is especially true for extreme applications where metals and composite devices must be minimized.

## References

- [1] Marconi, G. and C. S. Franklin, "Reflector for use in wireless telegraphy and telephony," US Patent 1,301,473, April 1919.
- [2] Munk, B. A., R. G. Kouyoumjian, and L. Peters, "Reflection properties of periodic surfaces of loaded dipoles," IEEE Trans. on Ant. and Prop., Vol. 19, No. 5, 612-617, 1971.
- [3] Parker, E. A. "The gentleman's guide to frequency selective surfaces." In 17th QMW Antenna Symposium, pp. 1-18. London, UK, Queen Mary and Westfield College, 1991.
- [4] Munk, B., *Frequency Selective Surfaces: Theory and Design*, Wiley, New York, 2005
- [5] Pelton, E. L., Munk, B. A., "A Streamlined Metallic Radome," IEEE Trans. on Ant. and Prop., Vol. 22, No. 6, pp. 799–803, 1974.
- [6] Agahi, S., Mittra, R., "Design of a Cascaded Frequency Selective Surface as a Dichroic Subreflector," Antennas and Propagation Society International Symposium, pp. 88–91, 1990.
- [7] Pozar, D.M., "Flat lens antenna concept using aperture coupled microstrip patches," *Electronics Letters*, Vol. 32, Issue 23, pp. 2109–2111, 1996.
- [8] Jalaly, I., Robertson, I.D., "RF barcodes using multiple frequency bands," IEEE MTT-S International Microwave Symposium Digest, pp. 139-142, 2005
- [9] Website. Retrieved 11-20-2013. [http://en.wikipedia.org/wiki/F-117\\_Nighthawk](http://en.wikipedia.org/wiki/F-117_Nighthawk)
- [10] Website. Retrieved 11-20-2013. [http://orbitaldebris.jsc.nasa.gov/measure/images/radar\\_dome.jpg](http://orbitaldebris.jsc.nasa.gov/measure/images/radar_dome.jpg)
- [11] Pugh, S., "Investigating the Use of Frequency Selective Surfaces in High Power Microwave Applications", DTIC Document, 2010.
- [12] Mesyats, G., *Pulsed Power*, Springer, New York, 2005
- [13] Edmiston G., Krile J., Neuber, A., Dickens, J., Krompholz, H., "High Power Microwave Surface Flashover of a Gas-Dielectric Interface at 90 to 760 Torr", *Pulsed Power Conference*, 2005 IEEE, vol., no., pp.350,353, 13-17, 2005
- [14] Li, M. and Behdad N., "Frequency Selective Surfaces for Pulsed High-Power Microwave Applications", *IEEE Trans on Ant. and Prop.*, Vol. 61, No. 2, 2013
- [15] Tan, Z.M., McDonald, K.T., "Babinet's Principle for Electromagnetic Fields" *Joseph Henry Laboratories, Princeton University, Princeton, NJ*, 2012.
- [16] Pagano, N.J., *Composite Materials Series Volume 5 "Interlaminar Response of Composite Materials"*, Elsevier Science Publishers B.V. New York, 1989
- [17] Asp, L.E., "The effects of moisture and temperature on the interlaminar delamination toughness of a carbon/epoxy composite", *Composites Science and Technology*, Volume 58, Issue 6, 1998.
- [18] Hill, K.O. and Meltz, G., "Fiber Bragg Grating Technology Fundamentals and Overview", *Journal of Lightwave Technology*, Vol. 15, No. 8, 1997.

- [19] Petrov, V.M. and Gagulin, V.V., "Microwave Absorbing Materials", Inorganic Materials, Vol. 37, Issue 2, 2001.
- [20] Magnusson, R., Wang, S.S., "New principle for optical filters," Appl. Phys. Lett. 61(9), pp. 1022–1024, 1992.
- [21] Tibuleac, S., Magnusson, R., "Reflection and transmission guided-mode resonance filters," J. Opt. Soc. Am A 14(7), pp. 1617–1626, 1997.
- [22] Boonruang, S. Greenwel, A. I, Moharam, M.G., "Multiline two-dimensional guided-mode resonant filters," Appl. Opt. 45(22), pp. 5740–5747, 2006.
- [23] Barton, J.H., Rumpf, R.C., Smith, R.W., Kozikowski, C.L., and Zellner, P.A., 'All-Dielectric Frequency Selective Surfaces with Few Number of Periods', Progress In Electromagnetics Research B, 41, pp. 269-283, 2012.
- [24] Lord Rayleigh, Proc. R. Soc. Lond. A 79, pp. 399–416, 1907.
- [25] Rumpf, R.C., Design and Optimization of Nano-Optical Elements by Coupling Fabrication to Optical Behavior, Ph.D. Thesis, University of Central Florida, 2006.
- [26] Balanis, C., *Advanced Engineering Electromagnetics*, pp. 323–325, Wiley, New York, NY, 1989.
- [27] Boyce, R. R., Kostuk, R.K., "Investigation of the effect of finite grating size on the performance of guided-mode resonance filters," Appl. Opt. 39(21), pp. 3649–3653, 2000.
- [28] Taylor, J.D., *Introduction to Ultra-Wideband Radar Systems*, Boca Raton, FL: CRC Press, 1995.
- [29] Costa, F., Monorchio, A., "A Frequency Selective Radome With Wideband Absorbing Properties," Antennas and Propagation, IEEE Transactions on, vol.60, no.6, pp.2740,2747, 2012.
- [30] Genovesi, S., Costa, F., Monorchio, A. "Wideband Radar Cross Section Reduction of Slot Antennas Arrays", Antennas and Propagation, IEEE Transactions on, pp. 163 - 173 vol. 62, no. 1, 2014.
- [31] Sadiku, M. N. O., *Numerical Techniques in Electromagnetics*. Boca Raton, FL: CRC Press, 2001.
- [32] Sun, W., Liu, K., and Balanis, A., "Analysis of Singly and Doubly Periodic Absorbers by Frequeuncy-Domain Finite-Difference Method," IEEE Trans. Antennas and Propagation, vol. 44, pp. 798-805, 1996.
- [33] Wu, S. and Glytsis, N., "Volume holographic grating couplers: rigorous analysis by use of the finite-difference frequency-domain method," Appl. Opt., vol. 43, pp. 1009-1023, 2004.
- [34] Rappaport, C. M. and McCartin, B. J., "FDFD Analysis of Electromagnetic Scattering in Anisotropic Media Using Unconstrained Triangular Meshes," IEEE Trans. Antennas and Propagation, vol. 39, pp. 345-349, 1991.
- [35] Sewell, G., *Computational Methods of Linear Algebra*, 2<sup>nd</sup> Edition, Wily, New York, 2005.
- [36] Rumpf, R.C., "Computational Electromagnetics (CEM): Lecture Series", University of Texas at El Paso, 2011.

- [37] Yee, K. S., "Numerical solution of the initial boundary value problems involving Maxwell's equations in isotropic media," IEEE Trans. Microwave Theory and Techniques, vol. 44, pp. 61–69, 1998.
- [38] Taflove, A. and Hagness, S. C., *Computational Electrodynamics: The Finite-Difference Time-Domain Method*, 2nd Edition. Norwood, MA: Artech House, Inc., 2000.
- [39] Chapra, S., Canale, R., *Numerical Methods for Engineers*, 6<sup>th</sup> Edition, McGraw-Hill, 2009
- [40] Joannopoulos, J. D., Meade, R. D., and Winn, J. N., *Photonic Crystals: Modeling the flow of light*. New Jersey: Princeton University Press, 1995.
- [41] Riley, K.F., Hobson, M.P., and Bence, S.J., *Mathematical Methods for Scientists and Engineers*, Cambridge University Press, 2002.
- [42] Jackson, J.D., *Classical Electrodynamics*, 3<sup>rd</sup> Edition, Wiley, New York, 1998
- [43] Rumpf, R. C., "Simple implementation of arbitrarily shaped total-field/scattered-field regions in finite-difference frequency-domain," PIERS B, Vol. 36, 221-248, 2012.
- [44] Shiesser, W.E., *The Numerical Method of Lines*, Academic Press, 1991.
- [45] Helfert, S. F. and Pregla, R., "The method of lines: A versatile tool for the analysis of waveguide structures," Electromagnetics, Vol. 22, 615{637, Taylor & Francis, New York, 2002
- [46] Highman, N.J., *Functions of Matrices*, Siam, Philadelphia, 2008
- [47] Pozar, D.M., *Microwave Engineering*, 4<sup>th</sup> Edition, Wiley, New York, 2011.
- [48] Moharam, M. G., D. A. Pommet, E. B. Grann, and T. K. Gaylord, "Stable implementation of the rigorous coupled-wave analysis for surface-relief gratings: Enhanced transmittance matrix approach," J. Opt. Soc. Am. A, Vol. 12, No. 5, 1077-1086, 1995
- [49] Rumpf, R. C., "Improved formulation of scattering matrices for semi-analytical methods that is consistent with convention," PIERS B, Vol. 35, 241-261, 2011.
- [50] Tervo, J., M. Kuittinen, P. Vahimaa, J. Turunen, T. Aalto, P. Heimala, and M. Leppihalme, "Efficient bragg waveguide-grating analysis by quasi-rigorous approach based on redheffer's star product," Optics Commun., Vol. 198, 265{272, 2001.
- [51] Redheffer, R., "Difference equations and functional equations in transmission-line theory," Modern Mathematics for the Engineer, E. F. Beckenbach, ed., Vol. 12, 282{337, McGraw-Hill, New York, 1961.
- [52] Perigal, H. "On Geometric Dissections and Transformations." *Messenger Math.* 2, 103-106, 1873.
- [53] Moharam, M. G., E. B. Grann, D. A. Pommet, and T. K. Gaylord, "Formulation for stable and efficient implementation of the rigorous coupled-wave analysis of binary grating," J. Opt. Soc. Am. A, Vol. 12, No. 5, 1995.
- [54] Apostol, T.M., *Mathematical Analysis*, 2<sup>nd</sup> Edition, Addison Wesley, Boston M.A., 1974
- [55] Gibbs, J.W., "Fourier Series", Nature 59 (1522): 200, 1898.

- [56] Robinson, J. and Rahmat-Samii, Y., 'Particle Swarm Optimization in Electromagnetics', *Antennas and Propagation, IEEE Transactions on*, , 52, (2), pp. 397-407, 2004
- [57] Kennedy, J. "Particle swarm: social adaptation of knowledge". *Proceedings of IEEE International Conference on Evolutionary Computation*, 1997.
- [58] Poli, R., "An analysis of publications on particle swarm optimization application", Technical Report CSM-469, Department of Computer Science, University of Essex, UK, 2007.
- [59] Fraser, A. S. "Simulation of Genetic Systems by Automatic Digital Computers. I. Introduction". *Australian Journal of Biological Sciences*, 1957.
- [60] Banzhaf, W., Nordin, P., Keller, R., Francone, F., *Genetic Programming – An Introduction*, San Francisco, CA: Morgan Kaufmann, 1998.
- [61] Beasley, D., Martin, R.R., Bull D.R., "An overview of genetic algorithms: Part 1. Fundamentals", *University computing*, 1993.
- [62] Magnusson, R., Shokooh-Saremi, M., "Physical basis for wideband resonant reflectors," *Opt. Express* 16(5), 3456–3462, 2008.
- [63] Hao, J., Zhou, L., "Electromagnetic wave scatterings by anisotropic metamaterials: Generalized 4x4 transfer-matrix method," *Phys. Rev. B*. 77, 094201, 2008.
- [64] Grann, E.B., Moharam, M.G., Pommet, D.A., "Artificial uniaxial and biaxial dielectrics with use of two-dimensional subwavelength binary gratings," *J. Opt. Soc. Am. A* 11(10), pp. 2695–2703, 1994.
- [65] Kintaka, K., Majima, T., Hatanaka, K., Inoue, J., and Ura, S., 'Polarization-Independent Guided-Mode Resonance Filter with Cross-Integrated Waveguide Resonators', *Optics Letters*, 37, (15), pp. 3264-3266, 2012.
- [66] Barton, J.H., Garcia, C.R., Berry E.A., May R.G., Gray D.T., Rumpf R.C., "All-Dielectric Frequency Selective Surface for High Power Microwaves", *Antennas and Propagation, IEEE Transactions on*, Vol. 62, No. 07, 2014.
- [67] Duhamel, P. and Vetterli, M., *Fast Fourier transforms: A tutorial review and a state of the art*, *Signal Processing* 19, 1990, pp. 259–299
- [68] Auslander, L., Feig, E. and Winograd, S., "New algorithms for the multidimensional Fourier transform", *IEEE Trans. Acoust. Speech Signal Process.*, Vol. ASSP-31, No. 2, pp. 338-403, 1983.
- [69] Fowles, G. R. *Introduction to Modern Optics*. New York: Dover, 1989.
- [70] Jacobs, P.F., "Fundamentals of Stereolithography", *Solid Freeform Fabrication Proceedings*, pp., 196-211, 1992.
- [71] Richter, J., and Jacobs, P.F., "The Present State of Accuracy in Stereolithography", *Conference Proceedings, Second International Conference on Rapid Prototyping*, University of Dayton, Dayton, Ohio pp. 269-294, 1991.
- [72] Rumpf, R. C., Gates, M., Kozikowski, C. L., Davis, W. A., "Guided-Mode Resonance Filter Compensated to Operate on a Curved Surface," *PIER C*, Vol. 40, pp. 93-103, 2013.

- [73] Rumpf, R. C., Pazos, J., "Synthesis of Spatially Variant Lattices," Opt. Express, Vol. 20, Issue 14, pp. 15263-15274 2012.

## Appendix

### A1: Normalization of the magnetic field component.

Below is shown the arithmetic behind the normalization of the  $\vec{H}$  field used in all the computational methods used in this work.

$$\begin{aligned}
 \nabla \times \vec{E} &= -j\omega[\mu]\vec{H} \\
 \nabla \times \vec{E} &= -j\omega\mu_0[\mu_r]\vec{H} \\
 \nabla \times \vec{E} &= -j\omega\mu_0[\mu_r]\left(-\frac{1}{j}\frac{\sqrt{\varepsilon_0}}{\sqrt{\mu_0}}\tilde{H}\right) \\
 \nabla \times \vec{E} &= (-1)(-1)\frac{j}{j}\omega\mu_0[\mu_r]\left(\frac{\sqrt{\varepsilon_0}}{\sqrt{\mu_0}}\tilde{H}\right) \\
 \nabla \times \vec{E} &= \omega\frac{\mu_0}{\sqrt{\mu_0}}\sqrt{\varepsilon_0}[\mu_r]\tilde{H} \\
 \nabla \times \vec{E} &= \omega\frac{\mu_0}{\sqrt{\mu_0}}\sqrt{\varepsilon_0}[\mu_r]\tilde{H} \\
 \nabla \times \vec{E} &= \omega\frac{\sqrt{\mu_0}}{\sqrt{\mu_0}}\frac{1}{\sqrt{\mu_0}}\mu_0\sqrt{\varepsilon_0}[\mu_r]\tilde{H} \\
 \nabla \times \vec{E} &= \omega\frac{\sqrt{\mu_0}}{\mu_0}\mu_0\sqrt{\varepsilon_0}[\mu_r]\tilde{H} \\
 \nabla \times \vec{E} &= \omega\sqrt{\mu_0}\sqrt{\varepsilon_0}[\mu_r]\tilde{H} \\
 \nabla \times \vec{E} &= \omega\sqrt{\mu_0\varepsilon_0}[\mu_r]\tilde{H} \\
 \nabla \times \vec{E} &= \omega\sqrt{\mu_0\varepsilon_0}[\mu_r]\tilde{H} \\
 \boxed{\nabla \times \vec{E} &= k_0[\mu_r]\tilde{H}}
 \end{aligned}$$

$$\begin{aligned}
 \nabla \times \vec{H} &= j\omega[\varepsilon]\vec{E} \\
 \nabla \times \vec{H} &= j\omega\varepsilon_0[\varepsilon_r]\vec{E} \\
 \nabla \times \left(-\frac{1}{j}\frac{\sqrt{\varepsilon_0}}{\sqrt{\mu_0}}\tilde{H}\right) &= j\omega\varepsilon_0[\varepsilon_r]\vec{E} \\
 -\frac{1}{j}\frac{\sqrt{\varepsilon_0}}{\sqrt{\mu_0}}(\nabla \times \tilde{H}) &= j\omega\varepsilon_0[\varepsilon_r]\vec{E} \\
 (-j) - \frac{1}{j}\frac{\sqrt{\varepsilon_0}}{\sqrt{\mu_0}}(\nabla \times \tilde{H}) &= (-j)j\omega\varepsilon_0[\varepsilon_r]\vec{E} \\
 \nabla \times \tilde{H} &= \omega\varepsilon_0\frac{\sqrt{\mu_0}}{\sqrt{\varepsilon_0}}[\varepsilon_r]\vec{E} \\
 \nabla \times \tilde{H} &= \omega\varepsilon_0\frac{\sqrt{\varepsilon_0}}{\sqrt{\varepsilon_0}}\frac{1}{\sqrt{\varepsilon_0}}\sqrt{\mu_0}[\varepsilon_r]\vec{E} \\
 \nabla \times \tilde{H} &= \omega\varepsilon_0\frac{1}{\varepsilon_0}\sqrt{\varepsilon_0}\sqrt{\mu_0}[\varepsilon_r]\vec{E} \\
 \nabla \times \tilde{H} &= \omega\sqrt{\varepsilon_0\mu_0}[\varepsilon_r]\vec{E} \\
 \boxed{\nabla \times \tilde{H} &= k_0[\varepsilon_r]\vec{E}}
 \end{aligned}$$

## A2: Example derivative operator matrices with periodic boundary conditions

Below is shown a 3x3 matrix derivative operator with periodic boundary conditions.

$$\mathbf{D}_x^E \mathbf{E} = \frac{1}{\Delta x'} = \begin{bmatrix} -1 & 1 & 0 & 0 & 0 & 0 & 0 & 0 & 0 \\ 0 & -1 & 1 & 0 & 0 & 0 & 0 & 0 & 0 \\ e^{j\beta\Lambda_x} & 0 & -1 & 0 & 0 & 0 & 0 & 0 & 0 \\ 0 & 0 & 0 & -1 & 1 & 0 & 0 & 0 & 0 \\ 0 & 0 & 0 & 0 & -1 & 1 & 0 & 0 & 0 \\ 0 & 0 & 0 & e^{j\beta\Lambda_x} & 0 & -1 & 0 & 0 & 0 \\ 0 & 0 & 0 & 0 & 0 & 0 & -1 & 1 & 0 \\ 0 & 0 & 0 & 0 & 0 & 0 & 0 & -1 & 1 \\ 0 & 0 & 0 & 0 & 0 & 0 & e^{j\beta\Lambda_x} & 0 & -1 \end{bmatrix}$$

$$\mathbf{D}_y^E \mathbf{E} = \frac{1}{\Delta y'} = \begin{bmatrix} -1 & 0 & 0 & 1 & 0 & 0 & 0 & 0 & 0 \\ 0 & -1 & 0 & 0 & 1 & 0 & 0 & 0 & 0 \\ 0 & 0 & -1 & 0 & 0 & 1 & 0 & 0 & 0 \\ 0 & 0 & 0 & -1 & 0 & 0 & 1 & 0 & 0 \\ 0 & 0 & 0 & 0 & -1 & 0 & 0 & 1 & 0 \\ 0 & 0 & 0 & 0 & 0 & -1 & 0 & 0 & 1 \\ e^{j\beta\Lambda_x} & 0 & 0 & 0 & 0 & 0 & -1 & 0 & 0 \\ 0 & e^{j\beta\Lambda_x} & 0 & 0 & 0 & 0 & 0 & -1 & 0 \\ 0 & 0 & e^{j\beta\Lambda_x} & 0 & 0 & 0 & 0 & 0 & -1 \end{bmatrix}$$

$$\mathbf{D}_x^H \mathbf{E} = \frac{1}{\Delta x'} = \begin{bmatrix} 1 & 0 & e^{j\beta\Lambda_x} & 0 & 0 & 0 & 0 & 0 & 0 \\ -1 & 1 & 0 & 0 & 0 & 0 & 0 & 0 & 0 \\ 0 & -1 & 1 & 0 & 0 & 0 & 0 & 0 & 0 \\ 0 & 0 & 0 & 1 & 0 & e^{j\beta\Lambda_x} & 0 & 0 & 0 \\ 0 & 0 & 0 & -1 & 1 & 0 & 0 & 0 & 0 \\ 0 & 0 & 0 & 0 & -1 & 1 & 0 & 0 & 0 \\ 0 & 0 & 0 & 0 & 0 & 0 & 1 & 0 & e^{j\beta\Lambda_x} \\ 0 & 0 & 0 & 0 & 0 & 0 & -1 & 1 & 0 \\ 0 & 0 & 0 & 0 & 0 & 0 & 0 & -1 & 1 \end{bmatrix}$$

$$\mathbf{D}_y^H \mathbf{E} = \frac{1}{\Delta y'} \begin{bmatrix} 1 & 0 & 0 & 0 & 0 & 0 & e^{j\beta\Lambda_x} & 0 & 0 \\ 0 & 1 & 0 & 0 & 0 & 0 & 0 & e^{j\beta\Lambda_x} & 0 \\ 0 & 0 & 1 & 0 & 0 & 0 & 0 & 0 & e^{j\beta\Lambda_x} \\ -1 & 0 & 0 & 1 & 0 & 0 & 0 & 0 & 0 \\ 0 & -1 & 0 & 0 & 1 & 0 & 0 & 0 & 0 \\ 0 & 0 & -1 & 0 & 0 & 1 & 0 & 0 & 0 \\ 0 & 0 & 0 & -1 & 0 & 0 & 1 & 0 & 0 \\ 0 & 0 & 0 & 0 & -1 & 0 & 0 & 1 & 0 \\ 0 & 0 & 0 & 0 & 0 & -1 & 0 & 0 & 1 \end{bmatrix}$$

### A3: Derivation of the 2D FDFD wave equations

First the required field components are solved for:

$$\begin{aligned}
 \mathbf{D}_y^E \mathbf{E}_z &= \boldsymbol{\mu}_{xx} \tilde{\mathbf{H}}_x & -\mathbf{D}_x^E \mathbf{E}_z &= \boldsymbol{\mu}_{yy} \tilde{\mathbf{H}}_y & \mathbf{D}_y^H \tilde{\mathbf{H}}_z &= \boldsymbol{\varepsilon}_{xx} \mathbf{E}_x & -\mathbf{D}_x^H \tilde{\mathbf{H}}_z &= \boldsymbol{\varepsilon}_{yy} \mathbf{E}_y \\
 \boldsymbol{\mu}_{xx}^{-1} \mathbf{D}_y^E \mathbf{E}_z &= \boldsymbol{\mu}_{xx}^{-1} \boldsymbol{\mu}_{xx} \tilde{\mathbf{H}}_x & -\boldsymbol{\mu}_{yy}^{-1} \mathbf{D}_x^E \mathbf{E}_z &= \boldsymbol{\mu}_{yy}^{-1} \boldsymbol{\mu}_{yy} \tilde{\mathbf{H}}_y & \boldsymbol{\varepsilon}_{xx}^{-1} \mathbf{D}_y^H \tilde{\mathbf{H}}_z &= \boldsymbol{\varepsilon}_{xx}^{-1} \boldsymbol{\varepsilon}_{xx} \mathbf{E}_x & -\boldsymbol{\varepsilon}_{yy}^{-1} \mathbf{D}_x^H \tilde{\mathbf{H}}_z &= \boldsymbol{\varepsilon}_{yy}^{-1} \boldsymbol{\varepsilon}_{yy} \mathbf{E}_y \\
 \boxed{\tilde{\mathbf{H}}_x &= \boldsymbol{\mu}_{xx}^{-1} \mathbf{D}_y^E \mathbf{E}_z} & \boxed{\tilde{\mathbf{H}}_y &= -\boldsymbol{\mu}_{yy}^{-1} \mathbf{D}_x^E \mathbf{E}_z} & \boxed{\mathbf{E}_x &= \boldsymbol{\varepsilon}_{xx}^{-1} \mathbf{D}_y^H \tilde{\mathbf{H}}_z} & \boxed{\mathbf{E}_y &= -\boldsymbol{\varepsilon}_{yy}^{-1} \mathbf{D}_x^H \tilde{\mathbf{H}}_z}
 \end{aligned}$$

Next these equations are plugged into their respected mode equations.

$\mathbf{E}_z$  Mode

$$\begin{aligned}
 \mathbf{D}_x^H \tilde{\mathbf{H}}_y - \mathbf{D}_y^H \tilde{\mathbf{H}}_x &= \boldsymbol{\varepsilon}_{zz} \mathbf{E}_z \\
 \mathbf{D}_x^H \left( -\boldsymbol{\mu}_{yy}^{-1} \mathbf{D}_x^E \mathbf{E}_z \right) - \mathbf{D}_y^H \left( \boldsymbol{\mu}_{xx}^{-1} \mathbf{D}_y^E \mathbf{E}_z \right) &= \boldsymbol{\varepsilon}_{zz} \mathbf{E}_z \\
 -\mathbf{D}_x^H \boldsymbol{\mu}_{yy}^{-1} \mathbf{D}_x^E \mathbf{E}_z - \mathbf{D}_y^H \boldsymbol{\mu}_{xx}^{-1} \mathbf{D}_y^E \mathbf{E}_z &= \boldsymbol{\varepsilon}_{zz} \mathbf{E}_z \\
 (-1) \left( -\mathbf{D}_x^H \boldsymbol{\mu}_{yy}^{-1} \mathbf{D}_x^E \mathbf{E}_z - \mathbf{D}_y^H \boldsymbol{\mu}_{xx}^{-1} \mathbf{D}_y^E \mathbf{E}_z \right) &= (-1) \boldsymbol{\varepsilon}_{zz} \mathbf{E}_z \\
 \mathbf{D}_x^H \boldsymbol{\mu}_{yy}^{-1} \mathbf{D}_x^E \mathbf{E}_z + \mathbf{D}_y^H \boldsymbol{\mu}_{xx}^{-1} \mathbf{D}_y^E \mathbf{E}_z &= -\boldsymbol{\varepsilon}_{zz} \mathbf{E}_z \\
 \mathbf{D}_x^H \boldsymbol{\mu}_{yy}^{-1} \mathbf{D}_x^E \mathbf{E}_z + \mathbf{D}_y^H \boldsymbol{\mu}_{xx}^{-1} \mathbf{D}_y^E \mathbf{E}_z + \boldsymbol{\varepsilon}_{zz} \mathbf{E}_z &= 0 \\
 \boxed{\left( \mathbf{D}_x^H \boldsymbol{\mu}_{yy}^{-1} \mathbf{D}_x^E + \mathbf{D}_y^H \boldsymbol{\mu}_{xx}^{-1} \mathbf{D}_y^E + \boldsymbol{\varepsilon}_{zz} \right) \mathbf{E}_z = 0}
 \end{aligned}$$

$\mathbf{H}_z$  Mode

$$\begin{aligned}
 \mathbf{D}_x^E \mathbf{E}_y - \mathbf{D}_y^E \mathbf{E}_x &= \boldsymbol{\mu}_{zz} \tilde{\mathbf{H}}_z \\
 \mathbf{D}_x^E \left( -\boldsymbol{\varepsilon}_{yy}^{-1} \mathbf{D}_x^H \tilde{\mathbf{H}}_z \right) - \mathbf{D}_y^E \left( \boldsymbol{\varepsilon}_{xx}^{-1} \mathbf{D}_y^H \tilde{\mathbf{H}}_z \right) &= \boldsymbol{\mu}_{zz} \tilde{\mathbf{H}}_z \\
 -\mathbf{D}_x^E \boldsymbol{\varepsilon}_{yy}^{-1} \mathbf{D}_x^H \tilde{\mathbf{H}}_z - \mathbf{D}_y^E \boldsymbol{\varepsilon}_{xx}^{-1} \mathbf{D}_y^H \tilde{\mathbf{H}}_z &= \boldsymbol{\mu}_{zz} \tilde{\mathbf{H}}_z \\
 (-1) \left( -\mathbf{D}_x^E \boldsymbol{\varepsilon}_{yy}^{-1} \mathbf{D}_x^H \tilde{\mathbf{H}}_z - \mathbf{D}_y^E \boldsymbol{\varepsilon}_{xx}^{-1} \mathbf{D}_y^H \tilde{\mathbf{H}}_z \right) &= (-1) \boldsymbol{\mu}_{zz} \tilde{\mathbf{H}}_z \\
 \mathbf{D}_x^E \boldsymbol{\varepsilon}_{yy}^{-1} \mathbf{D}_x^H \tilde{\mathbf{H}}_z + \mathbf{D}_y^E \boldsymbol{\varepsilon}_{xx}^{-1} \mathbf{D}_y^H \tilde{\mathbf{H}}_z &= -\boldsymbol{\mu}_{zz} \tilde{\mathbf{H}}_z \\
 \mathbf{D}_x^E \boldsymbol{\varepsilon}_{yy}^{-1} \mathbf{D}_x^H \tilde{\mathbf{H}}_z + \mathbf{D}_y^E \boldsymbol{\varepsilon}_{xx}^{-1} \mathbf{D}_y^H \tilde{\mathbf{H}}_z + \boldsymbol{\mu}_{zz} \tilde{\mathbf{H}}_z &= 0 \\
 \boxed{\left( \mathbf{D}_x^E \boldsymbol{\varepsilon}_{yy}^{-1} \mathbf{D}_x^H + \mathbf{D}_y^E \boldsymbol{\varepsilon}_{xx}^{-1} \mathbf{D}_y^H + \boldsymbol{\mu}_{zz} \right) \tilde{\mathbf{H}}_z = 0}
 \end{aligned}$$



### A5: Derivation of the scattering matrix terms

From Eq. (1.4.33) we see that an inverse matrix operation needs to be performed of the block matrices in this equation. It is known from basic linear algebra that the inverse of matrix can take on the following form:

$$\mathbf{A} \begin{bmatrix} a_{11} & a_{12} \\ a_{21} & a_{22} \end{bmatrix}^{-1} = \frac{1}{\det(\mathbf{A})} \begin{bmatrix} a_{22} & -a_{12} \\ -a_{21} & a_{11} \end{bmatrix}$$

This formula is applied the inverse term in Eq. (1.4.35).

$$\mathbf{W} \begin{bmatrix} \mathbf{W}_i & \mathbf{W}_i \\ -\mathbf{V}_i & \mathbf{V}_i \end{bmatrix}^{-1} = \frac{1}{\det(\mathbf{W})} \begin{bmatrix} \mathbf{V}_i & -\mathbf{W}_i \\ \mathbf{V}_i & \mathbf{W}_i \end{bmatrix} \quad | \quad \frac{1}{\det(\mathbf{W})} = \frac{1}{\mathbf{V}_i \mathbf{W}_i - -\mathbf{W}_i \mathbf{V}_i}$$

$$\begin{aligned} \mathbf{W}^{-1} &= \frac{1}{\mathbf{V}_i \mathbf{W}_i + \mathbf{W}_i \mathbf{V}_i} \begin{bmatrix} \mathbf{V}_i & -\mathbf{W}_i \\ \mathbf{V}_i & \mathbf{W}_i \end{bmatrix} \\ \mathbf{W}^{-1} &= \begin{bmatrix} \frac{\mathbf{V}_i}{\mathbf{V}_i \mathbf{W}_i + \mathbf{W}_i \mathbf{V}_i} & \frac{-\mathbf{W}_i}{\mathbf{V}_i \mathbf{W}_i + \mathbf{W}_i \mathbf{V}_i} \\ \frac{\mathbf{V}_i}{\mathbf{V}_i \mathbf{W}_i + \mathbf{W}_i \mathbf{V}_i} & \frac{\mathbf{W}_i}{\mathbf{V}_i \mathbf{W}_i + \mathbf{W}_i \mathbf{V}_i} \end{bmatrix} \\ \mathbf{W}^{-1} &= \begin{bmatrix} \frac{\mathbf{V}_i}{\mathbf{V}_i (\mathbf{W}_i + \mathbf{W}_i)} & \frac{-\mathbf{W}_i}{\mathbf{W}_i (\mathbf{V}_i + \mathbf{V}_i)} \\ \frac{\mathbf{V}_i}{\mathbf{V}_i (\mathbf{W}_i + \mathbf{W}_i)} & \frac{\mathbf{W}_i}{\mathbf{W}_i (\mathbf{V}_i + \mathbf{V}_i)} \end{bmatrix} \\ \mathbf{W}^{-1} &= \begin{bmatrix} \frac{1}{2\mathbf{W}_i} & -\frac{1}{2\mathbf{V}_i} \\ \frac{1}{2\mathbf{W}_i} & \frac{1}{2\mathbf{V}_i} \end{bmatrix} \\ \mathbf{W}^{-1} &= \frac{1}{2} \begin{bmatrix} \mathbf{W}_i^{-1} & -\mathbf{V}_i^{-1} \\ \mathbf{W}_i^{-1} & \mathbf{V}_i^{-1} \end{bmatrix} \end{aligned}$$

From here the  $\mathbf{W}^{-1}\mathbf{W}$  is calculated.

$$\begin{aligned}
& \frac{1}{2} \begin{bmatrix} \mathbf{W}_i^{-1} & -\mathbf{V}_i^{-1} \\ \mathbf{W}_i^{-1} & \mathbf{V}_i^{-1} \end{bmatrix} \begin{bmatrix} \mathbf{W}_j & \mathbf{W}_j \\ -\mathbf{V}_j & \mathbf{V}_j \end{bmatrix} \\
& \frac{1}{2} \begin{bmatrix} \mathbf{W}_i^{-1}\mathbf{W}_j + -\mathbf{V}_i^{-1} - \mathbf{V}_j & \mathbf{W}_i^{-1}\mathbf{W}_j + -\mathbf{V}_i^{-1}\mathbf{V}_j \\ \mathbf{W}_i^{-1}\mathbf{W}_j + \mathbf{V}_i^{-1} - \mathbf{V}_j & \mathbf{W}_i^{-1}\mathbf{W}_j + -\mathbf{V}_i^{-1}\mathbf{V}_j \end{bmatrix} \\
& \frac{1}{2} \begin{bmatrix} \mathbf{W}_i^{-1}\mathbf{W}_j + \mathbf{V}_i^{-1}\mathbf{V}_j & \mathbf{W}_i^{-1}\mathbf{W}_j - \mathbf{V}_i^{-1}\mathbf{V}_j \\ \mathbf{W}_i^{-1}\mathbf{W}_j - \mathbf{V}_i^{-1}\mathbf{V}_j & \mathbf{W}_i^{-1}\mathbf{W}_j + \mathbf{V}_i^{-1}\mathbf{V}_j \end{bmatrix} \\
& \boxed{\begin{bmatrix} \mathbf{A}_{ij} & \mathbf{B}_{ij} \\ \mathbf{B}_{ij} & \mathbf{A}_{ij} \end{bmatrix} \quad \begin{aligned} \mathbf{A}_{ij} &= \mathbf{W}_i^{-1}\mathbf{W}_j + \mathbf{V}_i^{-1}\mathbf{V}_j \\ \mathbf{B}_{ij} &= \mathbf{W}_i^{-1}\mathbf{W}_j - \mathbf{V}_i^{-1}\mathbf{V}_j \end{aligned}}
\end{aligned}$$

At this point the derivation of the scattering parameters begin with Eq. (1.4.38). The propagation terms of this equation can be simplified the following way, effectively getting rid of the inverse propagation terms:

$$\begin{aligned}
& \frac{1}{2} \begin{bmatrix} \mathbf{A}_{i1} & \mathbf{B}_{i1} \\ \mathbf{B}_{i1} & \mathbf{A}_{i1} \end{bmatrix} \begin{bmatrix} \mathbf{c}_1^+ \\ \mathbf{c}_1^- \end{bmatrix} = \frac{1}{2} \begin{bmatrix} \mathbf{X}_i^{-1} & \mathbf{0} \\ \mathbf{0} & \mathbf{X}_i \end{bmatrix} \begin{bmatrix} \mathbf{A}_{i2} & \mathbf{B}_{i2} \\ \mathbf{B}_{i2} & \mathbf{A}_{i2} \end{bmatrix} \begin{bmatrix} \mathbf{c}_2^+ \\ \mathbf{c}_2^- \end{bmatrix} \\
& \frac{1}{2} \begin{bmatrix} \mathbf{A}_{i1} & \mathbf{B}_{i1} \\ \mathbf{B}_{i1} & \mathbf{A}_{i1} \end{bmatrix} \begin{bmatrix} \mathbf{c}_1^+ \\ \mathbf{c}_1^- \end{bmatrix} = \frac{1}{2} \begin{bmatrix} \mathbf{X}_i^{-1} & \mathbf{0} \\ \mathbf{0} & \mathbf{I} \end{bmatrix} \begin{bmatrix} \mathbf{I} & \mathbf{0} \\ \mathbf{0} & \mathbf{X}_i \end{bmatrix} \begin{bmatrix} \mathbf{A}_{i2} & \mathbf{B}_{i2} \\ \mathbf{B}_{i2} & \mathbf{A}_{i2} \end{bmatrix} \begin{bmatrix} \mathbf{c}_2^+ \\ \mathbf{c}_2^- \end{bmatrix} \\
& \frac{1}{2} \begin{bmatrix} \mathbf{X}_i & \mathbf{0} \\ \mathbf{0} & \mathbf{I} \end{bmatrix} \begin{bmatrix} \mathbf{A}_{i1} & \mathbf{B}_{i1} \\ \mathbf{B}_{i1} & \mathbf{A}_{i1} \end{bmatrix} \begin{bmatrix} \mathbf{c}_1^+ \\ \mathbf{c}_1^- \end{bmatrix} = \frac{1}{2} \begin{bmatrix} \mathbf{I} & \mathbf{0} \\ \mathbf{0} & \mathbf{X}_i \end{bmatrix} \begin{bmatrix} \mathbf{A}_{i2} & \mathbf{B}_{i2} \\ \mathbf{B}_{i2} & \mathbf{A}_{i2} \end{bmatrix} \begin{bmatrix} \mathbf{c}_2^+ \\ \mathbf{c}_2^- \end{bmatrix}
\end{aligned}$$

Linear algebra is then performed on this equation simplifying and removing it from block matrix form.

$$\begin{aligned}
\frac{1}{2} \begin{bmatrix} \mathbf{X}_i & \mathbf{0} \\ \mathbf{0} & \mathbf{I} \end{bmatrix} \begin{bmatrix} \mathbf{A}_{i1} & \mathbf{B}_{i1} \\ \mathbf{B}_{i1} & \mathbf{A}_{i1} \end{bmatrix} \begin{bmatrix} \mathbf{c}_1^{++} \\ \mathbf{c}_1^{--} \end{bmatrix} &= \frac{1}{2} \begin{bmatrix} \mathbf{I} & \mathbf{0} \\ \mathbf{0} & \mathbf{X}_i \end{bmatrix} \begin{bmatrix} \mathbf{A}_{i2} & \mathbf{B}_{i2} \\ \mathbf{B}_{i2} & \mathbf{A}_{i2} \end{bmatrix} \begin{bmatrix} \mathbf{c}_2^{++} \\ \mathbf{c}_2^{--} \end{bmatrix} \\
2 \left( \frac{1}{2} \begin{bmatrix} \mathbf{X}_i & \mathbf{0} \\ \mathbf{0} & \mathbf{I} \end{bmatrix} \begin{bmatrix} \mathbf{A}_{i1} & \mathbf{B}_{i1} \\ \mathbf{B}_{i1} & \mathbf{A}_{i1} \end{bmatrix} \begin{bmatrix} \mathbf{c}_1^{++} \\ \mathbf{c}_1^{--} \end{bmatrix} \right) &= \frac{1}{2} \begin{bmatrix} \mathbf{I} & \mathbf{0} \\ \mathbf{0} & \mathbf{X}_i \end{bmatrix} \begin{bmatrix} \mathbf{A}_{i2} & \mathbf{B}_{i2} \\ \mathbf{B}_{i2} & \mathbf{A}_{i2} \end{bmatrix} \begin{bmatrix} \mathbf{c}_2^{++} \\ \mathbf{c}_2^{--} \end{bmatrix} \\
\begin{bmatrix} \mathbf{X}_i & \mathbf{0} \\ \mathbf{0} & \mathbf{I} \end{bmatrix} \begin{bmatrix} \mathbf{A}_{i1} & \mathbf{B}_{i1} \\ \mathbf{B}_{i1} & \mathbf{A}_{i1} \end{bmatrix} \begin{bmatrix} \mathbf{c}_1^{++} \\ \mathbf{c}_1^{--} \end{bmatrix} &= \begin{bmatrix} \mathbf{I} & \mathbf{0} \\ \mathbf{0} & \mathbf{X}_i \end{bmatrix} \begin{bmatrix} \mathbf{A}_{i2} & \mathbf{B}_{i2} \\ \mathbf{B}_{i2} & \mathbf{A}_{i2} \end{bmatrix} \begin{bmatrix} \mathbf{c}_2^{++} \\ \mathbf{c}_2^{--} \end{bmatrix} \\
\begin{bmatrix} \mathbf{X}_i \mathbf{A}_{i1} + \mathbf{0B}_{i1} & \mathbf{X}_i \mathbf{B}_{i1} + \mathbf{0A}_{i1} \\ \mathbf{0A}_{i1} + \mathbf{IB}_{i1} & \mathbf{0B}_{i1} + \mathbf{IA}_{i1} \end{bmatrix} \begin{bmatrix} \mathbf{c}_1^{++} \\ \mathbf{c}_1^{--} \end{bmatrix} &= \begin{bmatrix} \mathbf{IA}_{i2} + \mathbf{0B}_{i2} & \mathbf{IB}_{i2} + \mathbf{0A}_{i2} \\ \mathbf{0A}_{i2} + \mathbf{X}_i \mathbf{B}_{i2} & \mathbf{0B}_{i2} + \mathbf{X}_i \mathbf{A}_{i2} \end{bmatrix} \begin{bmatrix} \mathbf{c}_2^{++} \\ \mathbf{c}_2^{--} \end{bmatrix} \\
\begin{bmatrix} \mathbf{X}_i \mathbf{A}_{i1} & \mathbf{X}_i \mathbf{B}_{i1} \\ \mathbf{B}_{i1} & \mathbf{A}_{i1} \end{bmatrix} \begin{bmatrix} \mathbf{c}_1^{++} \\ \mathbf{c}_1^{--} \end{bmatrix} &= \begin{bmatrix} \mathbf{A}_{i2} & \mathbf{B}_{i2} \\ \mathbf{X}_i \mathbf{B}_{i2} & \mathbf{X}_i \mathbf{A}_{i2} \end{bmatrix} \begin{bmatrix} \mathbf{c}_2^{++} \\ \mathbf{c}_2^{--} \end{bmatrix} \\
\begin{bmatrix} \mathbf{X}_i \mathbf{A}_{i1} \mathbf{c}_1^{++} + \mathbf{X}_i \mathbf{B}_{i1} \mathbf{c}_1^{--} \\ \mathbf{B}_{i1} \mathbf{c}_1^{++} + \mathbf{A}_{i1} \mathbf{c}_1^{--} \end{bmatrix} &= \begin{bmatrix} \mathbf{A}_{i2} \mathbf{c}_2^{++} + \mathbf{B}_{i2} \mathbf{c}_2^{--} \\ \mathbf{X}_i \mathbf{B}_{i2} \mathbf{c}_2^{++} + \mathbf{X}_i \mathbf{A}_{i2} \mathbf{c}_2^{--} \end{bmatrix}
\end{aligned}$$

Now the independent equations are extracted from the matrices.

$$\mathbf{X}_i \mathbf{A}_{i1} \mathbf{c}_1^{++} + \mathbf{X}_i \mathbf{B}_{i1} \mathbf{c}_1^{--} = \mathbf{A}_{i2} \mathbf{c}_2^{++} + \mathbf{B}_{i2} \mathbf{c}_2^{--}$$

$$\mathbf{B}_{i1} \mathbf{c}_1^{++} + \mathbf{A}_{i1} \mathbf{c}_1^{--} = \mathbf{X}_i \mathbf{B}_{i2} \mathbf{c}_2^{++} + \mathbf{X}_i \mathbf{A}_{i2} \mathbf{c}_2^{--}$$

The  $\mathbf{c}_2^{++}$  and  $\mathbf{c}_1^{--}$  are now solved for.

$$\begin{aligned}
\mathbf{X}_i \mathbf{A}_{i1} \mathbf{c}_1^{++} + \mathbf{X}_i \mathbf{B}_{i1} \mathbf{c}_1^{--} &= \mathbf{A}_{i2} \mathbf{c}_2^{++} + \mathbf{B}_{i2} \mathbf{c}_2^{--} \\
\mathbf{A}_{i2} \mathbf{c}_2^{++} + \mathbf{B}_{i2} \mathbf{c}_2^{--} &= \mathbf{X}_i \mathbf{A}_{i1} \mathbf{c}_1^{++} + \mathbf{X}_i \mathbf{B}_{i1} \mathbf{c}_1^{--} \\
\mathbf{A}_{i2} \mathbf{c}_2^{++} &= \mathbf{X}_i \mathbf{A}_{i1} \mathbf{c}_1^{++} + \mathbf{X}_i \mathbf{B}_{i1} \mathbf{c}_1^{--} - \mathbf{B}_{i2} \mathbf{c}_2^{--} \\
\boxed{\mathbf{c}_2^{++} = \mathbf{A}_{i2}^{-1} \mathbf{X}_i \mathbf{A}_{i1} \mathbf{c}_1^{++} + \mathbf{A}_{i2}^{-1} \mathbf{X}_i \mathbf{B}_{i1} \mathbf{c}_1^{--} - \mathbf{A}_{i2}^{-1} \mathbf{B}_{i2} \mathbf{c}_2^{--}}
\end{aligned}$$

$$\begin{aligned}
\mathbf{B}_{i1} \mathbf{c}_1^{++} + \mathbf{A}_{i1} \mathbf{c}_1^{--} &= \mathbf{X}_i \mathbf{B}_{i2} \mathbf{c}_2^{++} + \mathbf{X}_i \mathbf{A}_{i2} \mathbf{c}_2^{--} \\
\mathbf{A}_{i1} \mathbf{c}_1^{--} &= \mathbf{X}_i \mathbf{B}_{i2} \mathbf{c}_2^{++} + \mathbf{X}_i \mathbf{A}_{i2} \mathbf{c}_2^{--} - \mathbf{B}_{i1} \mathbf{c}_1^{++} \\
\boxed{\mathbf{c}_1^{--} = \mathbf{A}_{i1}^{-1} \mathbf{X}_i \mathbf{B}_{i2} \mathbf{c}_2^{++} + \mathbf{A}_{i1}^{-1} \mathbf{X}_i \mathbf{A}_{i2} \mathbf{c}_2^{--} - \mathbf{A}_{i1}^{-1} \mathbf{B}_{i1} \mathbf{c}_1^{++}}
\end{aligned}$$

These solved terms are now substituted back into their respected equations and solved.



$$\begin{aligned}
\mathbf{S}_{11}^i &= \left( \mathbf{A}_{i1} - \mathbf{X}_i \mathbf{B}_{i2} \mathbf{A}_{i2}^{-1} \mathbf{X}_i \mathbf{B}_{i1} \right)^{-1} \left( \mathbf{X}_i \mathbf{B}_{i2} \mathbf{A}_{i2}^{-1} \mathbf{X}_i \mathbf{A}_{i1} - \mathbf{B}_{i1} \right) \\
\mathbf{S}_{12}^i &= \left( \mathbf{A}_{i1} - \mathbf{X}_i \mathbf{B}_{i2} \mathbf{A}_{i2}^{-1} \mathbf{X}_i \mathbf{B}_{i1} \right)^{-1} \mathbf{X}_i \left( \mathbf{A}_{i2} - \mathbf{B}_{i2} \mathbf{A}_{i2}^{-1} \mathbf{B}_{i2} \right) \\
\mathbf{S}_{21}^i &= \left( \mathbf{A}_{i2} - \mathbf{X}_i \mathbf{B}_{i1} \mathbf{A}_{i1}^{-1} \mathbf{X}_i \mathbf{B}_{i2} \right)^{-1} \mathbf{X}_i \left( \mathbf{A}_{i1} - \mathbf{B}_{i1} \mathbf{A}_{i1}^{-1} \mathbf{B}_{i1} \right) \\
\mathbf{S}_{22}^i &= \left( \mathbf{A}_{i2} - \mathbf{X}_i \mathbf{B}_{i1} \mathbf{A}_{i1}^{-1} \mathbf{X}_i \mathbf{B}_{i2} \right)^{-1} \left( \mathbf{B}_{i2} + \mathbf{X}_i \mathbf{B}_{i1} \mathbf{A}_{i1}^{-1} \mathbf{X}_i \mathbf{A}_{i2} \right)
\end{aligned}$$

## A6: Derivation of Redheffer's star product

This derivation begins with two scattering matrices that need to be combined.

$$\begin{bmatrix} \mathbf{c}_1^- \\ \mathbf{c}_2^+ \end{bmatrix} = \begin{bmatrix} \mathbf{a}_{11} & \mathbf{a}_{12} \\ \mathbf{a}_{21} & \mathbf{a}_{22} \end{bmatrix} \begin{bmatrix} \mathbf{c}_1^+ \\ \mathbf{c}_2^- \end{bmatrix}$$

$$\begin{bmatrix} \mathbf{c}_2^- \\ \mathbf{c}_3^+ \end{bmatrix} = \begin{bmatrix} \mathbf{b}_{11} & \mathbf{b}_{12} \\ \mathbf{b}_{21} & \mathbf{b}_{22} \end{bmatrix} \begin{bmatrix} \mathbf{c}_2^+ \\ \mathbf{c}_3^- \end{bmatrix}$$

From here the matrix equations are expanded into their normal form.

$$\mathbf{c}_1^- = \mathbf{a}_{11}\mathbf{c}_1^+ + \mathbf{a}_{12}\mathbf{c}_2^-$$

$$\mathbf{c}_2^+ = \mathbf{a}_{21}\mathbf{c}_1^+ + \mathbf{a}_{22}\mathbf{c}_2^-$$

$$\mathbf{c}_2^- = \mathbf{b}_{11}\mathbf{c}_2^+ + \mathbf{b}_{12}\mathbf{c}_3^-$$

$$\mathbf{c}_3^+ = \mathbf{b}_{21}\mathbf{c}_2^+ + \mathbf{b}_{22}\mathbf{c}_3^-$$

Next the  $\mathbf{c}_2^-$  equation is substituted into the  $\mathbf{c}_2^+$  and solved for the  $\mathbf{c}_2^-$  term.

$$\mathbf{c}_2^- = \mathbf{b}_{11}(\mathbf{a}_{21}\mathbf{c}_1^+ + \mathbf{a}_{22}\mathbf{c}_2^-) + \mathbf{b}_{12}\mathbf{c}_3^-$$

$$\mathbf{c}_2^- = \mathbf{b}_{11}\mathbf{a}_{21}\mathbf{c}_1^+ + \mathbf{b}_{11}\mathbf{a}_{22}\mathbf{c}_2^- + \mathbf{b}_{12}\mathbf{c}_3^-$$

$$\mathbf{c}_2^- - \mathbf{b}_{11}\mathbf{a}_{22}\mathbf{c}_2^- = \mathbf{b}_{11}\mathbf{a}_{21}\mathbf{c}_1^+ + \mathbf{b}_{12}\mathbf{c}_3^-$$

$$(\mathbf{I} - \mathbf{b}_{11}\mathbf{a}_{22})\mathbf{c}_2^- = \mathbf{b}_{11}\mathbf{a}_{21}\mathbf{c}_1^+ + \mathbf{b}_{12}\mathbf{c}_3^-$$

$$\boxed{\mathbf{c}_2^- = (\mathbf{I} - \mathbf{b}_{11}\mathbf{a}_{22})^{-1} \mathbf{b}_{11}\mathbf{a}_{21}\mathbf{c}_1^+ + (\mathbf{I} - \mathbf{b}_{11}\mathbf{a}_{22})^{-1} \mathbf{b}_{12}\mathbf{c}_3^-}$$

This is repeated with the  $\mathbf{c}_2^+$  term.

$$\mathbf{c}_2^+ = \mathbf{a}_{21}\mathbf{c}_1^+ + \mathbf{a}_{22}(\mathbf{b}_{11}\mathbf{c}_2^+ + \mathbf{b}_{12}\mathbf{c}_3^-)$$

$$\mathbf{c}_2^+ = \mathbf{a}_{21}\mathbf{c}_1^+ + \mathbf{a}_{22}\mathbf{b}_{11}\mathbf{c}_2^+ + \mathbf{a}_{22}\mathbf{b}_{12}\mathbf{c}_3^-$$

$$\mathbf{c}_2^+ - \mathbf{a}_{22}\mathbf{b}_{11}\mathbf{c}_2^+ = \mathbf{a}_{21}\mathbf{c}_1^+ + \mathbf{a}_{22}\mathbf{b}_{12}\mathbf{c}_3^-$$

$$(\mathbf{I} - \mathbf{a}_{22}\mathbf{b}_{11})\mathbf{c}_2^+ = \mathbf{a}_{21}\mathbf{c}_1^+ + \mathbf{a}_{22}\mathbf{b}_{12}\mathbf{c}_3^-$$

$$\boxed{\mathbf{c}_2^+ = (\mathbf{I} - \mathbf{a}_{22}\mathbf{b}_{11})^{-1} \mathbf{a}_{21}\mathbf{c}_1^+ + (\mathbf{I} - \mathbf{a}_{22}\mathbf{b}_{11})^{-1} \mathbf{a}_{22}\mathbf{b}_{12}\mathbf{c}_3^-}$$

At this point the  $\mathbf{c}_2'^{-}$  can be eliminated by substituting the  $\mathbf{c}_2'^{-}$  equation into the  $\mathbf{c}_2'^{+}$  equation.

$$\begin{aligned}\mathbf{c}_1'^{-} &= \mathbf{a}_{11}\mathbf{c}_1'^{+} + \mathbf{a}_{12}\left((\mathbf{I} - \mathbf{b}_{11}\mathbf{a}_{22})^{-1}\mathbf{b}_{11}\mathbf{a}_{21}\mathbf{c}_1'^{+} + (\mathbf{I} - \mathbf{b}_{11}\mathbf{a}_{22})^{-1}\mathbf{b}_{12}\mathbf{c}_3'^{-}\right) \\ \mathbf{c}_1'^{-} &= \mathbf{a}_{11}\mathbf{c}_1'^{+} + \mathbf{a}_{12}(\mathbf{I} - \mathbf{b}_{11}\mathbf{a}_{22})^{-1}\mathbf{b}_{11}\mathbf{a}_{21}\mathbf{c}_1'^{+} + \mathbf{a}_{12}(\mathbf{I} - \mathbf{b}_{11}\mathbf{a}_{22})^{-1}\mathbf{b}_{12}\mathbf{c}_3'^{-} \\ \boxed{\mathbf{c}_1'^{-} &= (\mathbf{a}_{11} + \mathbf{a}_{12}(\mathbf{I} - \mathbf{b}_{11}\mathbf{a}_{22})^{-1}\mathbf{b}_{11}\mathbf{a}_{21})\mathbf{c}_1'^{+} + \mathbf{a}_{12}(\mathbf{I} - \mathbf{b}_{11}\mathbf{a}_{22})^{-1}\mathbf{b}_{12}\mathbf{c}_3'^{-}}\end{aligned}$$

This step is repeated with the  $\mathbf{c}_2'^{+}$  term solving for the  $\mathbf{c}_3'^{+}$  term.

$$\begin{aligned}\mathbf{c}_3'^{+} &= \mathbf{b}_{21}\left((\mathbf{I} - \mathbf{a}_{22}\mathbf{b}_{11})^{-1}\mathbf{a}_{21}\mathbf{c}_1'^{+} + (\mathbf{I} - \mathbf{a}_{22}\mathbf{b}_{11})^{-1}\mathbf{a}_{22}\mathbf{b}_{12}\mathbf{c}_3'^{-}\right) + \mathbf{b}_{22}\mathbf{c}_3'^{-} \\ \mathbf{c}_3'^{+} &= \mathbf{b}_{21}(\mathbf{I} - \mathbf{a}_{22}\mathbf{b}_{11})^{-1}\mathbf{a}_{21}\mathbf{c}_1'^{+} + \mathbf{b}_{21}(\mathbf{I} - \mathbf{a}_{22}\mathbf{b}_{11})^{-1}\mathbf{a}_{22}\mathbf{b}_{12}\mathbf{c}_3'^{-} + \mathbf{b}_{22}\mathbf{c}_3'^{-} \\ \boxed{\mathbf{c}_3'^{+} &= \mathbf{b}_{21}(\mathbf{I} - \mathbf{a}_{22}\mathbf{b}_{11})^{-1}\mathbf{a}_{21}\mathbf{c}_1'^{+} + (\mathbf{b}_{21}(\mathbf{I} - \mathbf{a}_{22}\mathbf{b}_{11})^{-1}\mathbf{a}_{22}\mathbf{b}_{12} + \mathbf{b}_{22})\mathbf{c}_3'^{-}}\end{aligned}$$

These equations are now combined into block matrix form.

$$\begin{aligned}\mathbf{c}_1'^{-} &= (\mathbf{a}_{11} + \mathbf{a}_{12}(\mathbf{I} - \mathbf{b}_{11}\mathbf{a}_{22})^{-1}\mathbf{b}_{11}\mathbf{a}_{21})\mathbf{c}_1'^{+} + \mathbf{a}_{12}(\mathbf{I} - \mathbf{b}_{11}\mathbf{a}_{22})^{-1}\mathbf{b}_{12}\mathbf{c}_3'^{-} \\ \mathbf{c}_3'^{+} &= \mathbf{b}_{21}(\mathbf{I} - \mathbf{a}_{22}\mathbf{b}_{11})^{-1}\mathbf{a}_{21}\mathbf{c}_1'^{+} + (\mathbf{b}_{21}(\mathbf{I} - \mathbf{a}_{22}\mathbf{b}_{11})^{-1}\mathbf{a}_{22}\mathbf{b}_{12} + \mathbf{b}_{22})\mathbf{c}_3'^{-}\end{aligned}$$

$$\begin{bmatrix} \mathbf{c}_1'^{-} \\ \mathbf{c}_3'^{+} \end{bmatrix} = \begin{bmatrix} \mathbf{a}_{11} + \mathbf{a}_{12}(\mathbf{I} - \mathbf{b}_{11}\mathbf{a}_{22})^{-1}\mathbf{b}_{11}\mathbf{a}_{21} & \mathbf{a}_{12}(\mathbf{I} - \mathbf{b}_{11}\mathbf{a}_{22})^{-1}\mathbf{b}_{12} \\ \mathbf{b}_{21}(\mathbf{I} - \mathbf{a}_{22}\mathbf{b}_{11})^{-1}\mathbf{a}_{21} & \mathbf{b}_{22} + \mathbf{b}_{21}(\mathbf{I} - \mathbf{a}_{22}\mathbf{b}_{11})^{-1}\mathbf{a}_{22}\mathbf{b}_{12} \end{bmatrix} \begin{bmatrix} \mathbf{c}_1'^{+} \\ \mathbf{c}_3'^{-} \end{bmatrix}$$

From here the final form of Redheffer's star product is shown.

$$\mathbf{S} = \mathbf{S}_a \otimes \mathbf{S}_b \qquad \mathbf{S}_a = \begin{bmatrix} \mathbf{a}_{11} & \mathbf{a}_{12} \\ \mathbf{a}_{21} & \mathbf{a}_{22} \end{bmatrix} \qquad \mathbf{S}_b = \begin{bmatrix} \mathbf{b}_{11} & \mathbf{b}_{12} \\ \mathbf{b}_{21} & \mathbf{b}_{22} \end{bmatrix}$$

$$\mathbf{S} = \begin{bmatrix} \mathbf{S}_{11} & \mathbf{S}_{12} \\ \mathbf{S}_{21} & \mathbf{S}_{22} \end{bmatrix}$$

$$\mathbf{S}_{11} = \mathbf{a}_{11} + \mathbf{a}_{12} \left( \mathbf{I} - \mathbf{b}_{11} \mathbf{a}_{22} \right)^{-1} \mathbf{b}_{11} \mathbf{a}_{21}$$

$$\mathbf{S}_{12} = \mathbf{a}_{12} \left( \mathbf{I} - \mathbf{b}_{11} \mathbf{a}_{22} \right)^{-1} \mathbf{b}_{12}$$

$$\mathbf{S}_{21} = \mathbf{b}_{21} \left( \mathbf{I} - \mathbf{a}_{22} \mathbf{b}_{11} \right)^{-1} \mathbf{a}_{21}$$

$$\mathbf{S}_{22} = \mathbf{b}_{22} + \mathbf{b}_{21} \left( \mathbf{I} - \mathbf{a}_{22} \mathbf{b}_{11} \right)^{-1} \mathbf{a}_{22} \mathbf{b}_{12}$$

### A7: Derivation of the longitudinal field component from the divergence equation.

This derivation starts with the electric field divergence equation from Maxwell's equations.

$$\nabla \cdot \vec{E} = 0$$

This equation is expanded into Cartesian coordinates.

$$\frac{\partial}{\partial x} \left( E_x e^{-j\vec{k} \cdot \vec{r}} \right) + \frac{\partial}{\partial y} \left( E_y e^{-j\vec{k} \cdot \vec{r}} \right) + \frac{\partial}{\partial z} \left( E_z e^{-j\vec{k} \cdot \vec{r}} \right) = 0$$

Now the partial derivatives are solved analytically.

$$-jk_x E_x e^{-j\vec{k} \cdot \vec{r}} - jk_y E_y e^{-j\vec{k} \cdot \vec{r}} - jk_z E_z e^{-j\vec{k} \cdot \vec{r}} = 0$$

From here the  $E_z$  term is solved for.

$$\begin{aligned} & -jk_x E_x e^{-j\vec{k} \cdot \vec{r}} - jk_y E_y e^{-j\vec{k} \cdot \vec{r}} - jk_z E_z e^{-j\vec{k} \cdot \vec{r}} = 0 \\ & \frac{1}{-je^{-j\vec{k} \cdot \vec{r}}} \left( -jk_x E_x e^{-j\vec{k} \cdot \vec{r}} - jk_y E_y e^{-j\vec{k} \cdot \vec{r}} - jk_z E_z e^{-j\vec{k} \cdot \vec{r}} \right) = \frac{1}{-je^{-j\vec{k} \cdot \vec{r}}} 0 \end{aligned}$$

$$k_x E_x + k_y E_y + k_z E_z = 0$$

$$k_z E_z = -k_x E_x - k_y E_y$$

$$E_z = \frac{-k_x E_x - k_y E_y}{k_z}$$

## **Vita**

Jay Houston Barton is a U.S. Army veteran that spent two years overseas serving his country. After being honorable discharged from the Army in 2006, he started college at El Paso Community College. From here he received his A.A. in Electrical/Electronic Engineering in 2008 and transferred the University of Texas at El Paso (UTEP). He finished his bachelors in 2010 and was awarded a degree in Electrical Engineering.

In 2011 he started his graduate studies at UTEP entering the accelerated Ph.D. program. His main research focus was frequency selective surfaces for high-power microwaves and electromagnetic metamaterials with Professor Raymond Rumpf. During this time he was awarded two prestigious summer fellowships with military laboratories. The first was with the Directed Energy Directorate at the Air Force Research Laboratory, and the second was at the Survivability, Vulnerability and Assessment Directorate, at White Sands Missile Range. In May 2014 he received his doctorate in Electrical and Computer Engineering.

He is the first author of 3 peer-reviewed articles, two published and one submitted for publication and is also co-author on 3 other peer-reviewed articles. He has presented at two conferences on technologies for high-power microwaves.

Jay Barton is an avid outdoorsman, who likes to spend his free time hunting, fishing and camping in the wilds of New Mexico with family and friends.

Permanent address: 5 Our Way

Anthony, New Mexico, 88012

This dissertation was typed by Jay Houston Barton.